Hillslope erosion and weathering rates in Earth's most rapidly uplifting mountains

Isaac James Larsen

A dissertation
submitted in partial fulfillment of the
requirements for the degree of

Doctor of Philosophy

University of Washington
2013

Reading Committee:
David R. Montgomery, Chair
John O. Stone
Alan R. Gillespie

Program authorized to offer degree:
Department of Earth and Space Sciences

University of Washington

Abstract

Hillslope erosion and weathering rates in Earth's most rapidly uplifting mountains

Isaac James Larsen

Chair of the Supervisory Committee:
Professor David R. Montgomery
Department of Earth and Space Sciences

Knowledge of hillslope erosion rates and processes is necessary for understanding landscape response to tectonic and climatic forcing and for determining the degree to which mountains regulate biogeochemical cycles and global climate. Landslide erosion and soil production are the principle denudation processes in high-relief terrain, but quantitative estimates of landslide erosion on spatial and temporal scales relevant to landscape evolution are lacking, and there have been no prior measurements of soil production and weathering rates in Earth's most tectonically-active landscapes. Here, I address both of these problems, first by attempting to overcome the inherent difficulty in quantifying landslide erosion rates using a compilation of geometry measurements from 4,231 landslides. I use the geometry to develop scaling relationships that can be used to predict landslide volume from more readily available landslide area information. A key finding is that landslide scaling is controlled by hillslope material; soil landslides have lower depths and hence lower power-law volume-area scaling exponents than bedrock landslides, which has significant implications for accurately quantifying landslide erosion rates. By applying the landslide volume-area scaling relationship to over 15,000 landslides in the Tsangpo Gorge region of the eastern Himalaya, I demonstrate that landslide erosion rates are spatially coupled with stream power and long-term exhumation rates, but become decoupled from hillslope gradients when hillslope angles exceed 30°. These results indicate landslide erosion is coupled with bedrock river incision and rock uplift, but not topography, hence providing the first direct confirmation of a 'threshold hillslope' model of landscape evolution that has emerged over the last two decades. I address the role soils play in the denudation of rapidly uplifting mountains by developing soil production rate and catchment scale denudation data for the western Southern Alps of New Zealand. Soil production rates in the western Southern Alps can exceed those measured elsewhere by more than an order of magnitude and soil physical erosion rates are linearly coupled with chemical weathering rates. Using the relationship between physical and chemical denudation rates to model global weathering fluxes as a function of mean local slope, I demonstrate that the small, mountainous fraction of Earth's surface dominates the global chemical weathering flux. The weathering measurements and model results hence overturn the view that there are 'speed-limits' to soil production and that erosion and weathering are decoupled in mountains, and instead strongly support the hypothesis that mountain uplift influences global climate over geological timescales via links among topography, erosion, weathering, and CO_2 cycling.

To my family

ACKNOWLEDGEMENTS

Thank you Krista and Carl for your unwavering love and support over the past many years as I have completed this dissertation; I couldn't have done it without you. My parents and grandparents have provided encouragement and support as I've traveled a long path through many institutions of higher learning—thank you so much, especially to my parents, who always put their children's education first. Dave, I couldn't have asked for a better advisor; thank you for both giving me the freedom to venture out on my own path and for the very good advice you gave me along the way. Thank you John for welcoming me into your lab, helping push batches though in front of accelerator runs, and for teaching me everything I know about cosmogenic isotopes. Thanks also to Alan and Jeff Richie for thoughtful questions and comments that helped shape this work. Harvey, thank you so much for all of your GIS wisdom, which made much of this work possible. I have benefitted from interactions from a number of faculty at the University of Washington, particularly Bernard Hallet, Kate Huntington, Gerard Roe, Ron Sletten, and Brian Atwater. I especially thank Bernard for inspiring so much interest in the Tsangpo Gorge and Kate for continued discussions about the eastern Himalaya. It has been a privilege to work alongside so many great graduate students during my time at the University of Washington; thank you for your friendship.

I also thank Oliver Korup, not only for being a great colleague, but also for suggesting I take on the tedious task of determining the material of each landslide in the database—it certainly paid off. I had great fortune to have Peter Almond as a host during my two-month stay at Lincoln University in New Zealand. Without Peter's knowledge of the Southern Alps, we could never have pulled off the winter fieldwork; hopefully we'll have a chance to do it again.

Andre, you can’t thank someone enough who spent three weeks carrying ten kilogram bags of soil uphill through the Westland bush, but I’ll do it again anyway—thank you. Thanks very much to Brendon and Francis Malcolm for opening your home to me; my experience in New Zealand was all the better for it, including Francis’ hospitality and Brendon’s help in the field.

Thank you to Marganne Allen, Phil Flentje, Jim Griffiths, Richard Guthrie, Fumitoshi Imaizumi, Junko Iwahashi, Harvey Kelsey, Anke Knapen, Mary Ann Madej, Yvonne Martin, Christine May, Lewis Owen, Colin Pain, Leslie Reid, Alexander Strom, Jean Poesen, Roy Sidle, Miet Van Den Eeckhaut, and Hiro Yamagishi for generously sharing the landslide data presented in Chapter 2. The study simply would not have been possible without it.

The research presented in this dissertation was funded by a NASA Earth and Space Science Fellowship (award NNX09AN90H), the NSF East Asia and Pacific Summer Institutes program (award OISE-1015454), the Washington NASA Space Grant Consortium, Sigma Xi, the John Montagne Fund Award from the Geological Society of America, the J. Hoover Mackin Award from the Quaternary Geology and Geomorphology Division of the Geological Society of America, and the Quaternary Research Center and Department of Earth and Space Sciences, both at the University of Washington.

TABLE OF CONTENTS

Page

LIST OF FIGURES

LIST OF TABLES

CHAPTER 1

Introduction

Understanding the factors that govern landscape evolution and the interaction of surface processes with the larger Earth System are longstanding geological problems[1–3]. This dissertation focuses on quantifying erosion and weathering rates in some of the most tectonically-active landscapes on Earth, the Tsangpo Gorge region of the eastern Himalaya and the western Southern Alps on the South Island of New Zealand. The extreme rates of geomorphic activity in these landscapes certainly call loudly to a student of Earth surface dynamics, but still more appealing is the ability to use these landscapes as natural experiments that can be used to address fundamental questions regarding interactions among tectonics, topography, surface processes, and climate.

One such question involves determining the topographic and erosional response to tectonic forcing. In the case where landscapes maintain topographic equilibrium by balancing rates of rock uplift and erosion, hillslope angles should steepen as rock uplift rates increase so that progressively higher driving stresses engage increasingly rapid erosion processes[4]. However, hillslope steepness is limited by rock strength, hence hillslopes cannot steepen indefinitely as they are subjected to increasing uplift rates[5]. At high rock uplift rates, hillslopes are thought to steepen to a strength-limited, or threshold angle, where further increases in the uplift rate are accommodated only via increases in erosion rates, rather than landscape steepening[6–8]. Landsliding is conventionally thought to be the only hillslope processes capable of eroding at rates commensurate with rapid rock uplift[9]—but see below. Hence spatial patterns of landslide erosion, rather than hillslope angles should track rock uplift rates in tectonically-active mountains. This 'threshold hillslope' model of landscape evolution has garnered considerable indirect support in the nearly two decades since it was proposed[6,8,10,11]; yet the model has never been directly tested with landslide erosion data.

Landslide erosion rates are inherently difficult to quantify, which, in part, explains why no prior studies have developed landslide erosion data of sufficient spatial and temporal resolution for testing the threshold hillslope model. Because it is unfeasible to measure the volume of individual landslides in the field within even modestly-sized study areas, scaling relationships are generally used to predict landslide volumes from landslide area data[12], which are more readily obtained via mapping on remotely sensed images. The problem with this approach is that volume-area scaling relationships derived in one landscape are often applied to different landscapes with little regard to potential errors due to inherent differences in landslide geometry scaling; this represents a major limitation to accurate estimation of landslide erosion rates. In Chapter 2, I report efforts to overcome this limitation, using a compilation of 4,231 field measurements of landslide area, depth, and volume that is an order of magnitude larger than any other dataset of its kind. The compilation reveals that the power-law volume-area scaling exponent varies primarily as a function of whether landslide failures involve unconsolidated soil and regolith or bedrock. Hence, hillslope material is a primary control on landslide volumes and erosion rates. There is also considerable regional variability in scaling exponents, which can lead to order-of-magnitude errors in landslide erosion estimates if scaling relationships are improperly extrapolated. Additionally, the correspondence of soil and landslide depths in landscapes with both sets of measurements suggests that the rate of soil production may ultimately limit shallow landslide erosion rates, and rapid soil formation on landslides scars leads to the intriguing hypothesis that soil production rates may be much higher than previously thought, which is explored more fully in Chapter 4.

Equipped with the ability to more accurately estimate landslide volumes, I directly tested the threshold hillslope model with landslide erosion data from the eastern Himalayan syntaxis—a rapidly eroding landscape that dominates the erosional flux of the Tsangpo-Brahmaputra River system[13,14]. The area surrounding the Tsangpo Gorge is ideal for testing the threshold hillslope model because previous work has documented exhumation rates that vary spatially by more than two orders of magnitude[13,15-17] and stream power that varies spatially by more than three orders of magnitude[15]. These data indicate rock uplift and bedrock river incision are spatially-variable, yet hillslope angles are remarkably uniform. In Chapter 3, I report landslide erosion data based on 15,257 landslides I mapped in and around the Tsangpo Gorge. Landslide erosion rates are spatially coupled with both stream power and exhumation rates, but increase non-linearly once hillslope angles reach 30°. Given that exhumation and rock uplift must be roughly in balance within the eastern Himalaya, the results indicate that tectonically driven rock uplift drives landslide erosion on hillslopes steepened to their strength-limiting angle, as 30° is similar to the friction angle of fractured bedrock. These data provide the first direct support for the threshold hillslope model, a now dominant paradigm guiding the study of tectonic geomorphology and landscape evolution.

Over a century ago, T.C. Chamberlin hypothesized that mountain uplift was responsible for ice ages[1]. Revival of that hypothesis two decades ago[18,19] led to a large, multi-disciplinary effort to understand links among tectonically-driven rock uplift, topographic relief, atmospheric circulation, erosion rates, silicate weathering rates, organic carbon cycling, sequestration of CO_2, and global cooling[20]. These efforts continue, though recent studies have suggested that uplift and climate may not be linked because: mountain uplift does not increase erosion and weathering rates[21]; erosion and weathering rates are decoupled in rapidly eroding mountains due to soil production rate and chemical weathering speed-limits[22]; and the fraction of Earth's surface covered by mountains is too small for mountains to contribute significantly to global sediment and weathering fluxes[23]. The evidence used to advocate for decoupling of erosion and weathering, and hence a broken link between uplift and climate, are model results that predict that soil weathering rates become decoupled from erosion rates, based on the assumption that soil thickness, and hence mineral residence times in the weathering zone, approach zero as erosion rates increase[24–26], and a compilation of global soil production and weathering rate data[22]. The problem is that there are no soil production and weathering rate data from rapidly uplifting and eroding mountains, so the models that predict decoupling of weathering and erosion cannot be evaluated, and the setting of 'speed limits' to soil production and weathering is based on limited data that clearly do not extend to landscapes germane to the uplift-climate hypothesis.

Using *in-situ* produced ^{10}Be and zirconium mass balance data, I generated the first dataset of soil production and weathering rates in a rapidly eroding landscape; the western Southern Alps of New Zealand. The results, which are presented in Chapter 4, show that soil production and chemical weathering rates are extremely rapid, and that chemical and physical denudation rates are tightly coupled. Modeling global-scale denudation as a function of mean local slope, and chemical weathering rates as a function of denudation rate demonstrates that mountains, though small in terms of land area, dominate erosional and chemical weathering inputs to Earth's oceans. The measurements from the western Southern Alps break the proposed soil production and weathering rate speed limits and overturn the model-based view of decoupled erosion and weathering. Hence the results demonstrate that the link between erosion and weathering is intact and provide strong support for a tectonic influence on global climate.

The final chapter of this dissertation (Chapter 5) provides a brief summary of the key findings of this work, as well as some concluding remarks on the study of tectonics, topography, climate, and erosion. In Chapters 2-4, the key findings of each study and their implications are presented first, followed by a description of methods. More detailed methods, figures, and additional data that support each chapter are presented in the appendices. Chapter 2 has been published in *Nature Geoscience*[27] with co-authors David R. Montgomery and Oliver Korup. A manuscript based on Chapter 3, co-written with David R. Montgomery has also been published in *Nature Geoscience*[28]. Chapter 4 will be submitted as two manuscripts, one on soil production and weathering rates with co-authors Peter C. Almond, Andre Eger, John O. Stone, David R. Montgomery and Brendon Malcolm, and a second on global denudation modeling with co-authors David R. Montgomery and Harvey M. Greenberg.

References

1. Chamberlin, T. C. An attempt to frame a working hypothesis of the cause of glacial periods on an atmospheric basis. *Journal of Geology* **7**, 545-584 (1899).
2. Davis, W. M. The geographical cycle. *The Geographical Journal* **14**, 481-504 (1899).
3. Gilbert, G. Report on the Geology of the Henry Mountains: Geographical and Geological Survey of the Rocky Mountain Region, 160 p. *US Gov. Print. Off., Washington, DC* (1877).
4. Hack, J. Interpretation of erosional topography in humid temperate climates. *American Journal of Science* **258**, 80–97 (1960).
5. Schmidt, K. & Montgomery, D. Limits to relief. *Science* **270**, 617-620 (1995).
6. Burbank, D. *et al.* Bedrock incision, rock uplift and threshold hillslopes in the northwestern Himalayas. *Nature* **379**, 505-510 (1996).
7. Montgomery, D. Slope distributions, threshold hillslopes, and steady-state topography. *American Journal of Science* **301**, 432 (2001).
8. Montgomery, D. & Brandon, M. Topographic controls on erosion rates in tectonically active mountain ranges. *Earth. Planet. Sci. Lett.* **201**, 481-489 (2002).

9. Burbank, D. Rates of erosion and their implications for exhumation. *Mineralogical Magazine* **66**, 25-52 (2002).
10. Korup, O. Rock type leaves topographic signature in landslide-dominated mountain ranges. *Geophysical Research Letters* **35**, L11402 (2008).
11. Binnie, S., Phillips, W., Summerfield, M. & Fifield, L. Tectonic uplift, threshold hillslopes, and denudation rates in a developing mountain range. *Geology* **35**, 743-746 (2007).
12. Hovius, N., Stark, C. & Allen, P. Sediment flux from a mountain belt derived by landslide mapping. *Geology* **25**, 231-234 (1997).
13. Stewart, R. *et al.* Brahmaputra sediment flux dominated by highly localized rapid erosion from the easternmost Himalaya. *Geology* **36**, 711-714 (2008).
14. Zeitler, P. *et al.* Erosion, Himalayan geodynamics, and the geomorphology of metamorphism. *GSA Today* **11**, 4-9 (2001).
15. Finnegan, N. *et al.* Coupling of rock uplift and river incision in the Namche Barwa-Gyala Peri massif, Tibet. *Geological Society of America Bulletin* **120**, 142-155 (2008).
16. Burg, J. *et al.* Exhumation during crustal folding in the Namche-Barwa syntaxis. *Terra Nova* **9**, 53-56 (1997).
17. Seward, D. & Burg, J. Growth of the Namche Barwa Syntaxis and associated evolution of the Tsangpo Gorge: Constraints from structural and thermochronological data. *Tectonophysics* **451**, 282-289 (2008).
18. Raymo, M. & Ruddiman, W. Tectonic forcing of late Cenozoic climate. *Nature* **359**, 117-122 (1992).
19. Raymo, M., Ruddiman, W. & Froelich, P. Influence of late Cenozoic mountain building on ocean geochemical cycles. *Geology* **16**, 649-653 (1988).
20. Ruddiman, W. F. (ed.) Tectonic Uplift and Climate Change. Plenum Press, New York, 535 p. (1997).
21. Willenbring, J. & von Blanckenburg, F. Long-term stability of global erosion rates and weathering during late-Cenozoic cooling. *Nature* **465**, 211-214 (2010).
22. Dixon, J. & von Blanckenburg, F. Soils as pacemakers and limiters of global silicate weathering. *Comptes Rendus Geoscience* **344**, 597-609 (2012).
23. Willenbring, J., Codilean, A. & McElroy, B. Earth is (mostly) flat: Apportionment of the flux of continental sediment over millennial time scales. *Geology* **41**, 343-346 (2013).
24. Gabet, E. & Mudd, S. A theoretical model coupling chemical weathering rates with denudation rates. *Geology* **37**, 151-154 (2009).
25. Ferrier, K. & Kirchner, J. Effects of physical erosion on chemical denudation rates: A numerical modeling study of soil-mantled hillslopes. *Earth. Planet. Sci. Lett.* **272**, 591-599 (2008).
26. Hilley, G., Chamberlain, C., Moon, S., Porder, S. & Willett, S. Competition between erosion and reaction kinetics in controlling silicate-weathering rates. *Earth. Planet. Sci. Lett.* **293**, 191-199 (2010).
27. Larsen, I., Montgomery, D. & Korup, O. Landslide erosion controlled by hillslope material. *Nature Geoscience* **3**, 247-251 (2010).
28. Larsen, I. J. & Montgomery, D. R. Landslide erosion coupled to tectonics and river incision. *Nature Geoscience* **5**, 468-473 (2012).

CHAPTER 2

Landslide erosion controlled by hillslope material

Steep hillslopes in mountain belts are eroded by landslides, and landsliding is ultimately driven by the topographic relief produced by fluvial and glacial erosion[1–5]. Landslide erosion rates are derived from estimates of landslide volume and can help to appraise landscape responses to tectonic, climatic and anthropogenic forcing. However, the scaling relationships—power-law equations that are used to estimate the volume of the landslide from the area of the failure—are derived from a limited number of measurements, and do not discriminate between bedrock and soil landslides. Here we use a compilation of landslide geometry measurements from 4,231 individual landslides to assess the relative volume–area scaling of bedrock and soil landslides. We find that shallow, soil-based landslides can be approximated by an exponent of $\gamma = 1.1$–1.3. In contrast, landslides that involve the failure of bedrock have a deeper scar area, and hence larger volume, and are characterized by $\gamma = 1.3$–1.6. On the basis of observations that soil residence times in uplifting mountains can be as low as a few centuries[6], we suggest that both deep bedrock and frequent, shallow soil landslides can erode steep hillslopes at rates commensurate with even rapid tectonic uplift.

Quantifying rates of landslide erosion is essential for understanding links between physical erosion, chemical weathering and atmospheric CO_2 consumption[7,8], the transport of organic carbon from the terrestrial biosphere to ocean basin sinks[9,10], coupling among tectonic, atmospheric and surface processes[11], the productivity and sustainability of soil resources[12] and the forecasting of landslide hazards[13]. However, landslide erosion and the associated transport of soil, rock and biogeochemical constituents are difficult to quantify, in part because regional inventories contain hundreds to thousands of landslides, making it impractical to measure the depth of each landslide scar for determination of eroded volume. Hence, landslide volume and erosion estimates rely on scaling relationships based on relatively few field measurements[2,14–16], where the predicted volume V of a given landslide area A depends on a scaling exponent γ and intercept α such that $V = \alpha A^{\gamma}$. Such a model was first proposed over four decades ago[17]. Among the many subsequent studies of landslide scaling, limited data from New Zealand[2] were used to propose that landslide scar depth scales with landslide width. The resulting self-similar scaling with $\gamma = 1.5$ has been widely used outside New Zealand to estimate landslide volumes and erosion rates[7,13-15,18–21]. Recently, scaling with $\gamma = 1.45$ was proposed on the basis of 677 landslide measurements[22], leading to conclusions that V-A scaling is not significantly influenced by the geomorphic or mechanical properties of the failed soil or bedrock and that γ may vary with landslide size. Although these results draw on several landslide studies emphasizing V-A scaling, V is generally calculated as the product of A and mean landslide depth D, which introduces strong V-A covariance. Moreover, the tacit generality of these γ-values remains untested, or inferred from sample sizes constituting small fractions of published landslide inventories[22].

We assessed the degree to which variance in γ affects landslide erosion predictions with a sensitivity analysis that estimates the maximum degree of under- or over-prediction of total landslide volume (V_T), from a given inventory of landslide areas. The analysis shows that small differences in γ lead to substantial variance in V_T predictions. For example, using $\gamma = 1.5$ instead of $\gamma = 1.4$ overestimates V_T by at least a factor of two (Fig. 2.1). Prediction errors become larger with increasing difference in γ, decreasing area-frequency scaling exponents and increasing maximum landslide area, and can easily be one or more orders of magnitude. The degree of potential over- and under-estimation of landslide erosion is therefore large enough to warrant caution when applying any scaling relationship outside the region it was developed. Inappropriate use of self-similar scaling can lead to substantial errors in landslide volume predictions, and it follows that accurate estimation of γ may have a hitherto unrecognized role in quantifying landslide erosion and mass fluxes.

The lack of accurate constraints on γ for different hillslope materials is a key limitation for quantifying material transfer from uplands to lowlands, particularly as little is known about the relative contributions of soil (which we consider here as unconsolidated soil, regolith and colluvium) and bedrock landslides in denuding mountains. This is a major shortcoming, as on one hand it has been proposed that bedrock landsliding is the only hillslope process capable of keeping pace with the rapid, $1-10$ mm yr^{-1} long-term rates of river incision and exhumation of mid- to upper-crustal rocks inferred from studies of uplifting mountains[23]. This rate control may be manifest in adjusted frequencies or magnitudes of landslides on threshold hillslopes (those as steep as can be supported by their material strength). On the other hand, landslide erosion in soil-mantled landscapes may be limited by the rate at which bedrock weathers and is converted to soil[24]. Conceptual landscape evolution models hold that a transition from soil to bedrock landsliding in tectonically active mountains occurs where rock uplift rates greatly exceed soil formation rates[23]. If landslides dominate hillslope erosion through stripping of the soil mantle, soil depths should limit landslide scar depths. We tested the hypothesis that differing limits to

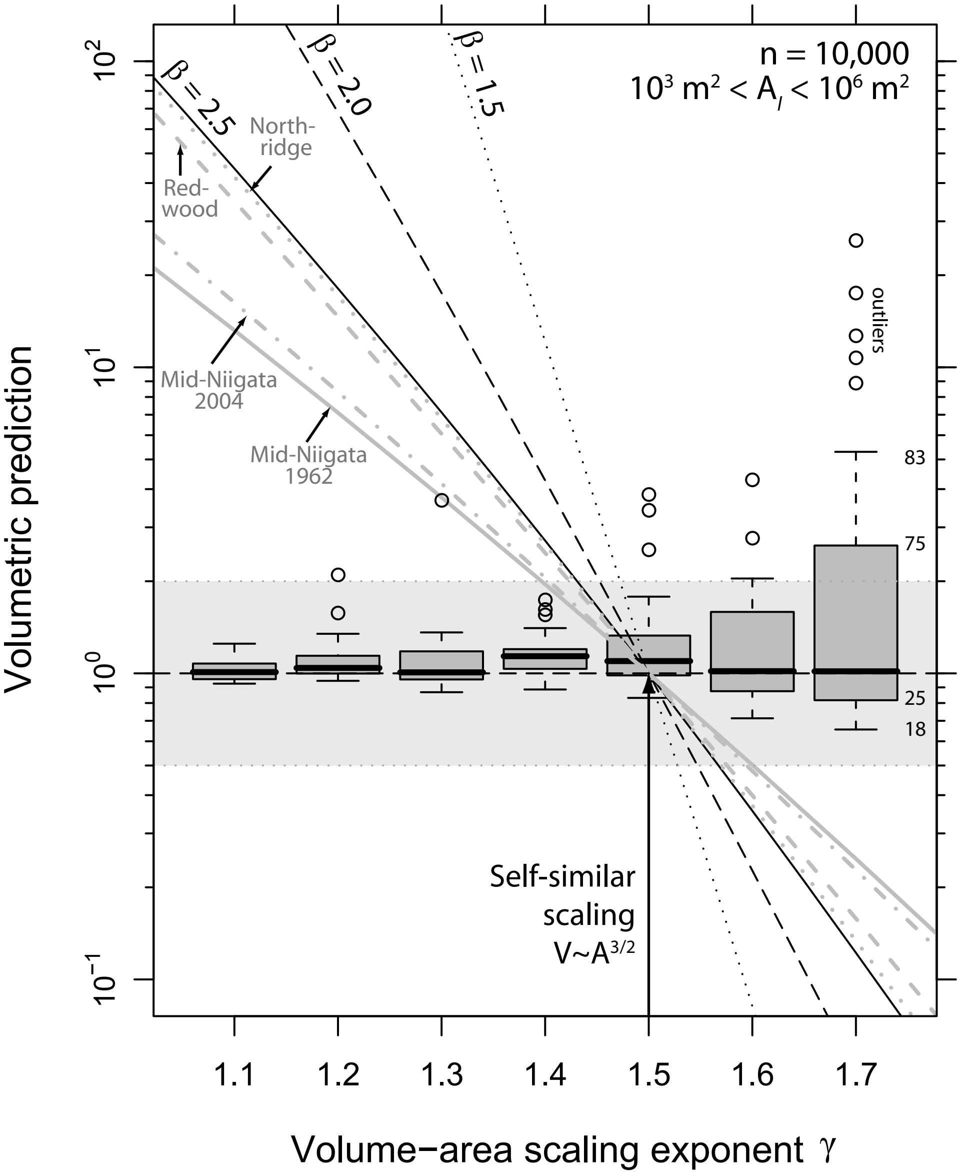

Figure 2.1. Effect of the volume–area scaling exponent γ on predicted total landslide volume (V_T). The total volumetric prediction is expressed as the ratio V_T (γ = 1.5)/V_T (γ) for three synthetic power-law distributed inventories (black lines) and four empirical landslide inventories (grey lines) of landslide area *A*. The grey shaded area encompasses factor of two under-/over-estimates. The boxes and whiskers show ranges of volumetric prediction for 30 randomly generated inventories of *A* for a fixed γ. Volumetric estimates from any two inventories with the same size range and scaling parameters generally vary by less than a factor of two, with the variance of the error increasing with γ, which is generally smaller than errors introduced by even small differences in γ. See Appendix 1 for data sources.

bedrock and soil landslide depths are mirrored in distinctly different *V-A* scaling parameters by compiling and analyzing 4,231 measurements of scar and deposit geometry for landslides from around the world, constituting to our best knowledge the largest database of this kind (Table A1.1). We demonstrate that scaling parameters vary significantly with material type, propose a physical basis for this variance and assess whether erosion by soil landslides is capable of keeping pace with bedrock uplift in tectonically active mountain ranges.

The documented landslides show power-law scaling over nine orders of magnitude in *A* and twelve orders of magnitude in *V*, with $\gamma = 1.332 \pm 0.005$ ($\pm 1\sigma$) (Fig. 2.2a). The high scatter in *D-A* data indicates considerable heterogeneity in measured landslide geometries (Fig. 2.2b). We examine the heterogeneity in landslide geometry by focusing on *V-A* scaling exponents because γ facilitates comparison with previous studies. Scaling exponents for bedrock and soil landslides differ significantly, with $\gamma_{\mathrm{rock}} = 1.35 \pm 0.01$ and $\gamma_{\mathrm{soil}} = 1.145 \pm 0.008$, which indicates *V-A* scaling varies with hillslope material. The combined data set consisting of all soil failures shows that scar depth or deposit thickness does not vary with landslide area, whereas the median depths of soil landslide scars increase by less than one order of magnitude with increasing landslide area (Fig. 2.3). In contrast, bedrock failures tend to become deeper and their deposits thicken by 2-3 orders of magnitude as landslide areas increase. This trend holds for the combined data set consisting of all bedrock failures, as well as data specifically from measurements of scars or deposits. The depths of small bedrock landslides ($<10^3$ m^2) are similar to soil landslides, probably because they occur in weathered or closely jointed bedrock mechanically similar to soil. Scaling exponents for global bedrock landslides derived from measurements of deposit ($\gamma = 1.40 \pm 0.02$) versus scar ($\gamma = 1.41 \pm 0.02$) geometry are indistinguishable (Table A1.1). Hence, the tendency for detached landslide masses to increase in volume because of dilation and

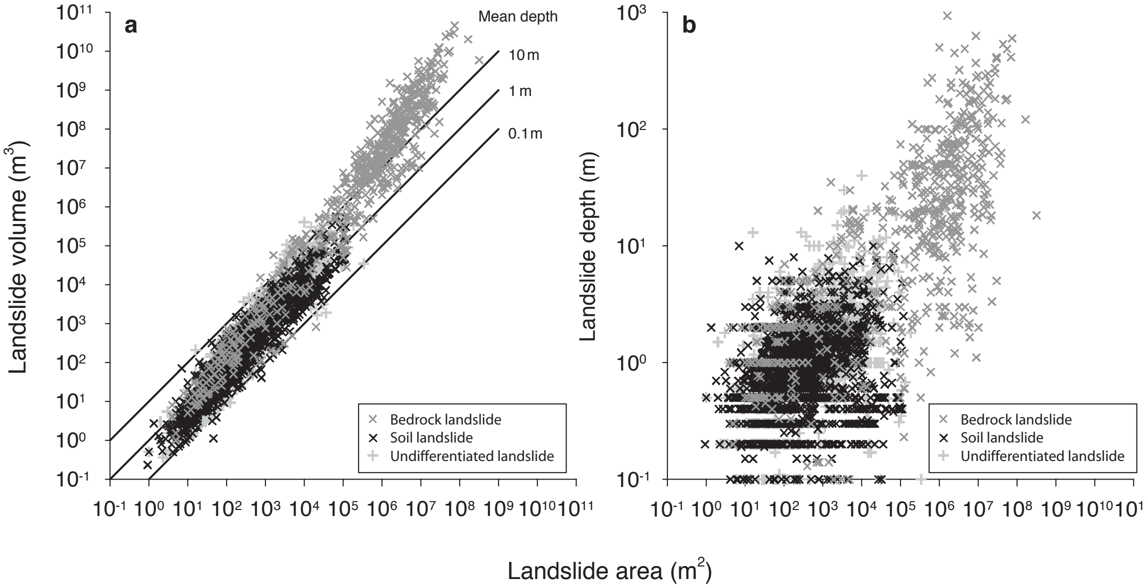

Figure 2.2. Landslide geometry scaling. Landslide volume versus area (a) and depth versus area (b). Data are for bedrock landslides (n = 604), soil landslides (n = 2,136) and undifferentiated landslides (n = 1,491). The landslide volume–area data may be described by power-law scaling with log $\alpha = -0.836\pm0.015$ with units $[L^{(3-2\gamma)}]$, $\gamma = 1.332\pm0.005$ and $R^2 = 0.95$. Depth-area data may be described by log $\alpha = -1.090\pm0.015$ with units $[L^{(1\text{-}2\gamma)}]$, $\gamma = 0.420\pm0.005$ and $R^2 = 0.50$. The soil landslide data include 1,617 and 124 measurements of scar and deposit geometry, respectively. The bedrock landslide data include 168 and 344 measurements of scar and deposit geometry, respectively.

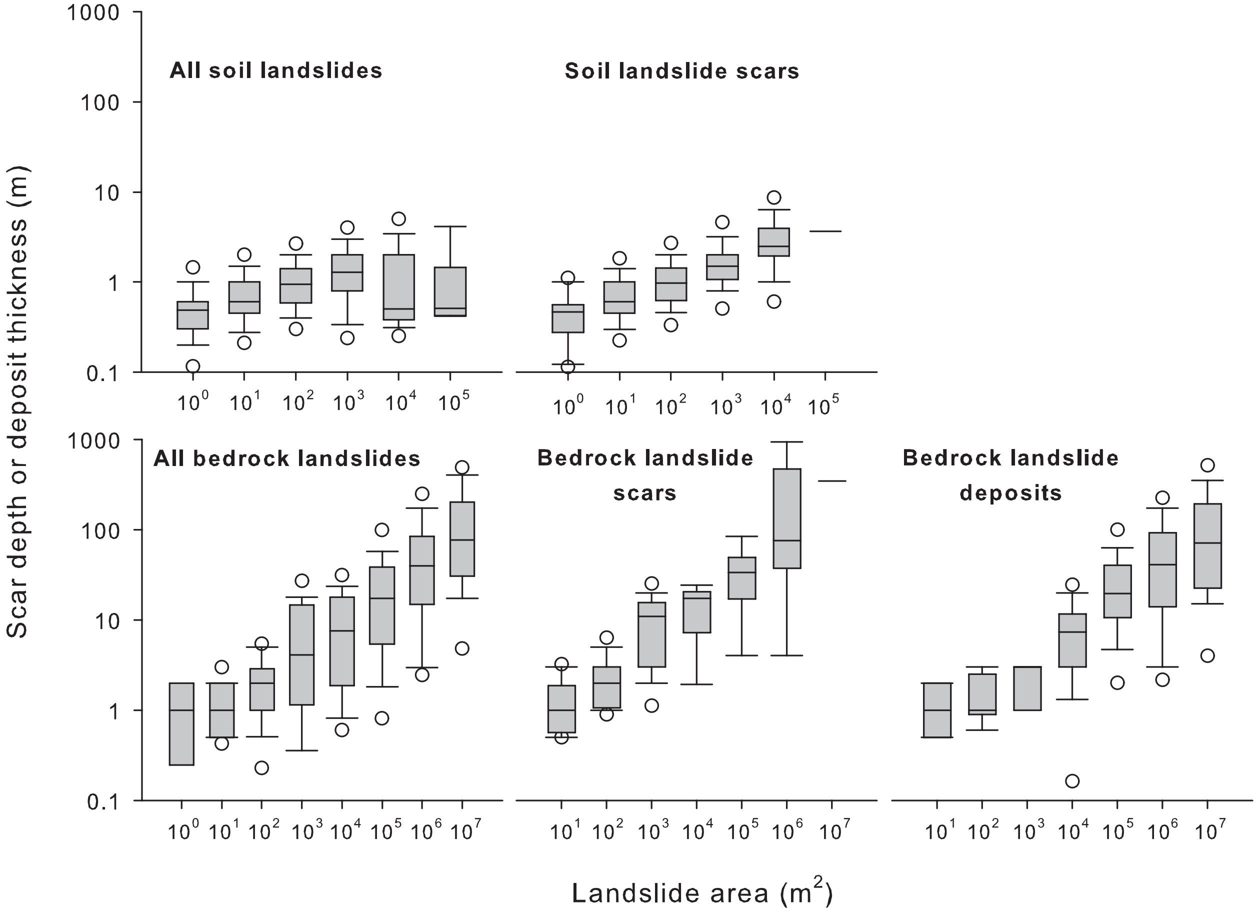

Figure 2.3. Box plots of landslide scar depth and deposit thickness as a function of landslide area for soil and bedrock landslides. Landslide areas are binned at one order of magnitude intervals. The horizontal line defines the median, for $n \geq 3$ the box defines the inter-quartile range, and for $n \geq 9$ the whiskers delineate the 10th and 90th percentiles and the circles delineate the 5th and 95th percentiles.

entrainment[25] has not introduced significant errors in our scaling relationships (Fig. A1.1).

Stratifying landslide data by region and dominant material confirms the trend in the combined, global data set and shows that for bedrock landslides γ_{rock} ranges from 1.3 to 1.6, whereas for soil landslides $\gamma_{\mathrm{soil}} = 1.1–1.4$ (Fig. 2.4). Self-similar scaling captures the central tendency in empirical γ-values for data sets consisting primarily of large bedrock landslides, but the large error bars do not allow us to resolve how generally self-similar scaling applies. The systematically lower γ-values show that self-similar scaling does not characterize soil landslides. We argue that the variation in γ for soil landslides reflects regional differences in soil thickness that limit landslide scar depths. For example, the lowest γ-values are from landscapes in British Columbia subject to Pleistocene glaciation and the semi-arid Transverse Ranges of southern California where soils tend to be thinner than in temperate-humid climates.

Systematic offsets in the peaks of estimated probability densities for global soil landslide and soil depths (Fig. 2.5a) support the notion that scar depths of shallow, primarily soil landslides are limited by soil thickness, and explain systematic differences between soil and bedrock landslide scaling. Regional data from the western U.S. show consistently that modal landslide scar depths are several decimeters less than modal soil depths (Fig. 2.5b–d). The limiting factor of soil thickness indicates soil landslides on soil-mantled hillslopes characterized by $\gamma < 1.3$ are transport-limited in the short-term if detaching less than the maximum soil depth, but supply-limited in the long-term as soil formation rates dictate the availability of detachable material[26]. If soil formation rates fail to match erosion rates, then bedrock failures with $\gamma > 1.4$ will characterize hillslope erosion, independent of soil cover or formation. The depth distributions for soil and bedrock landslide scars thus provide a physical explanation for variations in γ and we argue that γ is a metric capable of differentiating between these first order

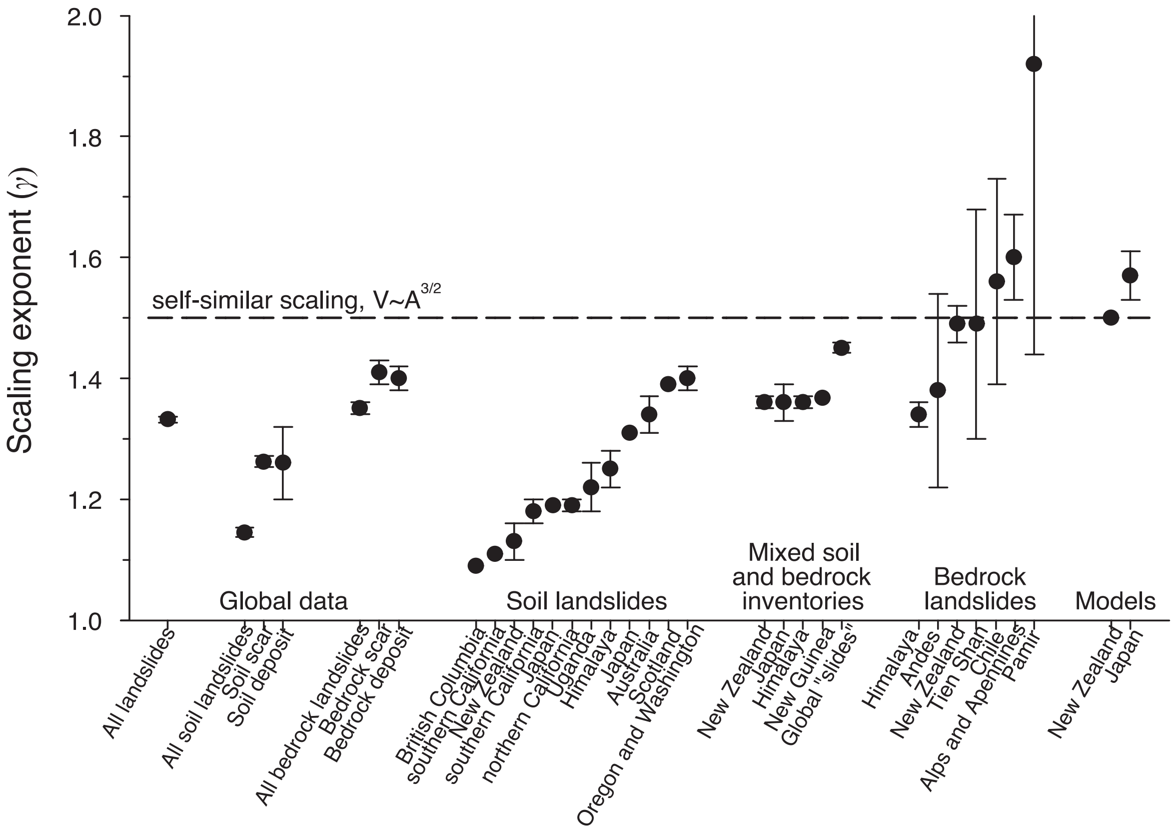

Figure 2.4. Scaling exponents (γ) from the landslide data sets used in this study, previous empirical studies and previous models. Landslide inventories are classified on the basis of the dominant landslide type. The circles are mean or reported values and the error bars denote one standard error or reported errors. The data sources are listed in Table A1.1 and the associated intercept (α) values are shown in Fig. A1.2.

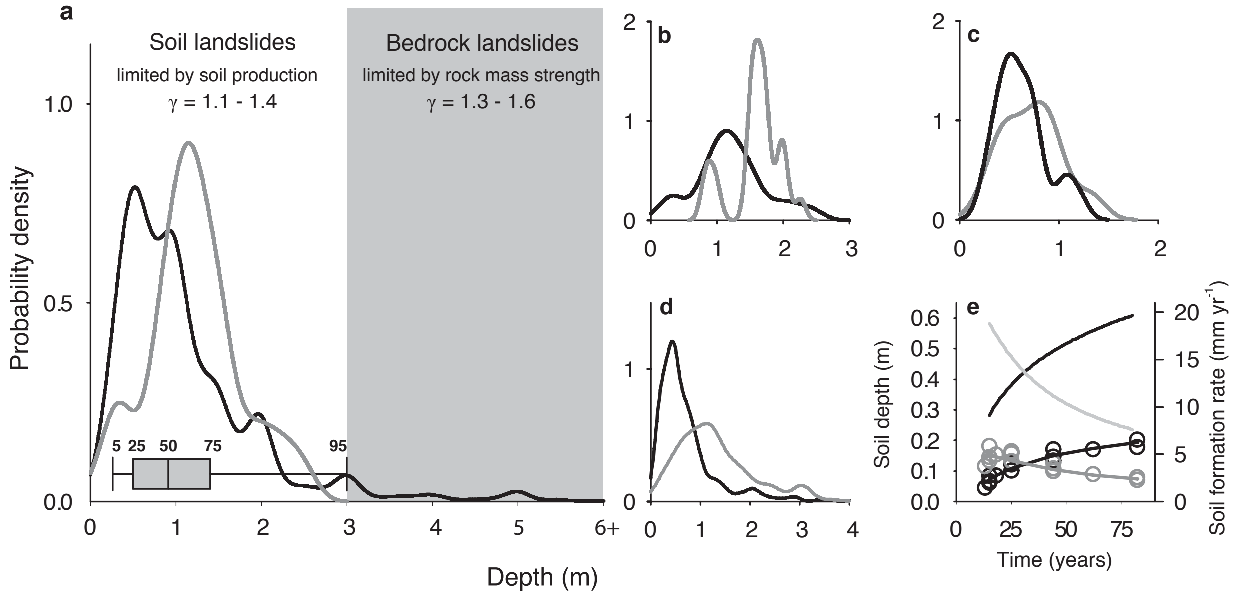

Figure 2.5. Soil and landslide depths. a–d, Gaussian kernel density estimates of landslide scar and soil depths for global soil landslides (*n* = 1,617; truncated at 6 m) and global soils (*n* = 83) for slope angles >20° (a), Redwood Creek, California (b), San Gabriel Mountains, California (c) and Oregon Coast Range (d). The black (grey) lines show landslide scar (soil) depth. The box plot shows the percentage of landslide depths that are less than the indicated value. The maximum soil depth in the global database and the 95th percentile soil landslide depth are both ~3 m. e, Soil depth (black) and rate of soil formation (grey) versus time since landsliding for landslide scars in Tairawhita[27] (upper curves) and Taranaki[28], New Zealand (lower curves).

material controls on hillslope erosion, thereby delimiting a transition that is central to understanding the production, transport and loss of soil and the resulting biogeochemical fluxes from mountain landscapes.

The view that only bedrock landslides can match river incision and exhumation rates in rapidly uplifting mountains[23] is supported by observations that bedrock-landslide inventories are dominated volumetrically by fewer, but larger failures more than are inventories of mixed or shallow landslides[20]. However, soil production rates decline exponentially as soil depth increases[24], so conversely, soil production should commensurately accelerate after landsliding removes the soil. Consequently, episodic soil landslides that reduce soil depths will increase rates of bedrock weathering in proportion to their frequency[7]. More frequent landslides will result in enhanced weathering[7] and we propose that bioturbation caused by root penetration into weathered and tectonically fractured bedrock drives rapid soil production in humid mountain belts. Indeed, soil residence times in rapidly uplifting, but soil-mantled landscapes can be as low as 100–200 yr (ref. 6). Rates of soil formation on landslide scars can increase to many times the long-term landscape erosion rates, reaching rates of 5–20 mm yr^{-1} in the century following failure[27,28] (Fig. 2.5e). Although some soil in landslide scars may derive from upslope soil erosion[27,28], such colluvial material helps accelerate soil production by providing substrate for rapid vegetation re-establishment[29]. Our data set lacks temporal information needed to assess volume-frequency relations for soil versus bedrock landslides, but recent modeling suggests smaller landslides (which tend to be soil failures) may occur frequently enough to contribute equally to denudation as larger failures[21]. We propose that rapid bedrock weathering and soil formation following soil landsliding may allow adjustments in landslide frequency to offset rock uplift without widespread, deep-seated bedrock failures by occurring at commensurately higher frequencies to counterbalance their lower volumetric contributions for a given failure area.

Quantification of the controls on landslide volume-area scaling highlights the importance of discriminating between soil and bedrock landslides when estimating erosion rates. Our analysis shows that soil depth limits the volume of material eroded from soil landslides and that the potential for rapid soil formation could allow soil landsliding to keep pace with rock uplift, even in the most tectonically active mountain ranges. The potential for both soil and bedrock landsliding to keep pace with rock uplift has important implications for soil residence times, biogeochemical cycling and landscape evolution in mountain belts.

Methods

Sensitivity analysis. We created synthetic power-law distributed landslide inventories (n = 10,000 each) over a pre-defined range of non-cumulative area-frequency scaling exponents (β = 1.5, 2.0 and 2.5) and landslide areas (10^3 m^2 < A_l <10^6 m^2), thus encompassing most published inventories. We used different values of γ (with intercept 0.02 m$^{3-2\gamma}$) and computed the ratio of V_T for $\gamma = 1.5$ over V_T for a range of reported values of γ to determine how variation in γ affects total landslide volume for the synthetic landslide inventories. The range of $V_T(\gamma = 1.5)/V_T(\gamma)$ ratios shown by the boxes and whiskers is for 30 randomly generated inventories of A (all with β = 2.5; n = 10,000 and 10^3 m^2 < A <10^6 m^2) for a fixed γ. See Appendix 1 for information on empirical inventories. Note that the Northridge landslide inventory has β = 2.4 only over a limited area range, hence the slightly higher apparent value of β.

Landslide geometry. Measurements of the area, thickness and volume of landslide scars and deposits were obtained from publications, digitized from published figures and our own field measurements (see Table A1.1 for data sources). Data are based on individual measurements and not on extrapolation. Landslide is defined broadly to include rotational, translational, flow and avalanche failures in earth, debris and bedrock[30]. We calculated landslide volume as the product of scar area and mean scar depth or deposit area and mean deposit thickness, depending on the available data. However, for some data sets landslide area was not defined or was based on the total area disturbed. All data were used to determine the relationship shown in Fig. 2.2. We further distinguished: (1) bedrock failures, (2) 'soil' failures within unconsolidated soil, regolith or colluvium and (3) undifferentiated failures (Fig. A1.3), as well as data based on: (1) the failure scar geometry, (2) the deposit geometry and (3) other or undefined geometries (Fig. A1.4). Reduced major axis regression on log-transformed data was used to determine the scaling parameters γ and α for different study regions grouped by dominant landslide material (Figs A1.5-A1.7). Scaling exponents were considered to be significantly different if the 95% confidence intervals did not overlap.

Soil depths. The distribution of global soil landslide scar depths (n = 1,617) was compared against 83 global upland soil depth values from slopes >20° using Gaussian kernel density estimation. Landslide (n = 898) and soil depth (n = 23) distributions were also compared for Redwood Creek, California, where landslide and soil depth data were available for the same watershed, and for the San Dimas Experimental Forest, California (n = 29) and the Oregon Coast Range (n = 287), where landslide and soil depths were measured at individual failures (see Appendix 1 for data sources). Soil depths for Redwood Creek were based on soil pits on slopes >20°. The pits did not always reach unweathered bedrock and thus, in some cases, soil depths are minimum values.

References

1. Burbank, D. et al. Bedrock incision, rock uplift and threshold hillslopes in the northwestern Himalayas. *Nature* 379, 505-510 (1996).
2. Hovius, N., Stark, C. & Allen, P. Sediment flux from a mountain belt derived by landslide mapping. *Geology* 25, 231-234 (1997).
3. Schmidt, K. & Montgomery, D. Limits to relief. *Science* 270, 617-620 (1995).
4. Whipple, K., Kirby, E. & Brocklehurst, S. Geomorphic limits to climate-induced increases in topographic relief. *Nature* 401, 39-43 (1999).
5. Korup, O. et al. Giant landslides, topography, and erosion. *Earth. Planet. Sci. Lett.* 261, 578-589 (2007).
6. Basher, L., Tonkin, P. & McSaveney, M. Geomorphic history of a rapidly uplifting area on a compressional plate boundary: Cropp River, New Zealand. *Z. Geomorphol.* 69, 117-131 (1988).
7. Gabet, E. A theoretical model coupling chemical weathering and physical erosion in landslide-dominated landscapes. Earth. Planet. Sci. Lett. 264, 259-265 (2007).
8. Raymo, M. & Ruddiman, W. Tectonic forcing of late Cenozoic climate. *Nature* 359, 117-122 (1992).
9. Hilton, R. et al. Tropical-cyclone-driven erosion of the terrestrial biosphere from mountains. *Nature Geosci*. 1, 759-762 (2008).
10. Hilton, R., Galy, A. & Hovius, N. Riverine particulate organic carbon from an active mountain belt: Importance of landslides. *Glob. Biogeochem. Cycles* 22, GB1017 (2008).
11. Willett, S. D., Hovius, N., Brandon, M. T. & Fisher, D. M. Tectonics, Climate and Landscape Evolution (Geol. Soc. Am., 2006).
12. Blaschke, P., Trustrum, N. & Hicks, D. Impacts of mass movement erosion on land productivity: A review. *Prog. Phys. Geog.* 24, 21-52 (2000).
13. Malamud, B., Turcotte, D., Guzzetti, F. & Reichenbach, P. Landslide inventories and their statistical properties. *Earth Surf. Processes Landforms* 29, 687-711 (2004).
14. Hovius, N., Stark, C., Hao-Tsu, C. & Jiun-Chuan, L. Supply and removal of sediment in a landslide-dominated mountain belt: Central Range, Taiwan. *J. Geol*. 108, 73-89 (2000).
15. Lavé, J. & Burbank, D. Denudation processes and rates in the Transverse Ranges, southern California: Erosional response of a transitional landscape to external and anthropogenic forcing. *J. Geophys. Res*. 109, F01006 (2004).
16. Imaizumi, F. & Sidle, R. Linkage of sediment supply and transport processes in Miyagawa Dam catchment, Japan. *J. Geophys. Res*. 112, F03012 (2007).
17. Simonett, D. in Landform studies from Australia and New Guinea (eds Jennings, J. N. & Mabbutt, J. A.) 64-84 (Australian National Univ. Press, 1967).
18. Niemi, N., Oskin, M., Burbank, D., Heimsath, A. & Gabet, E. Effects of bedrock landslides on cosmogenically determined erosion rates. *Earth. Planet. Sci. Lett*. 237, 480-498 (2005).
19. Yanites, B., Tucker, G. & Anderson, R. Numerical and analytical models of cosmogenic radionuclide dynamics in landslide-dominated drainage basins. *J. Geophys. Res*. 114, F01007 (2009).
20. Dussauge, C., Grasso, J. & Helmstetter, A. Statistical analysis of rockfall volume distributions: Implications for rockfall dynamics. *J. Geophys. Res*. 108, 2286 (2003).
21. Stark, C. & Guzzetti, F. Landslide rupture and the probability distribution of mobilized

debris volumes. *J. Geophys. Res*. 114, F00A02 (2009).

22. Guzzetti, F., Ardizzone, F., Cardinali, M., Rossi, M. & Valigi, D. Landslide volumes and landslide mobilization rates in Umbria, central Italy. *Earth Planet. Sci. Lett*. 279, 222-229 (2009).
23. Burbank, D. Rates of erosion and their implications for exhumation. *Mineral. Mag*. 66, 25-52 (2002).
24. Heimsath, A., Dietrich, W., Nishiizumi, K. & Finkel, R. The soil production function and landscape equilibrium. *Nature* 388, 358-361 (1997).
25. Hungr, O. & Evans, S. Entrainment of debris in rock avalanches: An analysis of a long run-out mechanism. *Geol. Soc. Am. Bull*. 116, 1240-1252 (2004).
26. Carson, M. & Kirkby, M. Hillslope Form and Process (Cambridge Univ. Press, 1972).
27. Smale, M., McLeod, M. & Smale, P. Vegetation and soil recovery on shallow landslide scars in Tertiary hill country, East Cape Region, New Zealand. *New Zeal. J. Ecol*. 21, 31-41 (1997).
28. Trustrum, N. A. & De Rose, R. C. Soil depth-age relationship of landslides on deforested hillslopes, Taranaki, New Zealand. *Geomorphology* 1, 143-160 (1988).
29. Restrepo, C. et al. Landsliding and its multiscale influence on mountainscapes. *Bioscience* 59, 685-698 (2009).
30. Cruden, D. & Varnes, D. in Landslides Investigation and Mitigation. Special Report 247 (eds Turner, A. K. & Schuster, R. L.) 36-71 (Transportation Research Board, National Research Council, National Academy Press, 1996).

CHAPTER 3

Landslide erosion coupled to tectonics and river incision

The steep topography of mountain landscapes arises from interactions among tectonic rock uplift, valley incision and landslide erosion on hillslopes. Hillslopes in rapidly uplifting landscapes are thought to respond to river incision into bedrock by steepening to a maximum stable or 'threshold' angle[1–3]. Landslide erosion rates are predicted to increase nonlinearly as hillslope angles approach the threshold angle[1–7]. However, the key tenet of this emerging threshold hillslope model of landscape evolution—the coupled response of landslide erosion to tectonic and fluvial forcing—remains untested. Here we quantify landslide erosion rates in the eastern Himalaya, based on mapping more than 15,000 landslides on satellite images. We show that landslide erosion rates are significantly correlated with exhumation rates and stream power and that small increases in mean hillslope angles beyond 30° translate into large and significant increases in landslide erosion. Extensive landsliding in response to a large outburst flood indicates that lateral river erosion is a key driver of landslide erosion on threshold hillslopes. Our results confirm the existence of threshold hillslopes and demonstrate that an increase in landslide erosion rates, rather than steepened hillslope angles, is the primary mechanism by which steep uplands respond to and balance rapid rates of rock uplift and bedrock river incision in tectonically active mountain belts.

The threshold hillslope paradigm is rooted in the observation that hillslope angles throughout mountainous landscapes tend to be symmetrically distributed about a mean value with a mode comparable to the friction angle of granular material[1,2,8–10]. In contrast to how hillslope angles and erosion rates increase linearly to keep pace with rock uplift in landscapes with low to moderate tectonic forcing[3,5–7,11], at high uplift rates hillslope angles are thought to be limited by material strength[12], so hillslopes will approach the threshold angle and erosion rates will increase nonlinearly such that the relationship between erosion rates and slope angles approaches asymptotic. Vertical river incision into bedrock is thought to over-steepen hillslopes with gradients near the threshold angle, increasing relief until gravitational stress exceeds material strength and bedrock landsliding occurs[1]. Hence landscapes with hillslope gradients near the threshold angle are thought to respond to increases in uplift-driven river incision by increasing landslide erosion rates, rather than by steepening[1,3,5]. Implicit in the threshold hillslope model are the assumptions that landslide erosion rates spatially track rates of river incision and that landslide erosion rates increase nonlinearly as hillslope gradients approach the threshold angle. In steady-state landscapes, the threshold hillslope model also predicts that landslide erosion rates are spatially coupled with exhumation and rock uplift rates. Strong indirect support for threshold hillslopes exists in the form of an independence of hillslope angles on river incision and exhumation rates[1], correlation of landslide density with exhumation and surface uplift rates[9], nonlinear relationships between erosion rates and hillslope angles[3–7,11] and the finding that landslide erosion rates can match high rates of landscape denudation[13]. However, direct coupling of landslide erosion with river incision and exhumation and the nature of the coupling have not been demonstrated.

We tested the threshold hillslope concept in the eastern Himalaya where the Yarlung Tsangpo River cuts through the Namche Barwa-Gyala Peri massif (Fig. 3.1a). Here the Tsangpo

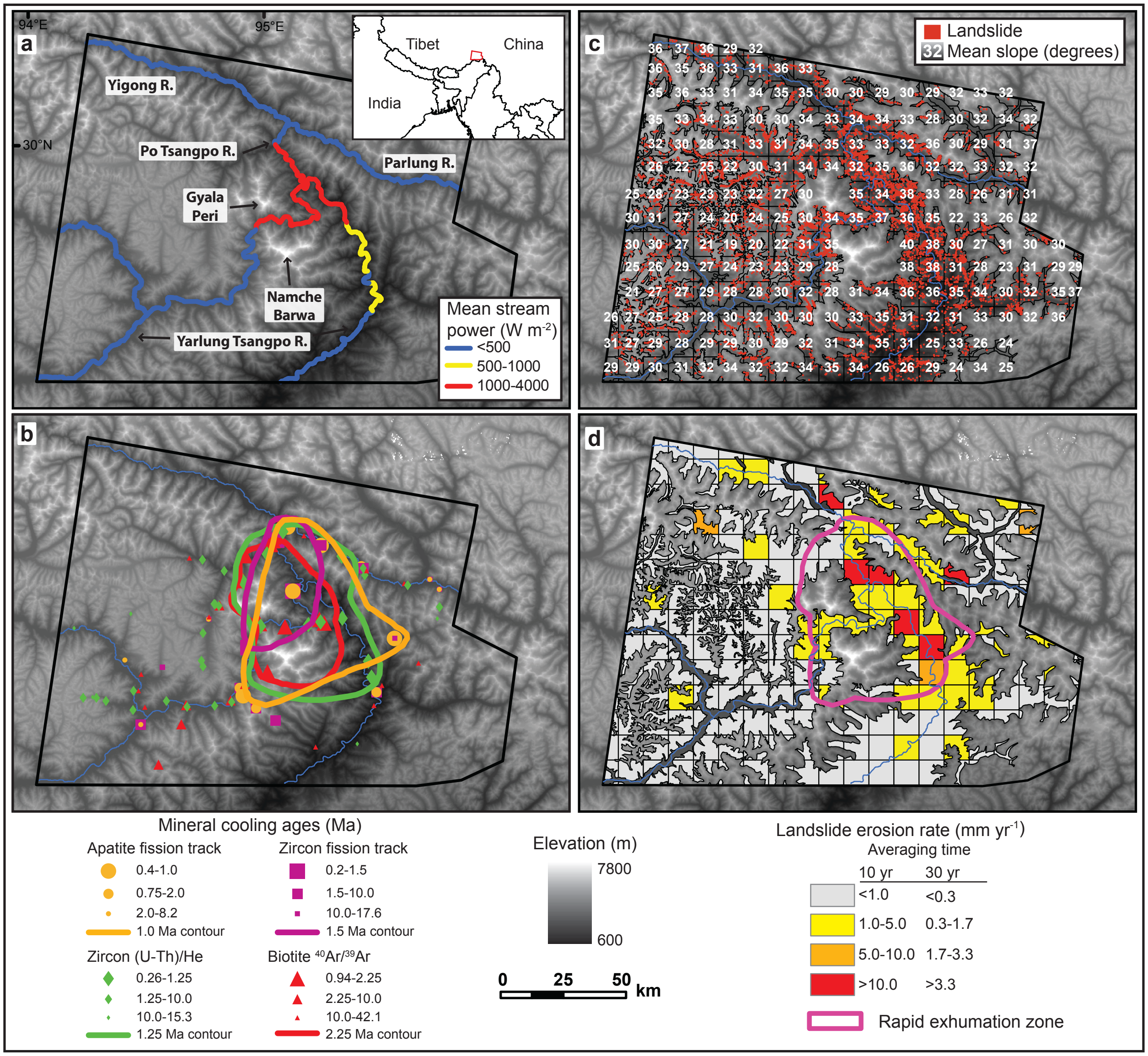

Figure 3.1. Spatial patterns of stream power, mineral cooling ages, hillslope angles and pre-1974 landslide erosion rates in the eastern Himalaya. a, Stream power[16]. b, Mineral cooling ages[16–18]. c, Mean hillslope angles. d, Pre-1974 landslide erosion rates. The mineral cooling age contours correspond approximately to a 2 mm yr^{-1} exhumation rate and delineate the high versus low exhumation zones (see Methods).

River drops 2 vertical kilometres within the Tsangpo Gorge[14], where close spatial coupling among high topographic relief, high unit stream power[15,16] and young mineral cooling ages[17,18] suggest high rates of erosion are closely linked with crustal deformation, metamorphism and rapid exhumation[19]. Moreover, the thermochronology (Fig. 3.1b) and stream power data indicate exhumation and river incision within the eastern Himalaya vary spatially by orders of magnitude[16], whereas mean slope angles vary little (Fig. 3.1c), making the landscape ideal for testing the threshold hillslope model with landslide erosion data. We quantified multi- decadal landslide erosion rates by generating two inventories of landslide areas: an inventory of 15,257 landslides that occurred before 1974 and an inventory of 558 landslides that occurred between 1974 and 2007. We used the spatial distribution of predicted landslide volumes as a proxy for spatially averaged erosion rates and assessed regional ($>10^3$ km^2) and local (≤ 100 km^2) spatial coupling among landslide erosion, hillslope angles, stream power and exhumation rates to determine whether the eastern Himalaya harbours threshold hillslopes.

The pre-1974 landslide data show that high rates of landslide erosion are spatially focused within a ~2,000 km^2 region of rapid exhumation along the Yarlung Tsangpo and Po Tsangpo rivers (Fig. 3.1d). The time period over which the pre-1974 landslides occurred is unknown, but 30 yr provides a limiting constraint (see Methods). To account for infrequently occurring large landslides ‘missing’ from our inventory because of the short temporal scale of observation, we assume the landslides occurred over three decades and integrate landslide magnitude-frequency distributions following the methodology of refs. 13 and 20, which yields erosion rates within the zone of high exhumation of 2–6 mm yr^{-1} (see Appendix 2). Erosion rates outside the zone of high exhumation are 0.3–1.0 mm yr^{-1} and are locally greater where large, isolated landslides occur on glacially steepened valley walls. Comparison of the distributions of local-scale erosion rates indicates that median landslide erosion rates within the high exhumation zone are significantly greater by a factor of four than landslide erosion rates outside this region (Fig. 3.2a).

The 1974–2007 landslide data indicate that the highest landslide erosion rates occur along the Po Tsangpo River downstream from Zhamu Creek (Fig. A2.1), a tributary of the Yigong River, where a large landslide dam[21] breached catastrophically in 2000. The ensuing outburst flood caused extensive landslide erosion; field inspection of sites along the upstream path of the flood indicated the toes of soil-mantled hillslopes were scoured to fresh bedrock, which triggered translational landslides that were identified on satellite images. Landslide erosion rates locally reach 15 mm yr^{-1} for 10-km-long river reaches during the 33-yr period (Fig. 3.3) and the flood-induced landslides account for ~70% of the landslide erosion in the high exhumation zone (Table A2.1). Landslide erosion rates in the high exhumation region were 4–21 mm yr^{-1} from 1974 to 2007, whereas rates in the low exhumation zone were estimated to be 1–4 mm yr^{-1}. Although the spatial maxima in landslide erosion are similar for both landslide inventories (Fig. 3.1d and Fig. A2.1), the pre-1974 landslide inventory provides a more representative view of the spatial pattern of landslide erosion because the outburst flood influenced the 1974–2007 erosion pattern.

The large differences in landslide erosion between the high and low exhumation zones exist despite only a 3° difference in the modal hillslope gradient of the two regions (Fig. 3.2b). Hillslopes in the high exhumation zone have a very limited capacity to steepen in response to rock uplift and river incision, as reflected in the close correspondence between the landslide and landscape-wide slope angle distributions.

The spatial focus of high landslide erosion rates from both landslide inventories

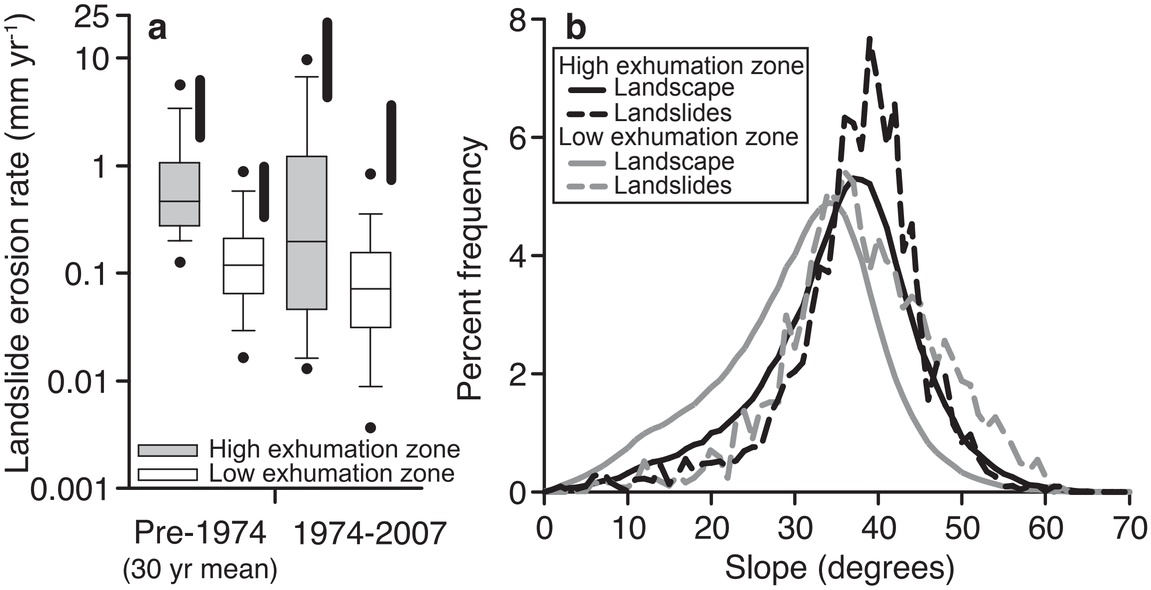

Figure 3.2. Landslide erosion rate and hillslope angle distributions for the high and low exhumation zones. a, Distributions of landslide erosion rates from each grid cell are depicted with boxplots; lines to the right of each boxplot show the range of erosion rates estimated by integration of landslide volume-frequency distributions (see Appendix 2). The boxes span the inter-quartile range, the line denotes the median, whiskers denote 10th and 90th percentiles and circles denote 5th and 95th percentiles. Each pair has significantly different medians ($p \leq 0.001$; see Methods). b, Hillslope angle distributions for the high exhumation zone (mode = 37°), 1974–2007 high exhumation zone landslides (mode = 39°), low exhumation zone (mode = 34°) and 1974–2007 low exhumation zone landslides (mode = 36°). The Zhamu Creek landslide accounts for ~65% of the 1974–2007 low exhumation zone landslide slope data. Excluding the Zhamu Creek landslide has a minimal influence of the mode, but reduces the mean slope angle by ~3°.

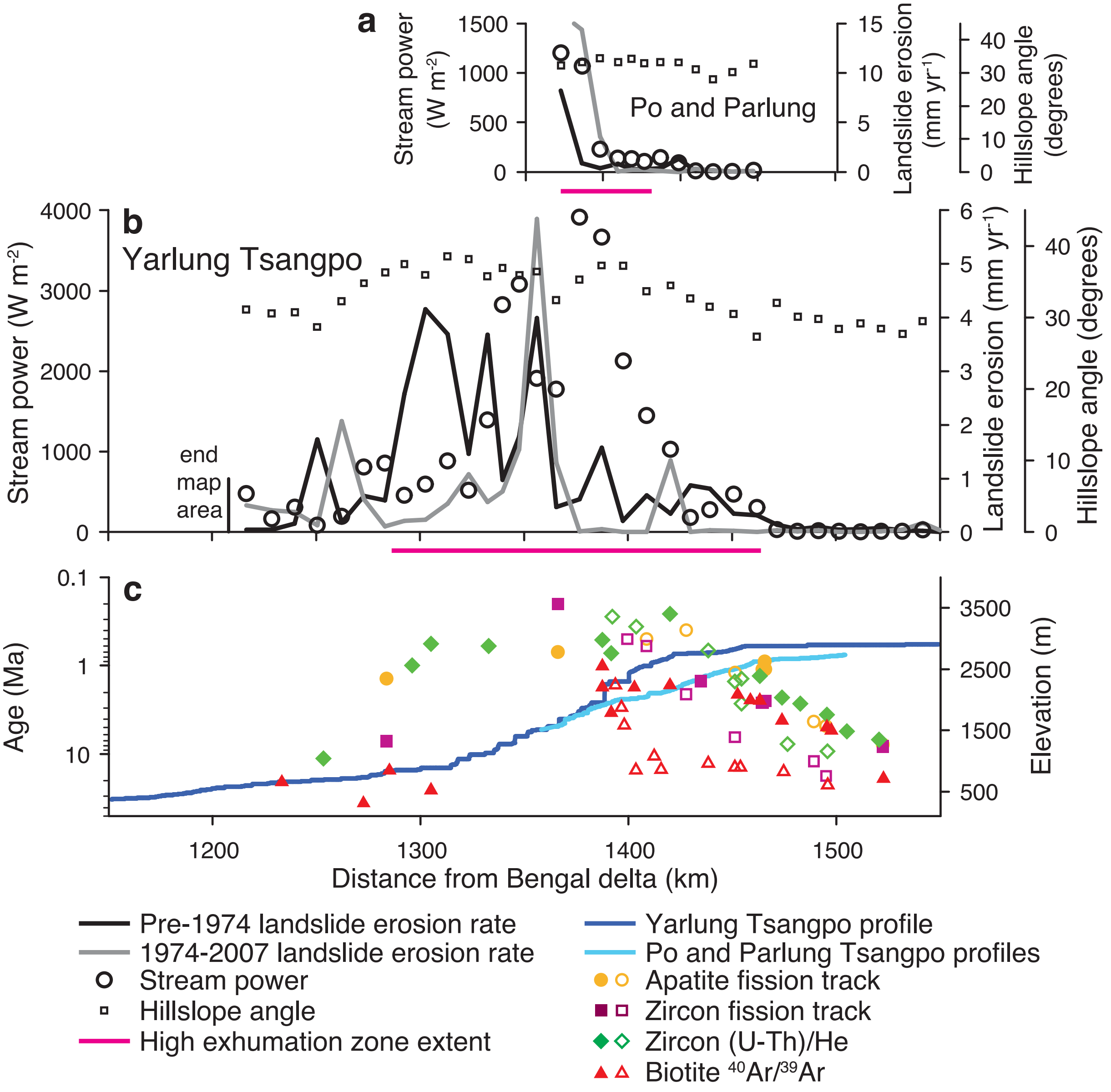

Figure 3.3. Patterns of landslide erosion, hillslope angles, stream power and mineral cooling ages along the long profiles of the Yarlung Tsangpo and Po and Parlung Tsangpo rivers. a,b, Landslide erosion rate, stream power[16] and hillslope angle for the Po and Parlung Tsangpo rivers (a) and Yarlung Tsangpo (b). c, River long profile and mineral cooling age data[16–18]; filled symbols correspond to the Yarlung Tsangpo and open symbols correspond to the Po and Parlung Tsangpo rivers.

corresponds to the high exhumation zone, where mineral cooling ages[16-18] are significantly younger than cooling ages from the surrounding landscape (Fig. A2.2). Hence decadal-scale landslide erosion rates and exhumation rates averaged over 10^5-10^6 yr timescales exhibit a significant degree of regional-scale spatial coupling. Estimates of exhumation rates in the eastern Himalaya range from 2 to 9 mm yr^{-1} (refs. 17,18,22). The multi-decadal landslide erosion rates within the high exhumation zone are of comparable magnitude to long-term exhumation rates, confirming that landslide erosion sustains rapid exhumation in the eastern Himalaya.

Local-scale landslide erosion rates increase weakly, but significantly with increasing exhumation rate for the lower temperature thermochronometers (Fig. 3.4a-c). The correlation between landslide erosion and exhumation rates generally declines as closure temperatures increase and there is no significant correlation for the highest temperature thermochronometer, biotite $^{40}Ar/^{39}Ar$ (Fig. 3.4d), indicating a limit to the fidelity at which thermochronometers track modern rates of surface processes, and hence the present topography, as the timescale of exhumation increases. This limiting timescale is approximately the time required to erode through the equivalent of the modern topographic relief, as the biotite $^{40}Ar/^{39}Ar$ closure depth and landscape relief[19] are both of the order of 3.5−7 km in the eastern Himalaya.

The highest landslide erosion rates exhibit a general spatial association with maxima in unit stream power that occur on the Yarlung and Po Tsangpo knickzones (Fig. 3.3). The landslide data indicate a clear increase in landslide erosion with increasing stream power for the Po Tsangpo and Parlung rivers. Along the Yarlung Tsangpo there is a general trend of increased landslide erosion where stream power is greatest, but individual reaches with high stream power do not always exhibit high landslide erosion rates, which may be due to the relatively short record of landslide occurrence and the stochasticity of landslide-triggering events or potential

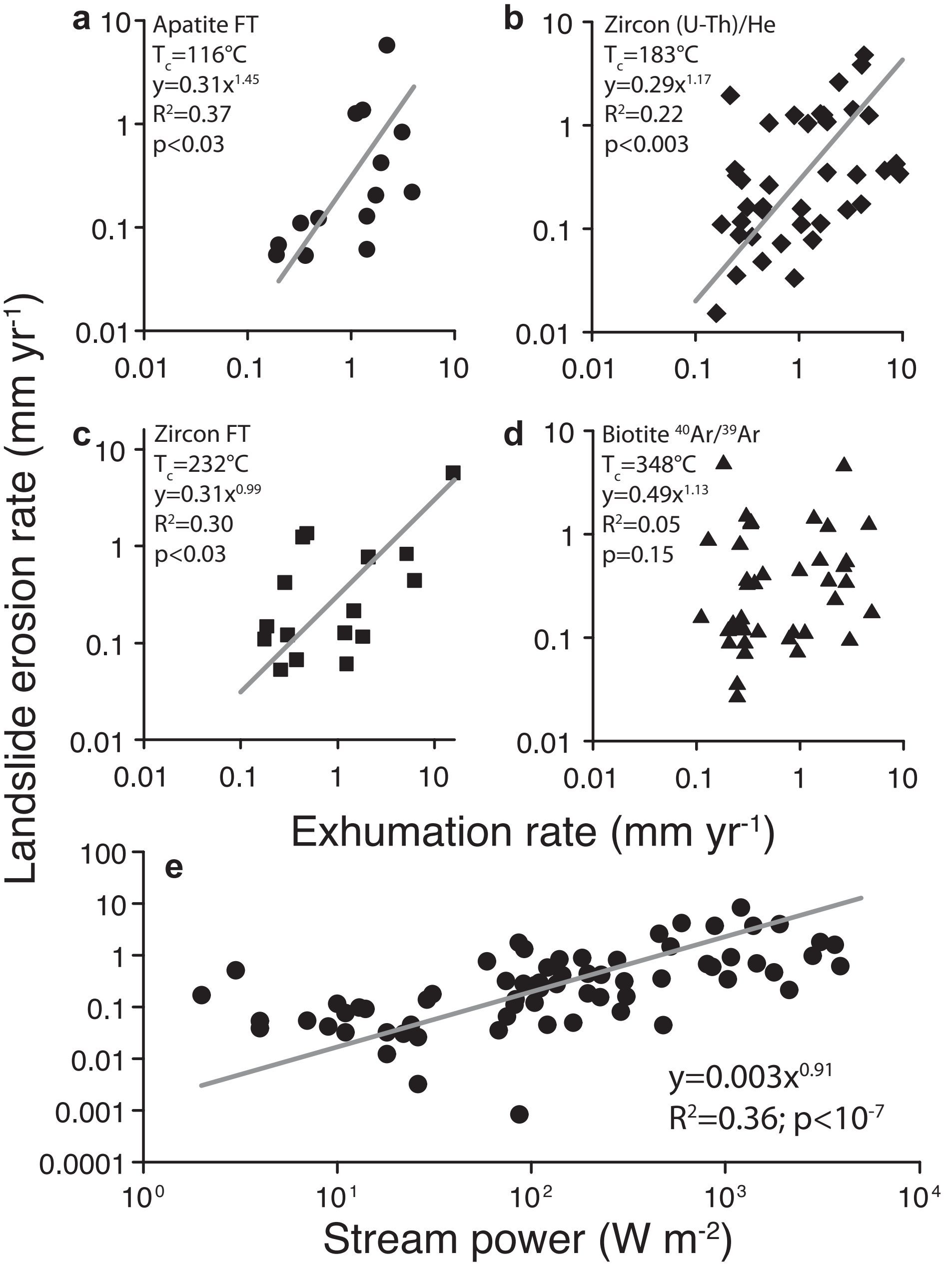

Figure 3.4. Landslide erosion rate versus exhumation rate and stream power. a–d, Pre-1974 landslide erosion rates versus exhumation rates for apatite fission track (FT) (a), zircon (U-Th)/He (b), zircon fission track (c) and biotite ^{40}Ar/^{39}Ar (d) thermochronometers. Closure temperature (T_c) values are from ref. 29. e, Pre-1974 landslide erosion rates versus stream power. Lines are shown only for significant regression relationships.

under-sampling of landslides on the steep hillslopes in this area. However, local-scale landslide erosion rates increase significantly with increasing stream power (Fig. 3.4e), indicating that stream power and landslide erosion are spatially coupled. The spatial correlation of young mineral cooling ages and high stream power has been cited as strong evidence that river incision drives landscape lowering in the eastern Himalaya and stream power seems to be a reasonable proxy for long-term fluvial incision in this region[16]. The correlation between landslide erosion rates and stream power supports this view, indicating that vertical river incision is a mechanism that drives landslide erosion on threshold hillslopes over long timescales.

Many of the flood-triggered landslides were located on the outside of meander bends (Fig. A2.3), suggesting lateral scour of regolith played an important role in destabilizing hillslopes. As for vertical channel incision, lateral erosion of hillslope toes increases hillslope gradients, causing landslides from hillslopes in the eastern Himalaya that have little capacity to steepen. Hence there are two mechanisms by which river incision drives erosion on threshold hillslopes, the conventional vertical bedrock incision mechanism, and the lateral erosion mechanism demonstrated by the Zhamu Creek outburst flood. The lateral erosion mechanism requires that rates of regolith (soil and fractured rock) production keep pace with landscape lowering, which is a reasonable expectation, given the lack of bedrock outcrops on the hillslopes in the sub-alpine portion of the Tsangpo Gorge, as well as documentation in other rapidly uplifting mountain belts of extensively fractured subsurface bedrock[10] and rapid soil production[23,24]. Furthermore, repeated failure of glacier dams upstream from the Tsangpo Gorge released floods 2–3 orders of magnitude greater than the Zhamu Creek outburst flood[25]. There are hundreds of breached natural dams upstream from the Tsangpo Gorge[26], suggesting that outburst floods occur often enough to allow lateral erosion to be an important mechanism for driving landslide erosion of threshold hillslopes in this region.

Landslide erosion rates are low where mean hillslope angles are less than 30°, but increase nonlinearly where hillslope angles exceed 30° (Fig. 3.5a), with small increases in hillslope angles leading to large and significant increases in landslide erosion rates (Fig. 3.5b). This erosion-slope relationship is consistent with previous studies[3–7,11] but demonstrates for the first time that adjustment of landslide erosion rates is the mechanism by which hillslopes with gradients near a strength-limited angle respond to spatially variable exhumation rates, and hence provides critical empirical evidence needed to validate the threshold hillslope model.

The spatial coupling among landslide erosion, stream power and mineral cooling ages indicates a strong link exists among landslide erosion, river incision and exhumation. This link is significant, despite the stochastic nature of landslide-triggering events and the short decadal timescale encompassed by our landslide erosion data. Furthermore, the extensive landslide erosion triggered by the Zhamu Creek outburst flood demonstrates that many hillslopes in the eastern Himalaya are indeed close to the threshold of stability and that lateral erosion by extreme floods is a key mechanism for coupling fluvial and hillslope erosion. The spatial coupling of landslide erosion rates, stream power and exhumation rates confirms that uplands in tectonically active mountain belts balance rapid rates of rock uplift and river incision through adjustment of landslide erosion rates on threshold hillslopes.

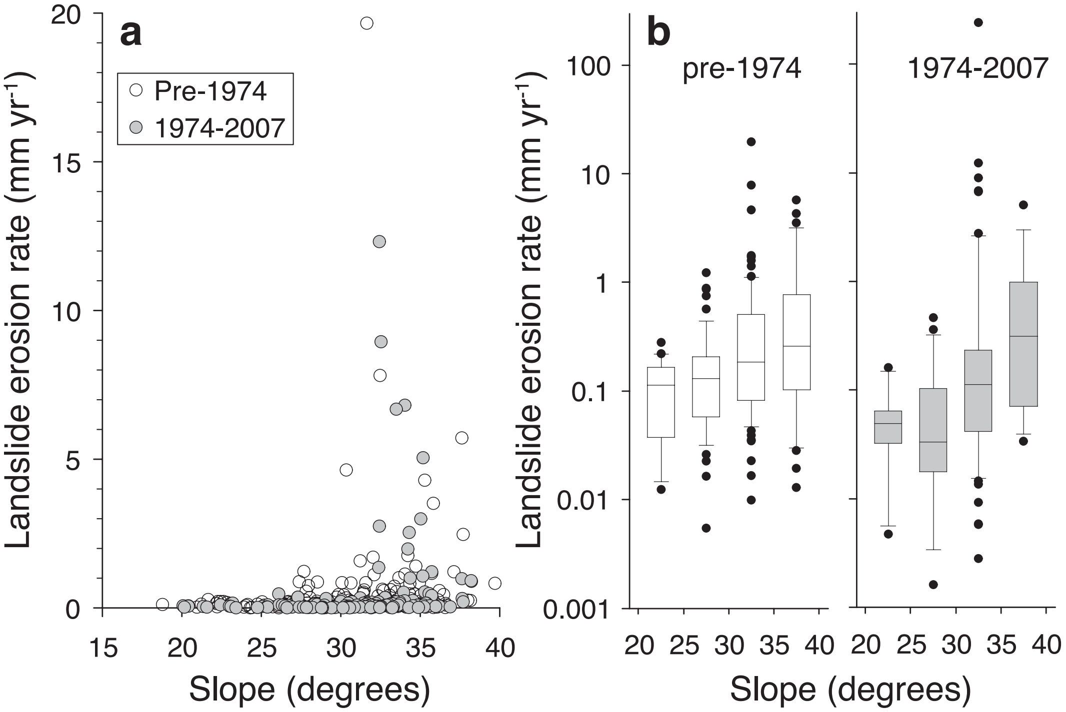

Figure 3.5. Landslide erosion rates as a function of hillslope angle. a, Landslide erosion rate versus hillslope angle for the pre-1974 (*n* = 201) and 1974-2007 (*n* = 123) inventories. Data are mean values for individual grid cells. b, Distribution of landslide erosion rates as a function of hillslope angle. For both landslide data sets, rates for 20–25° and 25–30° slopes are not significantly different ($p > 0.1$), nor are erosion rates for 30–35° and 35–40° slopes ($p > 0.3$). Erosion rates for 30–35° and 35–40° slopes are significantly greater than rates for 20–25° and 30–35° slopes in both cases ($p < 0.03$). The boxes span the inter-quartile range, the line denotes the median, whiskers denote 10^{th} and 90^{th} percentiles and circles denote outliers. Pre-1974 data average landslide erosion over a 30-yr period. Grid cells with no mapped landslides are not included in the 1974–2007 erosion data, and data for the grid cell with the Zhamu Creek landslide (erosion rate = 241 mm yr^{-1}, slope = 31°) are not shown in a.

Methods

Landslide erosion. The pre-1974 landslide inventory was generated by mapping all landslides visible on ~4-m-pixel-resolution Keyhole-9 Hexagon (KH-9) images. Two KH-9 images, one from 1973 and one from 1975 provide coverage of the entire area of this inventory. The 1974–2007 landslide inventory was generated by mapping landslides on Landsat (1990, 2000, 2001) and Advanced Spaceborne Thermal Emission and Reflection Radiometer (ASTER; 2001, 2004, 2005, 2007) images, which have a 15-m-pixel resolution, with the exception of the 1990 Landsat image, which has a 30-m-pixel resolution. The 1974–2007 inventory is limited to those landslides that were not present on the 1973/1975 KH-9 images. Landslides were identified on the basis of the distinct spectral signature of soil and rock relative to vegetation; alpine areas above tree line were excluded from the analysis. Landslide scars were mapped and were distinguished from deposits to the extent possible based on downslope changes in the shape and spectral brightness of the disturbed area. Landslide areas were converted to volumes using volume-area scaling relationships. Local-scale erosion rates for each grid cell (see below) were calculated using a volume-area scaling relationship based on 428 measurements of soil and bedrock landslides from the Himalaya[23] (see Appendix 2 for details and erosion rate estimates based on alternative volume-area scaling relationships). Regional-scale landslide erosion rates for the high and low exhumation zone were calculated by means of integration of landslide volume-frequency distributions[20] (see Appendix 2) and the ranges of values are based on multiple volume-area scaling relationships. The mean depth of material eroded by landslides was determined by summing the landslide volume within each grid cell or region and dividing by the grid cell or region area. The resulting depth of eroded material was converted to an erosion rate by dividing by the time over which the landslides occurred. For the 1974–2007 landslide inventory this was 33 yr, the time between the mean acquisition year of the KH-9 images and the most recent ASTER image. An averaging time of 30 yr was used to assess erosion rates represented by the pre-1974 landslide inventory, which we consider to be a reasonable limiting value for reasons discussed below. The similarity in the power-law portion of the landslide frequency-area distributions for the pre-1974 and 1974–2007 landslide inventories (Fig. A2.5 inset) indicates that these two inventories from different resolution images are drawn from a similar number of landslides[20]. Hence if landslide frequency were similar for the two inventories, landslides in the pre-1974 inventory would have occurred over ~3 decades. Repeat satellite images indicate some landslide scars can revegetate within a decade (Fig. A2.3), suggesting a shorter averaging time and hence higher erosion rates. As a result of uncertainty in the time over which the pre-1974 landslides occurred, we present erosion rates based on the range of averaging times of 10–30 yr (Fig. 3.1d). As vegetation, cloud cover, topographic shading and other factors can limit landslide detection, we consider the landslide erosion rates for both inventories to be minimum values.

Hillslope angles, stream power and mineral cooling ages. The landscape was divided into 10 km x 10 km grid cells that were clipped to remove areas above tree line and floodplains. Hillslope angles were extracted from the 3 arc-second Shuttle Radar Topography Mission (SRTM) digital elevation model (DEM) with data gaps filled using topographic line data from www.viewfinderpanoramas.org. The clipped 3 arc-second data were used to generate hillslope angle distributions for the high and low exhumation zones and for landslides in the 1974-2007 inventory (hillslope angle distributions were not extracted for the pre-1974 landslide inventory because parallax caused by high topographic relief led to small georeferencing errors and hence misalignment of the KH-9 images and DEM). Slope values averaged over each clipped grid cell were used to assess the relationship between landslide erosion rate and slope in Fig. 3.5. In addition to alpine areas and floodplains, the bottoms of small valleys were excluded from mean slope calculations by generating a stream network with a threshold contributing area of 8.1 km^2 with streams that terminated in low-gradient valley heads. Areas within 100 m of the streams were excluded from slope calculations. Mean hillslope gradients for areas within 5 km of either side of the channels were projected onto the river long profile after calculating the mean angle for hillslopes adjacent to each segment. Unit stream power data are primarily from ref. 16 but were augmented with values modeled for 10-km-long stream segments following ref. 27 by routing Tropical Rainfall Measuring Mission rainfall estimates from ref. 28 through the World Wildlife Fund-U.S. Geological Survey hydrologically conditioned SRTM DEM. Landslides ≤5 km from rivers were used to calculate erosion rates for 10-km-long stream segments. Mineral cooling data from refs. 16 to 18 were used to delineate cooling age contours. The cooling age contours approximately delineate an exhumation rate of ~2 mm yr^{-1}. The fault-bounded core of the Namche Barwa-Gyala Peri antiform has been exhumed at a rate of at least 2 mm yr^{-1} for the past 2.5 Myr, whereas exhumation rates outside the core are an order of magnitude lower[17]; hence the 2 mm yr^{-1} contour provides an independent threshold for delineating the high and low exhumation zones and for comparing spatial patterns in landslide erosion, stream power and topographic data. Exhumation rates were calculated using assumptions similar to those in ref. 18, using closure temperature data from ref. 29 and geothermal gradient information from ref. 30. The zone of rapid exhumation is based on the maximum aerial extent of the ~2 mm yr^{-1} contour for the different thermochronometers. Mineral cooling ages from samples ≤5 km from either side of rivers were projected onto the long profiles in Fig. 3.3. Landslide erosion data in Fig. 3.4 are based on summing landslide volumes within a 10-km-diameter circle centred on each thermochronology sample after clipping the circle to the mappable area. Data were excluded if the clipped area was <10% of the original, unclipped area. Exhumation rates in Fig. 3.4a–d are based on a 75 °C km^{-1} geothermal gradient, the midpoint of the 50–100 °C km^{-1} range[18,30].

Statistical analyses. Hillslope angle modes were determined from 1° slope bins. We tested for significant differences ($p \leq 0.05$) in mineral cooling ages, stream power and landslide erosion inside versus outside the zone of high exhumation using Mann-Whitney U tests, as these data were not normally distributed. Hillslope angle data were normally distributed and differences were assessed using a t-test. Differences in landslide erosion as a function of hillslope angle were assessed by binning erosion data in 5° increments. A natural log transformation was applied to the landslide erosion data so they approximated a normal distribution and an analysis of variance with a post hoc Fisher's least significant difference test was used to test for differences in erosion rate across the slope groups. Data from grid cells with drainage areas <1 km^2 were not used in statistical analysis of erosion or hillslope angle data. Owing to the coarse resolution of the ASTER and Landsat images, 100 of the 223 grid cells in the 1974-2007 inventory had no mapped landslides; we considered these grid cells to have ‘no data’ and excluded them from the statistical analysis of the 1974–2007 landslide data. Reduced major axis regression was used to assess the relationship between erosion rates and exhumation rates and erosion rates and stream power. The pre-1974 landslide erosion data were used for regression analyses because the spatial pattern was not influenced by the Zhamu Creek outburst flood.

References

1. Burbank, D. W. et al. Bedrock incision, rock uplift and threshold hillslopes in the northwestern Himalayas. *Nature* 379, 505-510 (1996).
2. Montgomery, D. R. Slope distributions, threshold hillslopes, and steady-state topography. *Am. J. Sci.* 301, 432-454 (2001).
3. Montgomery, D. R. & Brandon, M. T. Topographic controls on erosion rates in tectonically active mountain ranges. *Earth Planet. Sc. Lett.* 201, 481-489 (2002).
4. Roering, J. J., Kirchner, J. W. & Dietrich, W. E. Evidence for nonlinear, diffusive sediment transport on hillslopes and implications for landscape morphology. *Water Resour. Res.* 35, 853-870 (1999).
5. Binnie, S. A., Phillips, W. M., Summerfield, M. A. & Fifield, L. K. Tectonic uplift, threshold hillslopes, and denudation rates in a developing mountain range. *Geology* 35, 743-746 (2007).
6. Ouimet, W. B., Whipple, K. X. & Granger, D. E. Beyond threshold hillslopes: Channel adjustment to base-level fall in tectonically active mountain ranges. *Geology* 37, 579-582 (2009).
7. DiBiase, R. A., Whipple, K. X., Heimsath, A. M. & Ouimet, W. B. Landscape form and millennial erosion rates in the San Gabriel Mountains, CA. *Earth. Planet. Sci. Lett.* 289, 134-144 (2009).
8. Strahler, A. N. Equilibrium theory of erosional slopes approached by frequency distribution analysis; Part 1. *Am. J. Sci.* 248, 673-696 (1950).
9. Korup, O. Rock type leaves topographic signature in landslide-dominated mountain ranges. *Geophys. Res. Lett.* 35, L11402 (2008).
10. Clarke, B. A. & Burbank, D. W. Bedrock fracturing, threshold hillslopes, and limits to the magnitude of bedrock landslides. *Earth. Planet. Sci. Lett.* 297, 577-586 (2010).
11. Safran, E. B. et al. Erosion rates driven by channel network incision in the Bolivian Andes. *Earth Surf. Process. Landf.* 30, 1007-1024 (2005).
12. Schmidt, K. M. & Montgomery, D. R. Limits to relief. *Science* 270, 617-620 (1995).
13. Hovius, N., Stark, C. P. & Allen, P. A. Sediment flux from a mountain belt derived by landslide mapping. *Geology* 25, 231-234 (1997).
14. Brookfield, M. E. The evolution of the great river systems of southern Asia during the Cenozoic India-Asia collision: Rivers draining southwards. *Geomorphology* 22, 285-312 (1998).
15. Finlayson, D. P., Montgomery, D. R. & Hallet, B. Spatial coincidence of erosional and metamorphic hot spots in the Himalaya. *Geology* 30, 219-222 (2002).
16. Finnegan, N. J. et al. Coupling of rock uplift and river incision in the Namche Barwa-Gyala Peri massif, Tibet. *Geol. Soc. Am. Bull.* 120, 142-155 (2008).
17. Seward, D. & Burg, J. P. Growth of the Namche Barwa syntaxis and associated evolution of the Tsangpo Gorge: Constraints from structural and thermochronological data. *Tectonophysics* 451, 282-289 (2008).
18. Stewart, R. J. et al. Brahmaputra sediment flux dominated by highly localized rapid erosion from the easternmost Himalaya. *Geology* 36, 711-714 (2008).
19. Zeitler, P. K. et al. Erosion, Himalayan geodynamics, and the geomorphology of metamorphism. *GSA Today* 11, 4-9 (2001).
20. Malamud, B. D., Turcotte, D. L., Guzzetti, F. & Reichenbach, P. Landslide inventories

and their statistical properties. *Earth Surf. Process. Landf.* 29, 687-711 (2004).

21. Shang, Y. et al. A super-large landslide in Tibet in 2000: Background, occurrence, disaster, and origin. *Geomorphology* 54, 225-243 (2003).
22. Enkelmann, E., Ehlers, T. A., Zeitler, P. K. & Hallet, B. Denudation of the Namche Barwa antiform, eastern Himalaya. *Earth. Planet. Sci. Lett.* 307, 323-333 (2011).
23. Larsen, I. J., Montgomery, D. M. & Korup, O. Landslide erosion controlled by hillslope material. *Nature Geosci.* 3, 247-251 (2010).
24. Heimsath, A. M., DiBiase, R. A. & Whipple, K. X. Soil production limits and the transition to bedrock-dominated landscapes. *Nature Geosci.* 5, 210-214.
25. Montgomery, D. R. et al. Evidence for Holocene megafloods down the Tsangpo River gorge, southeastern Tibet. *Quaternary Res.* 62, 201-207 (2004).
26. Korup, O. & Montgomery, D. R. Tibetan plateau river incision inhibited by glacial stabilization of the Tsangpo gorge. *Nature* 455, 786-789 (2008).
27. Finnegan, N. J., Roe, G., Montgomery, D. R. & Hallet, B. Controls on the channel width of rivers: Implications for modeling fluvial incision of bedrock. *Geology* 33, 229-232 (2005).
28. Anders, A. M. et al. Spatial patterns of precipitation and topography in the Himalaya. *GSA Spec. Pap.* 398, 39-54 (2006).
29. Reiners, P. W. & Brandon, M. T. Using thermochronology to understand orogenic erosion. *Annu. Rev. Earth Planet. Sci.* 34, 419-466 (2006).
30. Craw, D., Koons, P. O., Zeitler, P. K. & Kidd, W. S. F. Fluid evolution and thermal structure in the rapidly exhuming gneiss complex of Namche Barwa-Gyala Peri, eastern Himalayan syntaxis. *J. Metamorph. Geol.* 23, 829-845 (2005).

CHAPTER 4

Rapid mountain weathering breaks global speed limit

Whether Earth's tectonically-active mountains significantly influence global CO_2 cycling and climate depends on the relationship between erosion and chemical weathering rates. Despite the important role soils play in hillslope weathering, to date there have been no measurements of soil production and weathering rates in Earth's most rapidly uplifting mountains. ^{10}Be concentrations in soils from the western Southern Alps of New Zealand demonstrate that soil is produced from bedrock much more rapidly than previously recognized, at rates up to 2.5 mm yr^{-1}. Soil chemical denudation rates increase linearly with erosion rates and are the highest rates yet measured. The high weathering rates support the view that the majority of global chemical denudation occurs on the small, mountainous fraction of Earth's surface, and thus that tectonics and erosion are major influences on global climate.

The exchange of CO_2 between Earth's rock and surficial reservoirs—the atmosphere, biosphere, soils, and oceans—controls global climate on geological timescales[1]. Vigorous, ongoing debate centers on the role of plate tectonics in influencing global climate via links among rock uplift, relief generation, erosion, silicate weathering, and CO_2 consumption[2–4]. Soil production and weathering rates have not previously been measured in Earth's most rapidly uplifting mountains, where high rates of orographic precipitation, pervasively fractured bedrock, and dense vegetation provide potentially optimal conditions for rapid soil production and chemical weathering[5]. However, the now conventional views hold that there are 'speed limits' to both soil production and soil chemical denudation rates, that mountains are inefficient sites for weathering because they lack extensive soil cover[6], and that the critical zone response to tectonic uplift has previously been greatly exaggerated[7]. The existence of a weathering speed limit and the implied de-coupling of erosion and weathering are major untested assumptions underpinning analyses of the role mountains play in influencing global climate.

Soils are generally thought to play a minor role in the erosion[8] and weathering of tectonically-active mountains, as models predict that the contribution of soils to weathering fluxes declines with increasing erosion rates[9]. Soil production[10] is conventionally thought to occur too slowly to keep pace with the more rapid rates of rock uplift and erosion that characterize tectonically-active mountains, leading to progressive stripping of soil and the emergence of bedrock hillslopes as erosion rates increase[7,11]. Whether hillslopes maintain a soil mantle or are stripped to bedrock at high erosion rates is central to understanding the role mountains play in CO_2 cycling, because chemical denudation rates are predicted to depend strongly on soil thickness[9,12,13,14].

The relationship between weathering (chemical denudation) and erosion (physical denudation) or soil production (physical + chemical = total denudation) is thought to depend on whether chemical denudation rates are supply- or kinetically-limited. Supply-limited weathering is thought to occur at low denudation rates where long mineral residence times within soil lead to complete weathering of reactive material, such that chemical denudation rates are limited only by the rate at which fresh minerals are exposed by erosion[15]. In contrast, kinetically-limited chemical denudation is thought to occur where short mineral residence times lead to incomplete weathering. Based on the assumption that soil thickness approaches zero as erosion rates increase, models predict that kinetically-limited weathering occurs at high denudation rates, resulting in a de-coupling of weathering and erosion. Under these circumstances the relationship between chemical and physical denudation becomes increasingly non-linear, such that very little weathering is predicted to occur at the highest physical denudation rates[12–14]. These model predictions have led to the conclusion that increased rates of tectonic uplift and physical erosion do not lead to faster weathering[6,12,13,16].

The argument for the existence of weathering speed limits is based, in great part, on recent work in the San Gabriel Mountains, where hillslope bedrock exposure increases with increasing denudation rates[17], soil production rates of 0.01–0.6 mm yr^{-1} are the highest previously measured[7], and the relationship between soil chemical and physical denudation rates is consistent with kinetically-limited weathering[16]. In contrast to the San Gabriel Mountains, which receive ≤1 m yr^{-1} of precipitation and erode at rates ≤1 mm yr^{-1} (ref. 17), the most-tectonically-active mountains on Earth—including the Himalaya, Taiwan, and New Zealand Southern Alps orogens—have higher rates of both precipitation (1–10 m yr^{-1}) and erosion (1–10 mm yr^{-1}), and hence the potential for much higher soil production and weathering rates than have been measured previously. The observation that subalpine portions of these mountains tend to be soil-mantled calls into question the views that hillslopes are necessarily stripped to bedrock at high uplift rates[11] due to a global weathering speed limit[6].

We measured soil production, soil weathering, and catchment-scale denudation rates[18] in the central portion of the western Southern Alps of New Zealand (Fig. 4.1), where rock uplift and long-term exhumation rates are ~10 mm yr^{-1} ref. [19,20] along the Alpine Fault, which accommodates oblique collision between the Pacific and Australian plates[20]. The rapid uplift is

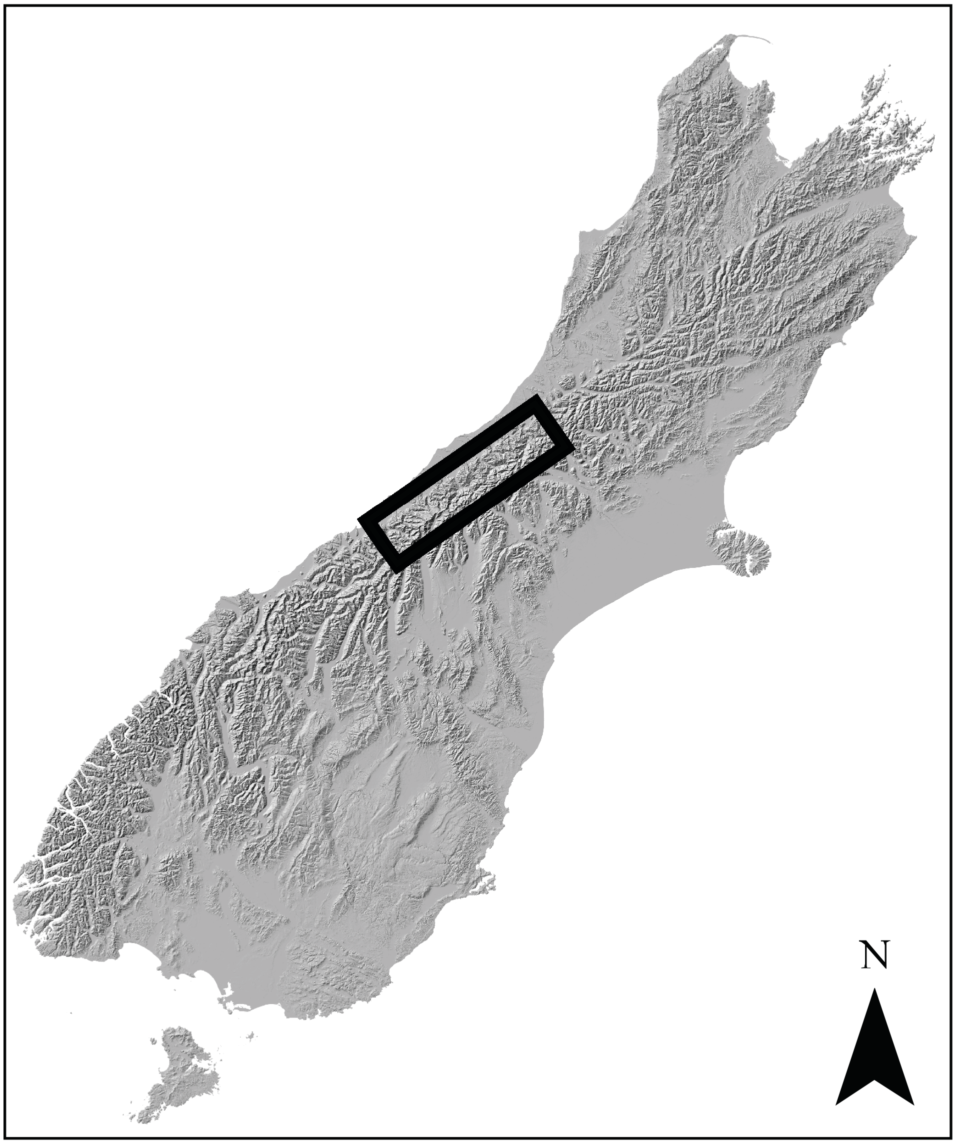

Figure 4.1. Location of the field site on New Zealand's South Island.

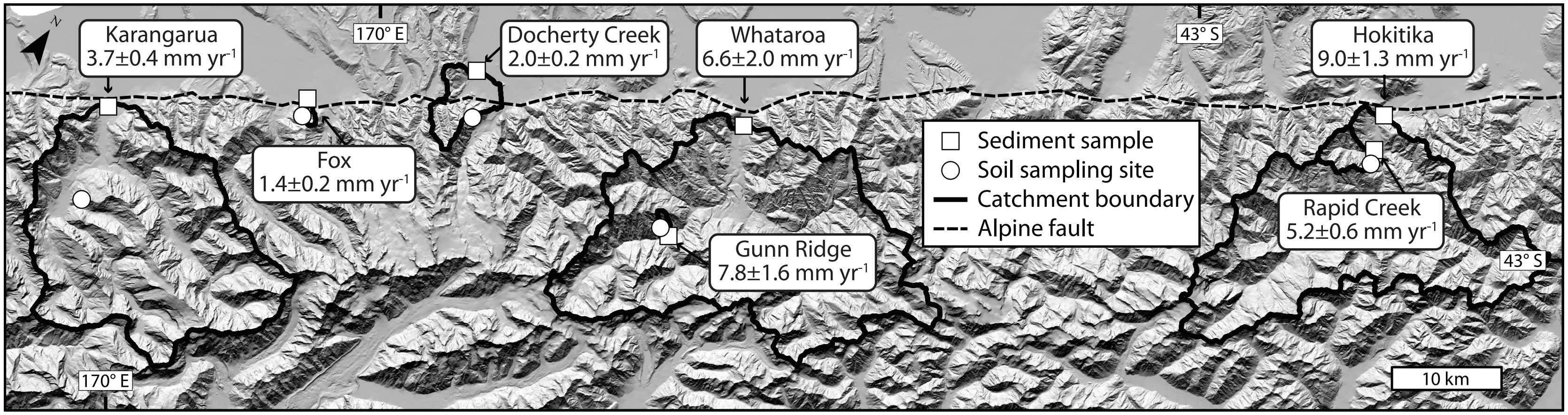

Figure 4.2. Sample locations and watershed scale denudation rates in the western Southern Alps.

balanced by high rates of erosion[21,22] such that the fluxes of material into and out of the orogen are thought to be in steady-state[23]. Mean annual precipitation on the western flank of the mountains exceeds 10 m yr^{-1}, supporting dense temperate montane rainforest and sub-alpine shrub ecosystems that grow on <1 m thick soils formed from highly-fractured schist bedrock[24–26].

Soil production rates on ridgetops range from 0.1–2.5 mm yr^{-1} and decline exponentially with increasing soil thickness at two of the three sites with a sufficient number of samples ($n \geq 5$) to define a regression relationship (Fig. 4.3a). The exponentially declining "soil production functions" observed in the western Southern Alps are consistent with those determined for other landscapes[10]. However, comparison of soil production rates against a compilation of data from sites worldwide indicates that soil production rates in the western Southern Alps reach more than an order of magnitude greater than rates measured elsewhere (Fig. 4.3b), showing that soil production can play a far greater role in mountain denudation than previously recognized[8,11].

Chemical depletion fractions appear to decline with increasing soil production rates, which is consistent with the kinetically-limited weathering that models predict at high denudation rates (Fig. 4.2c). However, the high p-values preclude concluding that the regression slopes are significantly different from zero. Thus, contrary to model predictions, weathering may be supply-limited at the very high denudation rates we observe. Regardless of whether the chemical denudation data conform strictly to supply- or kinetically-limited weathering end members or reflect both weathering regimes, the chemical denudation rates increase linearly with physical erosion rates (Fig. 4.3d). Comparison of soil chemical denudation rates from the western Southern Alps against a compilation of worldwide data indicates soil chemical

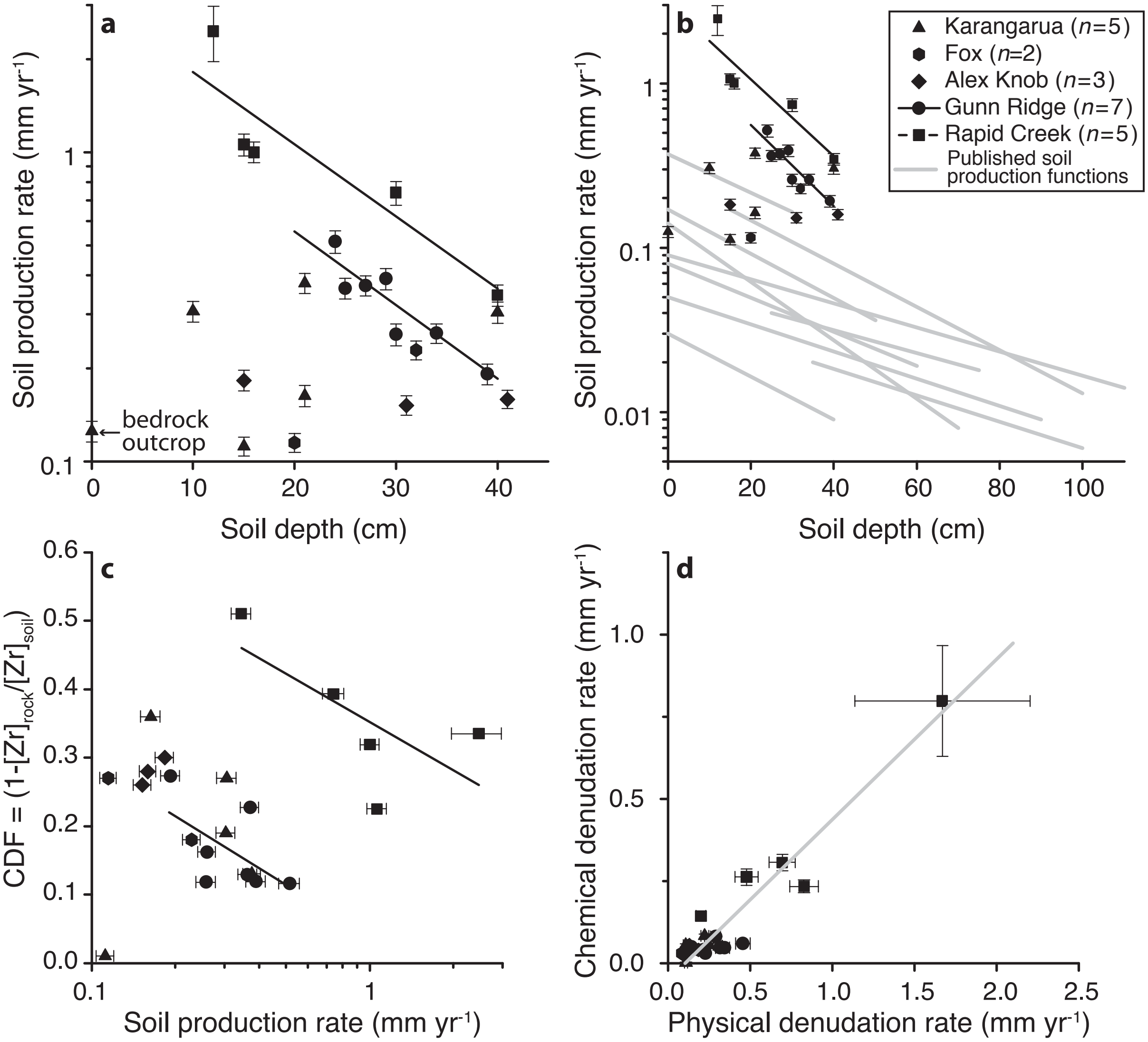

Figure 4.3. Soil production rates, chemical depletion fraction (CDF) data, and chemical versus physical denudation rates. a, Soil production rate versus soil depth for the western Southern Alps. Error bars indicate propagated soil production rate uncertainties. Soil production rates decline exponentially with increasing soil depth at the Gunn Ridge and Rapid Creek sites and the respective exponential regression fits are $y = 1.73(+0.71/-0.51)e^{-0.057(\pm 0.011)x}$, $R^2=0.83$, p=0.004, and $y = 3.12(+1.34/-0.94)e^{-0.054(\pm 0.014)x}$, $R^2=0.82$, p=0.03. b, western Southern Alps soil production rate data and soil production functions plotted with a global compilation of soil production functions; see Appendix 3 for data sources. c, CDF versus soil production rates for the western Southern Alps. CDF values decline as soil production rates increase, as $y = -0.11(\pm 0.069)\ln(x)+0.037(\pm 0.08)$, p=0.17, $R^2=0.34$ for Gunn Ridge and $y = -0.10(\pm 0.063)\ln(x)+0.35(\pm 0.040)$, p=0.21, $R^2=0.46$ for Rapid Creek. d, Chemical denudation rate versus physical denudation rate for the western Southern Alps. Chemical denudation rates increase linearly as physical denudation rates increase. The linear reduced major axis (RMA) regression fit shown by the gray line is $y = 0.49(\pm 0.035)x-0.052(\pm 0.017)$, $p<0.001$, $R^2=0.90$. Values in parentheses are standard errors of parameter estimates. The legend applies to all panels (a–d).

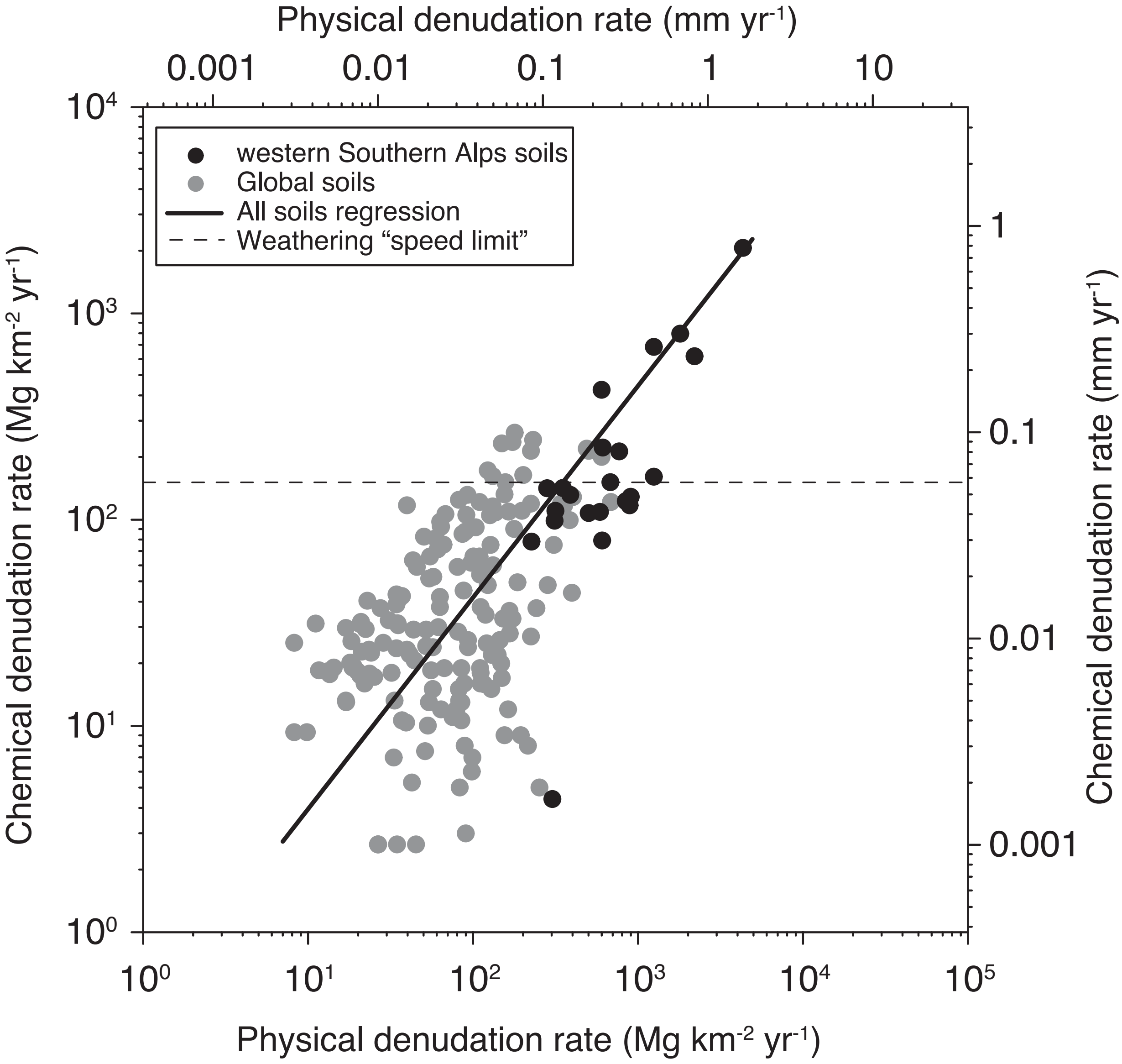

Figure 4.4. Compilation of global soil chemical versus physical denudation rate data. The RMA power-law fit to the soil mass flux data $y=0.37(+0.18/-0.11)]x^{1.025(\pm 0.059)}$, $R^2=0.38$, $p<0.001$, indicating chemical denudation increases linearly as physical denudation rates increase by nearly three orders of magnitude. The weathering “speed limit”[6] (horizontal dashed line) is shown for reference. The upper and right axes with length units are related to the mass flux axes by a density of 2.65 g cm^{-3} and thus are approximate and for reference only, as rock density varies among the samples. See Appendix 3 for data sources.

denudation rates in the western Southern Alps are the highest values yet measured on Earth, and that chemical denudation rates increase linearly as erosion rates increase by nearly three orders of magnitude (Fig. 4.4). Contrary to predictions of previous workers[6,9,12,13,16], these results indicate that soil chemical denudation rates can be extremely high in rapidly uplifting mountains, demonstrating that high erosion rates can be accompanied by high chemical denudation rates.

Watershed-scale denudation rates in the western Southern Alps range from 1–9 mm yr^{-1} (Fig. 4.2). Small catchments that drain areas within 1–2 km of the Alpine Fault have the lowest denudation rates of 1–2 mm yr^{-1}. Larger catchments and small sub-catchments that drain areas farther to the east of the Alpine Fault denude at rates of 4–9 mm yr^{-1}. The spatial pattern of decreasing watershed-scale erosion toward the Alpine Fault is consistent with crustal velocity fields predicted by simple shear deformation[27] and vertical deformation measured by GPS[28].

The maximum soil production rate we measured in the western Southern Alps equals or exceeds denudation rates for the more slowly eroding watersheds. However, for a given catchment, soil production rates are a fraction of the catchment-averaged denudation rates. This finding differs from more slowly eroding landscapes where maximum soil production rates generally equal catchment-averaged values[7]. Hillslopes at sub-alpine elevations in the western Southern Alps have extensive soil mantles with very little bedrock exposure, even though soil production rates are lower than catchment-averaged erosion rates. The landscape maintains a soil mantle because the return interval for landslides, which must account for the balance of catchment-averaged denudation that is not attributed to soil production[21], is long enough at any point on the landscape that soils develop between failures[7].

We suggest the rapid soil production and weathering rates in the western Southern Alps arise from the interaction of climatic, biologic, and geologic influences. The high mean annual precipitation promotes rapid leaching[24] and supports high rates of vegetation productivity[29]. The biotic driver of rapid soil production is vegetation, as burrowing mammals, which contribute to soil production in other landscapes[10], are not endemic to New Zealand. Coarse and fine roots readily penetrate bedrock by exploiting foliation planes and fractures generated by tectonics[26] and erosional unloading (Fig. A3.1). Root expansion in fractures, especially those within a few cm of the soil-bedrock interface, likely plays a key role in converting rock to soil, both by physically breaking rock and by enhancing chemical weathering via organic acid production and increased subsurface CO_2 concentrations[1]. The steep soil production functions we observe also bear a signature of biotic-abiotic coupling. The decline of soil production rates with soil depth (the slope of the soil production function) in the western Southern Alps is approximately twice that which is generally observed in other settings. Since the depth of rooting is directly related to water availability[30], roots will be concentrated at shallow depths in wet landscapes. Due to the high mean annual precipitation and lack of distinct rainfall seasonality in the western Southern Alps (Fig. A3.2), water is continuously available to plants within soil and near-surface bedrock fractures. Root biomass, and hence rock damage and weathering caused by roots, is concentrated at shallow depths. In contrast, drier regions with seasonal water deficits, such as in the western U.S. and Australia (where most soil production functions have previously been defined), will be characterized by deeper root depths, and hence a more dispersed depth distribution of rock damage, resulting in lower soil production function slopes.

The extremely rapid soil production rates in the western Southern Alps are consistent with estimated soil residence times of only a few centuries for the Cropp River watershed[24], which shares a drainage divide with the Rapid Creek catchment, and rapid leaching documented at other sites on the South Island's west coast[31]. Soil production rates have not been measured in other mountains undergoing comparable uplift rates. However, the rapid soil production in the western Southern Alps is consistent with other landscapes that maintain soil mantled hillslopes despite high rates of rock uplift and erosion, such as the Taiwan orogen, where shallow landslides mobilizing primarily soil erode at rates >2 mm yr^{-1} (ref. 32) and the Tsangpo Gorge in the eastern Himalaya, where landslides mobilizing soil and regolith contribute to erosion rates in excess of 4 mm yr^{-1} (ref. 33).

The linear relationship between soil chemical denudation and physical denudation rates observed in the western Southern Alps is consistent with data from more slowly eroding landscapes[15] and extends the range of soil production rates over which weathering and denudation rates increase in proportion to one another to much higher values than previously recognized. If the relationship becomes non-linear or reverses to an inverse correlation, as predicted by several models[12–14], it does so at rates higher than we observe in the western Southern Alps.

Global river solute and sediment yield data[34] demonstrate that short-term, catchment-averaged chemical denudation rates also exceed the proposed chemical weathering “speed limit”[6], though the power law scaling exponent is less than unity, which differs from the soils data (Fig. 4.5). River solute data indicate chemical denudation rates in the western Southern Alps are extremely high, and are of the same magnitude as rates determined for soils, yet chemical weathering accounts for only 1–5% of catchment-scale denudation[22,36]. The mean soil chemical denudation rates we measured are 1–7% of the ^{10}Be-based total denudation rates determined for each watershed, whereas mean chemical denudation is 16–32% of the soil production rate at each of the ridgetop sites. Given that the soil weathering contribution to catchment denudation is of the same order as denudation determined from river solute

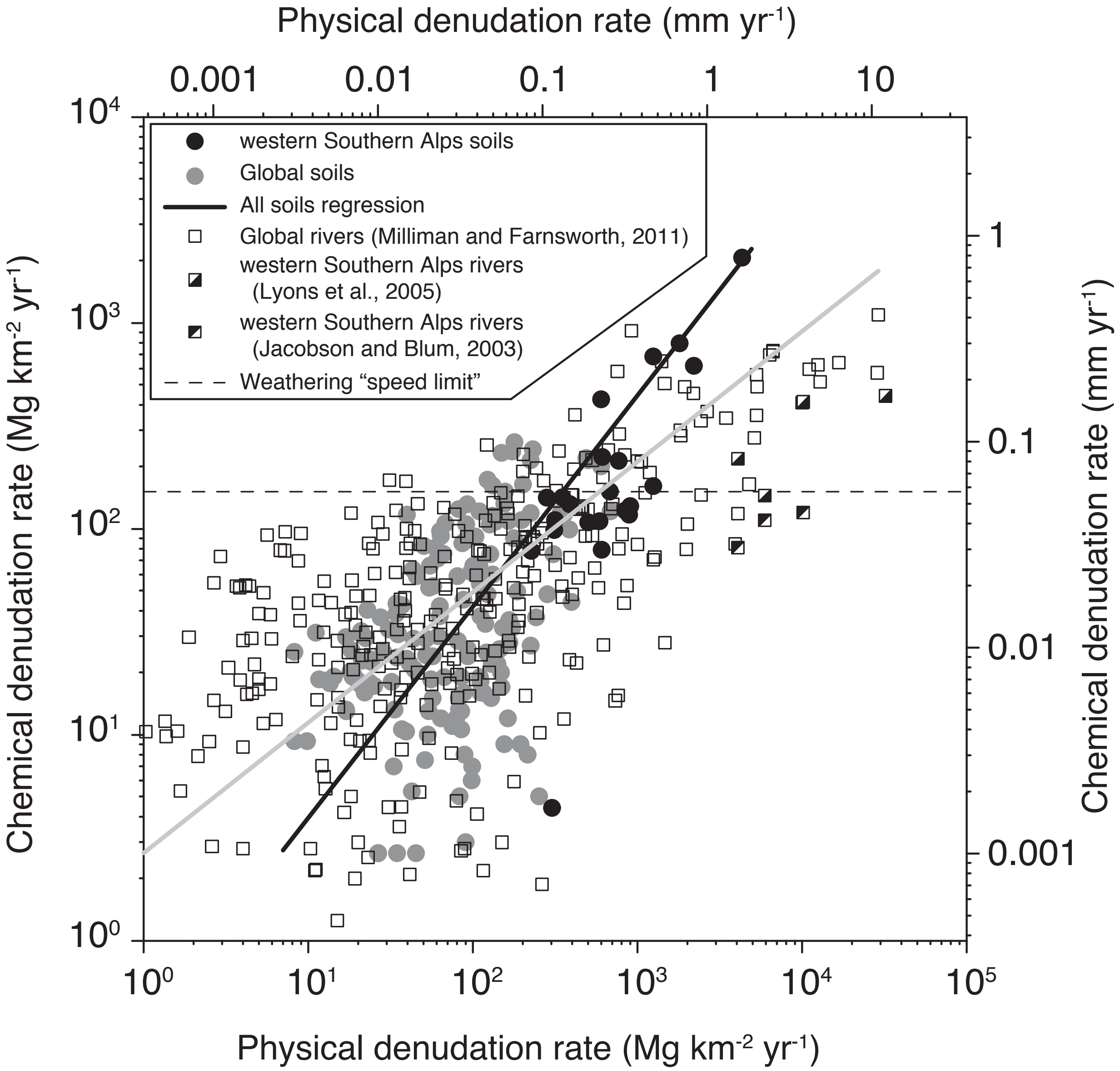

Figure 4.5. Compilation of global soil and river chemical versus physical denudation rate data. The RMA power law fit to the river data[34] is $y=2.66(+3.05/-2.31)]x^{0.63(\pm 0.028)}$, $R^2=0.41$, $p<0.001$, $p<0.001$, $R^2=0.41$. The power-law scaling exponent for the river flux data indicates watershed scale chemical denudation rates increase more slowly than those for soils, given the same increase in physical denudation rate. Also shown are river flux-based denudation data from the western Southern Alps[22,35,36]; note that river and soil chemical denudation rates in the western Southern Alps are of similar magnitude. Also note also that soil and river chemical denudation rates both break the proposed "speed limit"[6]

measurements, these results indicate that the very high catchment-scale chemical denudation rates observed in the western Southern Alps can be explained by soil chemical denudation rates alone, without a need to invoke factors such as deep bedrock weathering or weathering in floodplains[9,37]. The differing ratio of chemical to total denudation rates observed for soils versus catchments is thus due to increased delivery of unweathered rock to rivers by landslides. Hence, to simulate weathering fluxes from mountains, models need to incorporate spatially and temporally non-uniform erosion and weathering[38].

We modeled global denudation rates as a function of slope[39] using a 3 arc-second DEM and estimate that 52% of Earth's denudation occurs where mean local hillslope angles exceed 15°, which accounts for only 8.8% of the terrestrial surface area (Fig. 4.6). Areas with slopes greater than 20° and 30° contribute 41% and 16% of Earth's total annual denudation, though these areas make up only 4.6% and 0.6% of Earth's surface, respectively (Fig. 4.7). These results demonstrate that the small mountainous fraction of Earth's surface contributes disproportionally to global denudation. These findings counter those of Willenbring et al.[39], who claimed that the majority of Earth's denudation occurs on the extensive terrestrial area with low slopes. However, Willenbring et al. inappropriately used a denudation-slope relationship calibrated with 3 arc-second slope data to model global erosion using slopes derived from a 30 arc-second DEM, thereby ignoring the slope angle dependence on DEM grid scale[40]. The inappropriate DEM grid scale caused substantial underestimation of denudation rates in steep mountain terrain, as our analysis indicates that when using 30 arc-second DEM data only 0.81% of Earth's surface has mean local hillslope angles >15°, which contribute only 5.1% of the total global denudation.

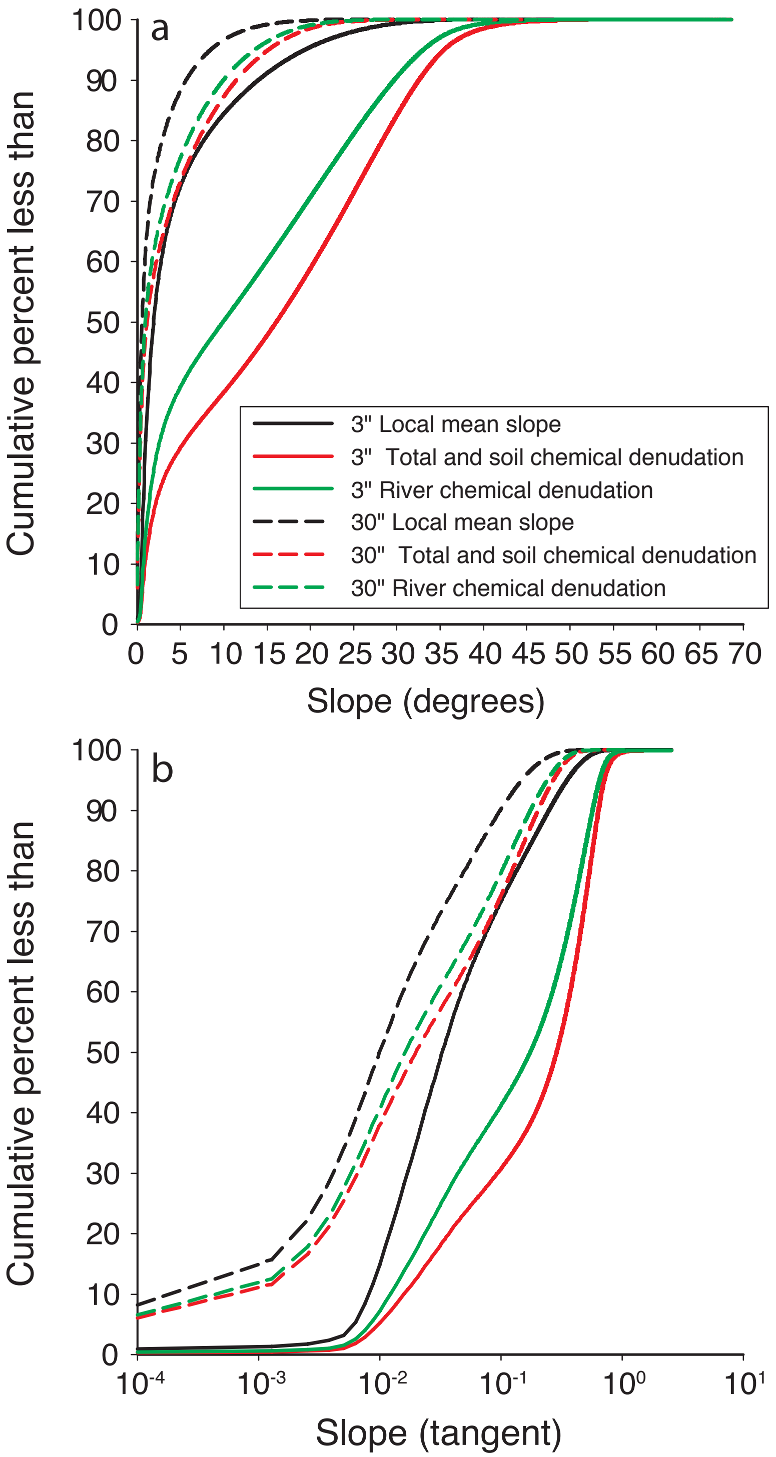

Figure 4.6. Global cumulative percent frequency of mean local slope angles and denudation rates as a function of slope expressed in degrees (a) and as the tangent (b). The black curves show the percentage of Earth's surface with slopes less than a given value; the red and green curves show the percentage of Earth's denudation contributed by areas with slopes less than a given value. Zero slopes are expressed as tangent = 10^{-4}.

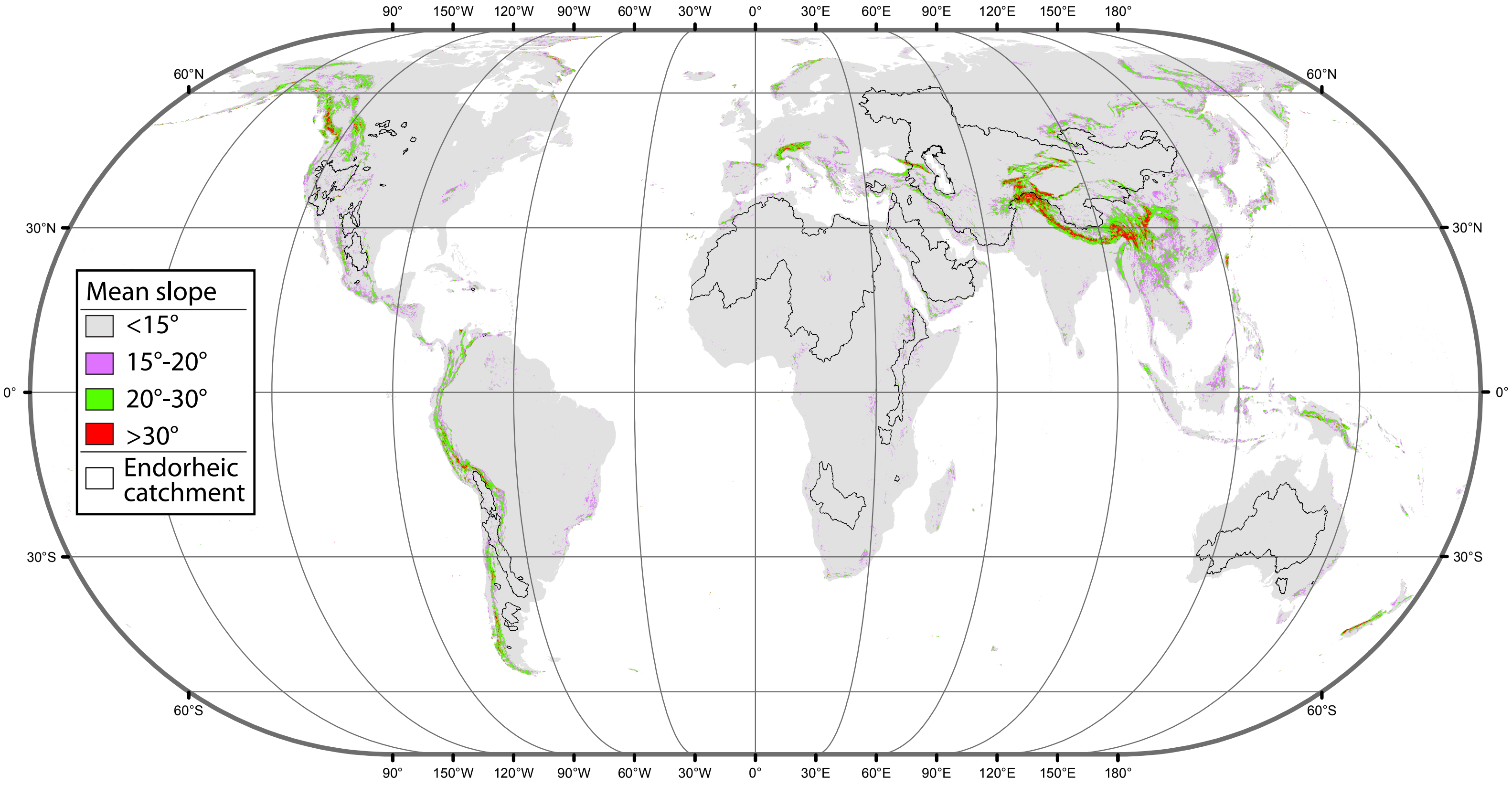

Figure 4.7. Global slope map. Slope angles exceed 15° on only a small fraction of Earth's terrestrial surface. Slope angles are mean values calculated using a 5 km by 5 km moving window. Endorheic catchments (closed basins) are outlined in black.

Modeling global chemical denudation rates as a function of total denudation rate indicates that the 8.8% of Earth's surface with slopes >15° is responsible for 40–52% of global chemical denudation. Similarly, areas with slopes greater than 20° and 30° contribute 29–41% and 9–16% of global chemical denudation. These results demonstrate that mountains are a major influence on global scale weathering fluxes and are consistent with both modeled and measured Si fluxes from mountains to oceans[34,41] and support the view that the collision of India and Asia would have cooled global climate via increased erosion and weathering rates[2]. Hillslopes in the western Southern Alps are soil mantled, despite catchment-averaged denudation rates of up to 9 mm yr^{-1}. Hence mountain hillslopes do not necessarily lose their soil cover at high erosion rates. Our results suggest that mountain soils are a key source of solutes that are eventually delivered to oceans, as soil chemical denudation rates in the western Southern Alps are the most rapid yet measured on Earth and can account for the high watershed scale chemical denudation rates. The high soil chemical denudation rates indicate that whether hillslope weathering rates are necessarily supply- or kinetically-limited [12,13,14,16] has little bearing on the magnitude of chemical denudation rates in mountains and thus indicate that the majority of global chemical denudation occurs on the small mountainous fraction of Earth's surface. Hence, contrary to the notion that mountains do not influence global climate because they lack soil-mantled hillslopes and are hence inefficient sites for weathering[6], our results support the view that, if silicate weathering controls CO_2 cycling on geological timescales, then high erosion and weathering rates in mountains greatly influence climate[2]. We conclude that, due to soil weathering, mountains do indeed matter for global weathering, CO_2 cycling, and climate. If there are speed limits to soil production and soil chemical denudation in Earth's most rapidly eroding mountains, they are not yet posted.

References

1. Berner, R. A. GEOCARB III: A revised model of atmospheric CO_2 over Phanerozoic time. *American Journal of Science* **301**, 182-204 (2001).
2. Raymo, M. & Ruddiman, W. Tectonic forcing of late Cenozoic climate. *Nature* **359**, 117-122 (1992).
3. Molnar, P. & England, P. Late Cenozoic uplift of mountain ranges and global climate change: chicken or egg? *Nature* **346**, 29-34 (1990).
4. Willenbring, J. & von Blanckenburg, F. Long-term stability of global erosion rates and weathering during late-Cenozoic cooling. *Nature* **465**, 211-214 (2010).
5. Larsen, I., Montgomery, D. & Korup, O. Landslide erosion controlled by hillslope material. *Nature Geoscience* **3**, 247-251 (2010).
6. Dixon, J. & von Blanckenburg, F. Soils as pacemakers and limiters of global silicate weathering. *Comptes Rendus Geoscience* **344**, 597-609 (2012).
7. Heimsath, A., DiBiase, R. & Whipple, K. X. Soil production limits and the transition to bedrock-dominated landscapes. *Nature Geoscience* **5**, 210-214, (2012).
8. Burbank, D. *et al.* Bedrock incision, rock uplift and threshold hillslopes in the northwestern Himalayas. *Nature* **379**, 505-510 (1996).
9. West, A. J. Thickness of the chemical weathering zone and implications for erosional and climatic drivers of weathering and for carbon-cycle feedbacks. *Geology* **40**, 811-814 (2012).
10. Heimsath, A., Dietrich, W., Nishiizumi, K. & Finkel, R. The soil production function and landscape equilibrium. *Nature* **388**, 358-361 (1997).
11. Whipple, K., Kirby, E. & Brocklehurst, S. Geomorphic limits to climate-induced increases in topographic relief. *Nature* **401**, 39-43 (1999).
12. Gabet, E. & Mudd, S. A theoretical model coupling chemical weathering rates with denudation rates. *Geology* **37**, 151-154 (2009).
13. Ferrier, K. & Kirchner, J. Effects of physical erosion on chemical denudation rates: A numerical modeling study of soil-mantled hillslopes. *Earth. Planet. Sci. Lett.* **272**, 591-599 (2008).
14. Hilley, G., Chamberlain, C., Moon, S., Porder, S. & Willett, S. Competition between erosion and reaction kinetics in controlling silicate-weathering rates. *Earth. Planet. Sci. Lett.* **293**, 191-199 (2010).
15. Riebe, C. S., Kirchner, J. W. & Finkel, R. C. Erosional and climatic effects on long-term chemical weathering rates in granitic landscapes spanning diverse climate regimes. *Earth. Planet. Sci. Lett.* **224**, 547-562 (2004).
16. Dixon, J., Hartshorn, A., Heimsath, A., DiBiase, R. & Whipple, K. Chemical weathering response to tectonic forcing: A soils perspective from the San Gabriel Mountains, California. *Earth. Planet. Sci. Lett.* **323-324**, 40-49 (2012).
17. DiBiase, R., Heimsath, A. & Whipple, K. Hillslope response to tectonic forcing in threshold landscapes. *Earth Surface Processes and Landforms* **38**, 855-865 (2012).
18. see Methods in Appendix 3
19. Tippett, J. & Kamp, P. Fission track analysis of the late Cenozoic vertical kinematics of continental Pacific crust, South Island New Zealand. *Journal of Geophysical Research* **98**, 16,119–116,148 (1993).

20. Norris, R. J. & Cooper, A. F. Late Quaternary slip rates and slip partitioning on the Alpine Fault, New Zealand. *Journal of Structural Geology* **23**, 507-520 (2001).
21. Hovius, N., Stark, C. & Allen, P. Sediment flux from a mountain belt derived by landslide mapping. *Geology* **25**, 231-234 (1997).
22. Lyons, B., Carey, A., Hicks, D. & Nezat, C. Chemical weathering in high-sediment-yielding watersheds, New Zealand. *Journal of Geophysical Research* **110**, F11008 (2005).
23. Adams, J. Contemporary uplift and erosion of the Southern Alps, New Zealand: summary. *Geol. Soc. Am. Bull* **91**, 1-114 (1980).
24. Basher, L., Tonkin, P. & McSaveney, M. Geomorphic history of a rapidly uplifting area on a compressional plate boundary: Cropp River, New Zealand. *Zeitschrift für Geomorphologie* **69**, 117-131 (1988).
25. Griffiths, G. & McSaveney, M. Distribution of mean annual precipitation across some steepland regions of New Zealand. *New Zealand Journal of Science* **26**, 197-209 (1983).
26. Clarke, B. A. & Burbank, D. W. Quantifying bedrock-fracture patterns within the shallow subsurface: Implications for rock mass strength, bedrock landslides, and erodibility. *Journal of Geophysical Research* **116**, F04009, (2011).
27. Braun, J., Herman, F. & Batt, G. Kinematic strain localization. *Earth. Planet. Sci. Lett.* **300**, 197-204 (2010).
28. Beavan, J. *et al.* Distribution of present-day vertical deformation across the Southern Alps, New Zealand, from 10 years of GPS data. *Geophysical Research Letters* **37**, L16305 (2010).
29. Hilton, R., Meunier, P., Hovius, N., Bellingham, P. & Galy, A. Landslide impact on organic carbon cycling in a temperate montane forest. *Earth Surface Processes and Landforms* **36**, 1670-1679 (2011).
30. Graham, R. C., Rossi, A. M. & Hubbert, K. R. Rock to regolith conversion: Producing hospitable substrates for terrestrial ecosystems. *GSA Today* **20**, 4-9 (2010).
31. Eger, A., Almond, P. C. & Condron, L. M. Pedogenesis, soil mass balance, phosphorus dynamics and vegetation communities across a Holocene soil chronosequence in a super-humid climate, South Westland, New Zealand. *Geoderma* **163**, 185-196 (2011).
32. Tsai, Z.-X., You, G. J. Y., Lee, H.-Y. & Chiu, Y.-J. Modeling the sediment yield from landslides in the Shihmen Reservoir watershed, Taiwan. *Earth Surface Processes and Landforms*, in press, doi:10.1002/esp.3309 (2013).
33. Larsen, I. J. & Montgomery, D. R. Landslide erosion coupled to tectonics and river incision. *Nature Geoscience* **5**, 468-473 (2012).
34. Milliman, J. & Farnsworth, K. *River Discharge to the Coastal Ocean: A Global Synthesis*. (Cambridge University Press, 2011).
35. Hicks, D. M. *et al.* Suspended sediment yields from New Zealand rivers. *Journal of Hydrology (New Zealand)* **50**, 81 (2011).
36. Jacobson, A. D. & Blum, J. D. Relationship between mechanical erosion and atmospheric CO_2 consumption in the New Zealand Southern Alps. *Geology* **31**, 865-868 (2003).
37. Lupker, M. *et al.* Predominant floodplain over mountain weathering of Himalayan sediments (Ganga basin). *Geochim. Cosmochim. Acta* **84**, 410-432 (2012).
38. Gabet, E. A theoretical model coupling chemical weathering and physical erosion in landslide-dominated landscapes. *Earth. Planet. Sci. Lett.*, 259-265 (2007).

39. Willenbring, J., Codilean, A. & McElroy, B. Earth is (mostly) flat: Apportionment of the flux of continental sediment over millennial time scales. *Geology* **41**, 343-346 (2013).
40. Zhang, W. & Montgomery, D. R. Digital elevation model grid size, landscape representation. *Water Resour. Res.* **30**, 1019-1028 (1994).
41. Hilley, G. & Porder, S. A framework for predicting global silicate weathering and CO_2 drawdown rates over geologic time-scales. *Proceedings of the National Academy of Sciences* **105**, 16855-16859 (2008).

CHAPTER 5

Conclusion

Hillslopes respond to tectonic and climatic forcing via adjustment in erosion rates. Hence, quantifying rates of hillslope erosion in Earth's most rapidly uplifting mountain ranges, though challenging, is essential for both advancing our understanding of orogens as coupled geomorphic-geodynamic systems and for determining the role mountains play in global biogeochemical cycles. This dissertation includes an advance in our ability to quantify landslide erosion rates and contains new erosion data for the eastern Himalaya and the western Southern Alps that I use to address two broad problems involving links among tectonics, topography, erosion, and climate.

Landslides are a dominant erosion mechanism in steep landscapes, but rates of landslide erosion are difficult to quantify. The landslide geometry data presented in Chapter 2 reveal that hillslope material is a fundamental control on landslide volume-area scaling. Landslides that initiate in unconsolidated soil and regolith have different geometric scaling than bedrock landslides, and failure to account for the different scaling can lead to large errors in landscape-scale erosion estimates. Scientists are already using the volume-area scaling exponents presented in Chapter 2 to quantify landslide erosion at sites around the world.

The concept of threshold hillslopes is a dominant paradigm in tectonic geomorphology and landscape evolution, but one that has not been tested directly. According to the threshold hillslope model, landslide erosion rates should spatially track rock uplift and river incision rates, but increase non-linearly as hillslope gradients approach the friction angle. The landslide erosion rates described in Chapter 3, determined from mapping 15,257 landslides in the eastern Himalaya, reveal that landslide erosion is correlated with both exhumation rates and stream power, and increases non-linearly once hillslope angles exceed ~30°. These results match the predictions of the threshold hillslope model and hence provide the first empirical validation of the paradigm. The landslide mapping also revealed that 70% of the landslide erosion that occurred between 1974 and 2007 took place during a single outburst flood that emanated from a failed landslide dam, demonstrating that hillslopes in the Tsangpo Gorge are indeed close to the threshold for stability.

The fourth chapter of this dissertation continues the theme of hillslope erosion in rapidly uplifting landscapes, but shifts both the process and geographic focus to soil production rates in the western Southern Alps of New Zealand. Knowing the magnitude of soil production and weathering rates and the degree to which they are coupled is important for evaluating the broader question of whether mountain uplift influences global climate. According to the uplift-climate hypothesis, rock uplift increases topographic relief, which increases erosion rates and hence weathering rates; silicate weathering releases Ca and Mg ions that are delivered to oceans, where they form carbonates, which sequesters CO_2 from the ocean-atmosphere system, and cools global climate on geological timescales. The increase in chemical weathering rates with increasing physical erosion rates is central to the uplift-climate hypothesis. Recent modeling studies have suggested that soil weathering rates become decoupled from erosion rates, leading to weathering 'speed limits', and the conclusion that mountain erosion does not influence global climate. Using *in-situ* produced ^{10}Be and Zr mass balance, I demonstrate that soil production and weathering rates in the western Southern Alps are extremely rapid. Moreover, chemical and physical denudation rates are linearly coupled, as demonstrated both by data from the western

Southern Alps and a global compilation of soil erosion and weathering measurements. The soil production rates are a fraction of catchment-scale denudation rates, but soil chemical weathering rates alone can account for catchment solute fluxes in this landscape, suggesting that soils set the weathering flux of rapidly uplifting mountains. Unsurprisingly, soil production and catchment-scale erosion rates in the western Southern Alps are the most rapid yet measured using ^{10}Be and, to my knowledge, the soil weathering rates are the most rapid weathering rates on Earth. Clearly, if there are speed limits to soil production and weathering, they are not yet posted. To assess the role of mountains in global chemical weathering, I modeled global denudation rates as a function of mean local slope and used relationships between denudation and weathering rates to model global weathering rates. The results show that mountains, though small in terms of the global land area, dominate the global chemical weathering flux. Hence, due to strong coupling among tectonics, topography, erosion, and weathering, mountains indeed influence global climate.

APPENDIX 1

Supplementary Data and Methods

Landslide geometry data. The source of the landslide geometry data and previously published *V-A* scaling parameters were from references 1–144.

Sensitivity analysis. We created synthetic power-law distributed landslide inventories (n = 10,000 each) over a pre-defined range of non-cumulative area-frequency scaling exponents (β = 1.5, 2.0, and 2.5) and landslide areas (10^3 m^2 $< A_l <$ 10^6 m^2), thus encompassing most published inventories. Volumetric errors induced by the moderate covariance between empirical volume-area α- and γ-values are <5% for this landslide area range. To further put the error introduced by differences in γ into context, we generated 30 inventories of 10,000 landslide areas randomly distributed about the area-frequency exponent β = 2.5, and computed the scatter in volumetric prediction for several values of γ. Comparing under- and overestimates derived from four empirical landslide inventories[69,145,146] demonstrates that our volumetric error prediction provides maximum bounds, mainly because only parts of these inventories follow a power-law trend.

Soil depth data. The global soil depth data and landslide and soil depth data for Redwood Creek, California, San Gabriel Mountains, California, and Oregon Coast Range area from references 69, 109, 111, 147, and 148.

Supplementary Table

Table A1.1. Landslide datasets, data sources, and parameters (± 1 standard error) for the relationship $V=\alpha\cdot A^{\gamma}$, goodness of fit (R^2), and sample size (n). Note that α has units [$L^{(3-2\gamma)}$], where L is in meters.

Data set	Data source	γ	log α	R^2	n
Global landslides					
All landslides	1-43, 45-58, 60-121, 123-144	1.332±0.005	-0.836±0.015	0.95	4231
Soil landslides	10, 13-16, 26, 37, 38, 41-43, 45, 63, 66, 69, 71, 79, 80, 84, 88, 94, 101, 109-111, 118, 134, 137, 138, 142	1.145±0.008	-0.44±0.02	0.90	2136
Soil scar geometry	10, 13-15, 26, 38, 69, 71, 79, 80, 84, 88, 94, 101, 109, 110, 111, 118, 137, 138, 142	1.262±0.009	-0.649±0.021	0.92	1617
Soil deposit geometry	63, 142	1.26±0.06	-0.70±0.11	0.76	124
Bedrock landslides	1-12, 17-37, 39-42, 45-58, 60, 64-78, 81-83, 85-87, 89-93, 95-100, 102-106, 112-115, 117, 119-121, 123-133, 135-142	1.35±0.01	-0.73±0.06	0.96	604
Bedrock scar geometry	2, 8, 10, 17, 20, 26, 27, 29, 30, 32, 47, 50, 71, 72, 75, 76, 82, 86, 92, 96, 97, 111, 112, 117, 126, 130, 133, 141, 142	1.41±0.02	-0.63±0.06	0.97	168
Bedrock deposit geometry	1-7, 9, 19, 21, 23-25, 28, 31, 33-36, 39, 40, 46, 48, 51, 52, 54-57, 58, 64, 67, 68, 70, 72-75, 77, 78, 85, 86, 89-91, 93, 98-100, 102-106, 113-115, 119-121, 123, 125, 127-129, 131, 135, 136, 140, 142, 144	1.40±0.02	-1.02±0.14	0.91	344
Soil landslides					
British Columbia	43	1.09	-0.81	0.95	124
southern California	109	1.11	-0.631	-	29
New Zealand	14, 41, 45, 94	1.13±0.03	-0.37±0.06	0.86	237
southern California	38, 109, 110	1.18±0.02	-0.68±0.05	0.95	117
Japan	62	1.19	-0.72	0.86	11
northern California	69, 101, 108	1.19±0.01	-0.49±0.02	0.95	956
Uganda	71	1.22±0.04	-0.40±0.12	0.91	93
Himalaya	10, 16, 80	1.25±0.03	-0.44±0.07	0.92	141
Japan	61	1.31	-0.41	0.84	51
Australia	37	1.34±0.03	-1.14±0.10	0.81	426
Scotland	63	1.39	-1.48	-	30
Oregon and Washington	84, 88, 107, 111	1.40±0.02	-0.98±0.04	0.86	684
Mixed Soil and bedrock inventories					
New Zealand	4, 12, 14, 20, 41, 45, 46, 72-77, 86, 89, 94, 99, 117, 123, 128, 136, 140	1.36±0.01	-0.86±0.05	0.97	389
Japan	142	1.36±0.03	-0.60±0.06	0.88	236
Himalaya	10, 11, 16, 28, 30, 31, 54-58, 80, 90, 115, 135	1.36±0.01	-0.59±0.03	0.98	428
New Guinea	116	1.368	-0.82	0.98	201
Global “slides”	44	1.450	-1.131	0.97	677
Bedrock landslides					
Himalaya	10, 11, 28, 30, 31, 54-58, 90, 115, 135	1.34±0.02	-0.49±0.08	0.98	123
Andes	5, 25, 36, 50, 52, 53, 102	1.38±0.16	-0.78±1.00	0.58	33
New Zealand	4, 12, 20, 41, 45, 46, 72-77, 86, 89, 99, 117, 123, 128, 136, 140	1.49±0.03	-1.60±0.19	0.93	140
Tien Shan	75	1.49±0.19	-1.43±1.27	-	20

Chile	5	1.56±0.17	-1.68±-1.21	0.82	14
Alps and Apennines	2, 6, 9, 18, 19, 24, 32, 33, 34, 36, 39, 40, 64, 70, 75, 78, 91, 98, 103-106, 113, 114, 125, 127, 129-131	1.60±0.07	-2.36±0.45	0.82	87
Pamir	75	1.92±0.48	-4.09±3.24	-	11
Models					
New Zealand	59[†]	1.5	-1.30	-	-
Japan	122[†‡]	1.57±0.04	-0.60	-	3424

[†] The reported α-value is 0.05±0.02. Note this error is symmetrical and differs from the other values in the table.

[‡] Based on a model where volume=(1/3) *h A*; where *h* is the elevation difference between the landslide toe and head scarp, which is described by an empirical power-law function of landslide area *A*. The scaling coefficients reported here are based on values for 11 different rock types and the ± symbol indicates standard error of the 11 values. The α-value is 0.25±0.18. Note this error is symmetrical and differs from the other values in the table.

Supplementary Figures

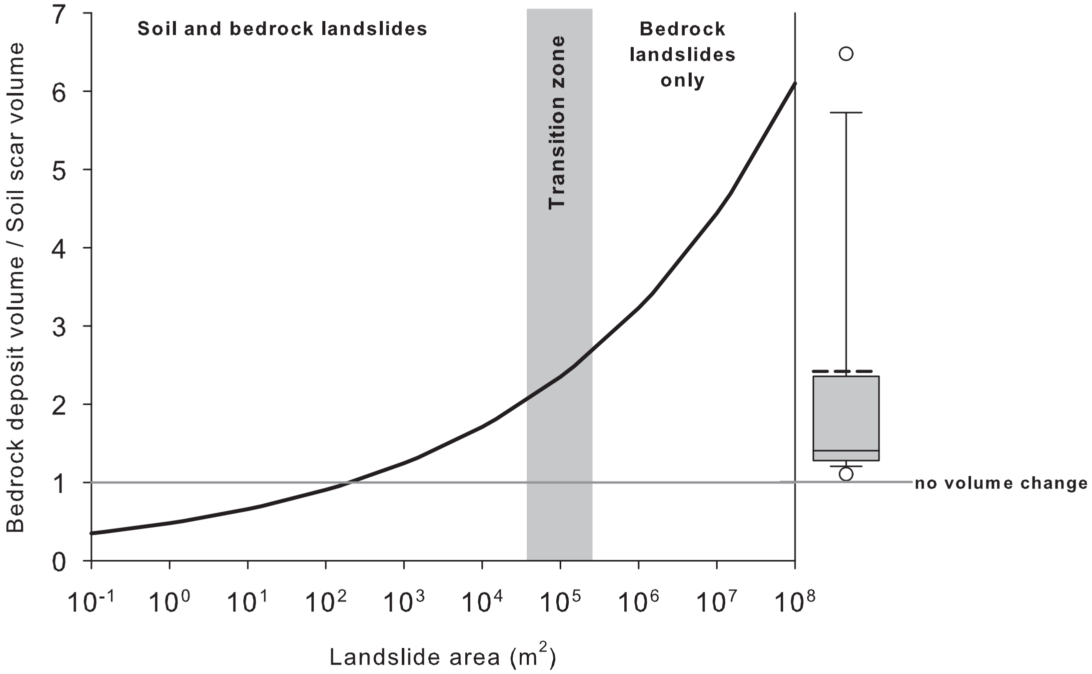

Figure A1.1. The ratio of bedrock landslide deposit volume to soil scar volume as a function of landslide area. The black curve was calculated using the scaling relationships in Table A1.1 and shows the magnitude of bulking that would be required to cause the difference in *V-A* scaling for soil and bedrock landslides. This analysis assumes *V-A* scaling for bedrock landslide scars is identical to soil landslide scaling, i.e., the inflection in *V-A* data that occurs at a landslide area of approximately 10^5 m^2 (shown in Fig. 2.2) is solely due to bulking of large bedrock landslides via dilation of the rock mass and entrainment of material in the runout path. The grey line indicates no bulking, where landslide scar and deposit volumes are equal. The boxplot shows the distribution of 42 published bulking values (refs. 2, 29, 30, 33, 50, 64, 65, 75, 78, 86, 96, 102, 105, 117, 125, 149-165). The solid line within the box denotes the median, the dashed line is the mean, the box spans the inter-quartile range, whiskers show the 10th and 90th percentiles, and the circles show the 5th and 95th percentiles. The range of published bulking values spans the range of deposit to scar volume ratios. However, if bulking caused the inflection in *V-A* data, the magnitude of bulking for each landslide in our dataset would have to be greater than the 75th percentile of published values. Given there is no evidence of systematic extreme bulking for the landslides in our dataset, we conclude that bulking has not caused the observed inflection in *V-A* scaling and the greater thickness of large bedrock landslide deposits.

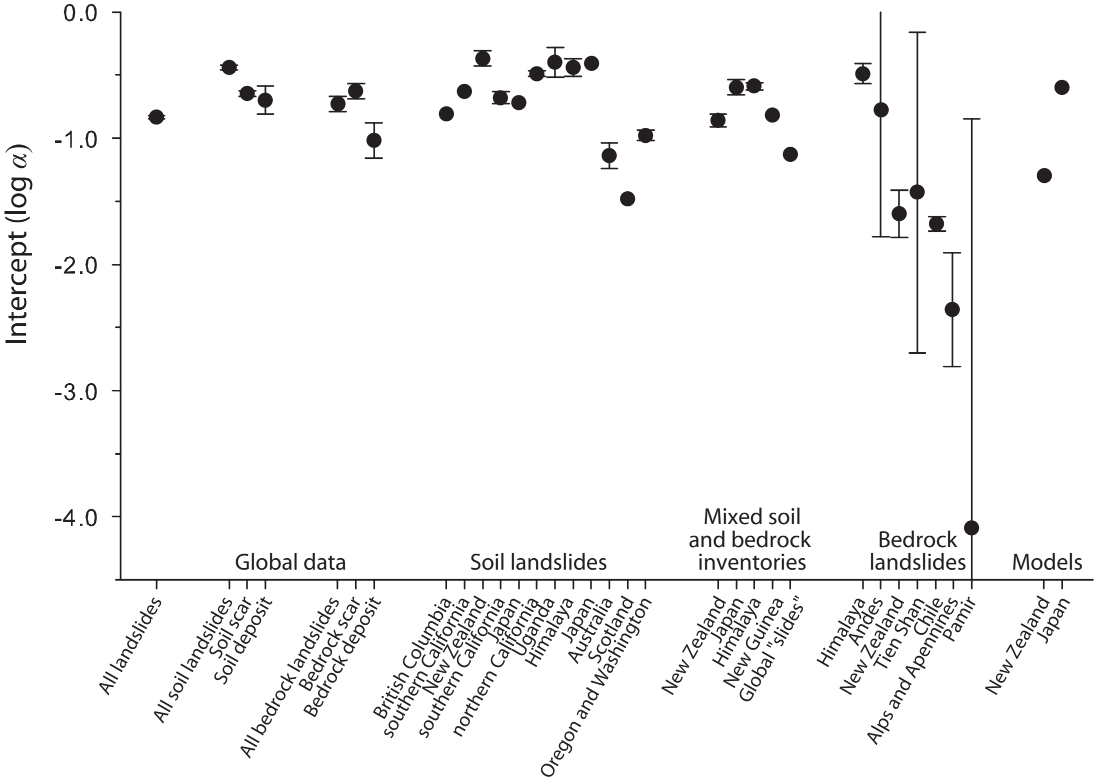

Figure A1.2. Intercept values (*α*) from the regional datasets used in this study, previous empirical studies, and proposed models. Landslide inventories are classified based on dominant landslide type. The circles are mean or reported values; error bars denote 1-standard error or reported errors. The data sources are listed in Table A1.1.

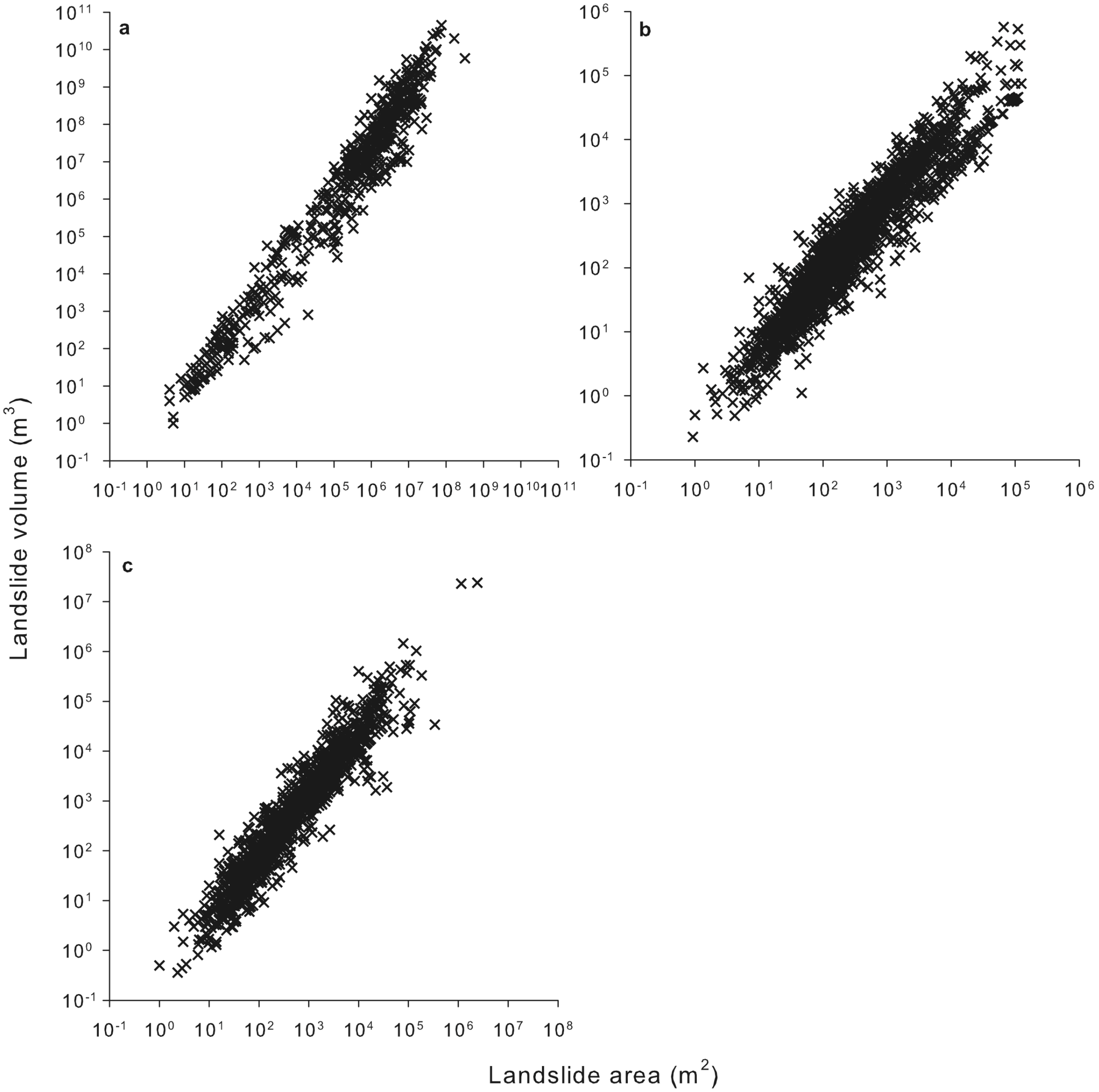

Figure A1.3. Landslide volume versus area for a) bedrock landslides (*n* = 604, b) soil landslides (*n* = 2136), and c) undifferentiated landslides (*n* = 1491).

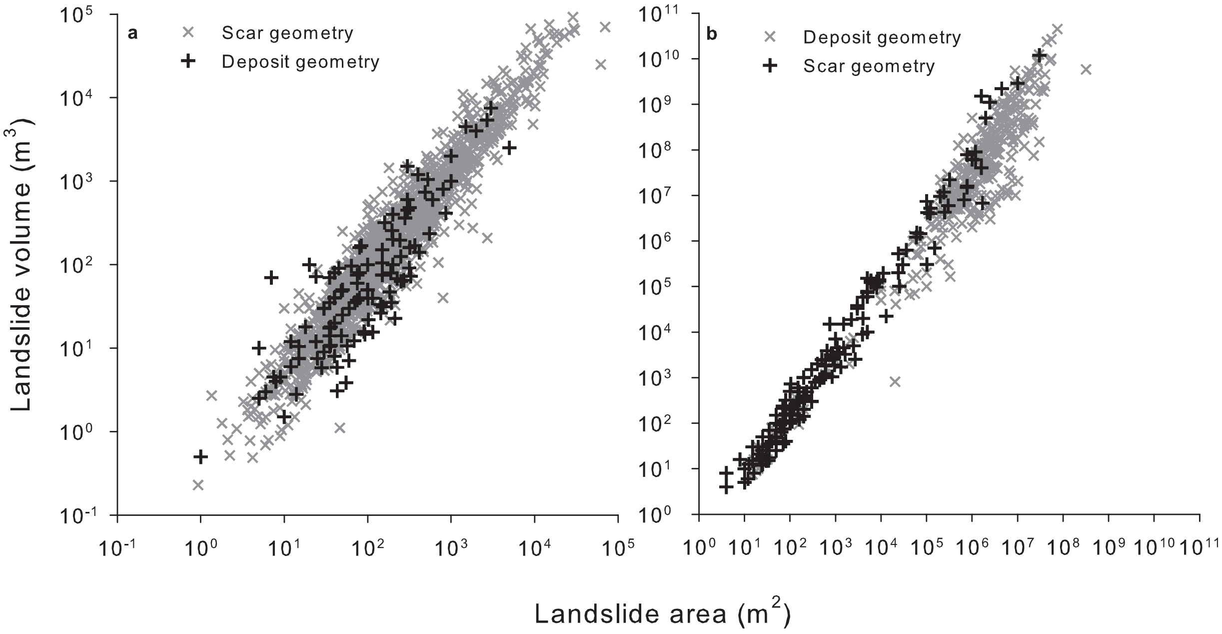

Figure A1.4. Landslide volume versus area for a) soil landslides differentiated by measurements of scar (*n*=1617) and deposit (*n*=124) geometry and b) bedrock landslides differentiated by measurements of scar (*n*=168) and deposit (*n*=344) geometry.

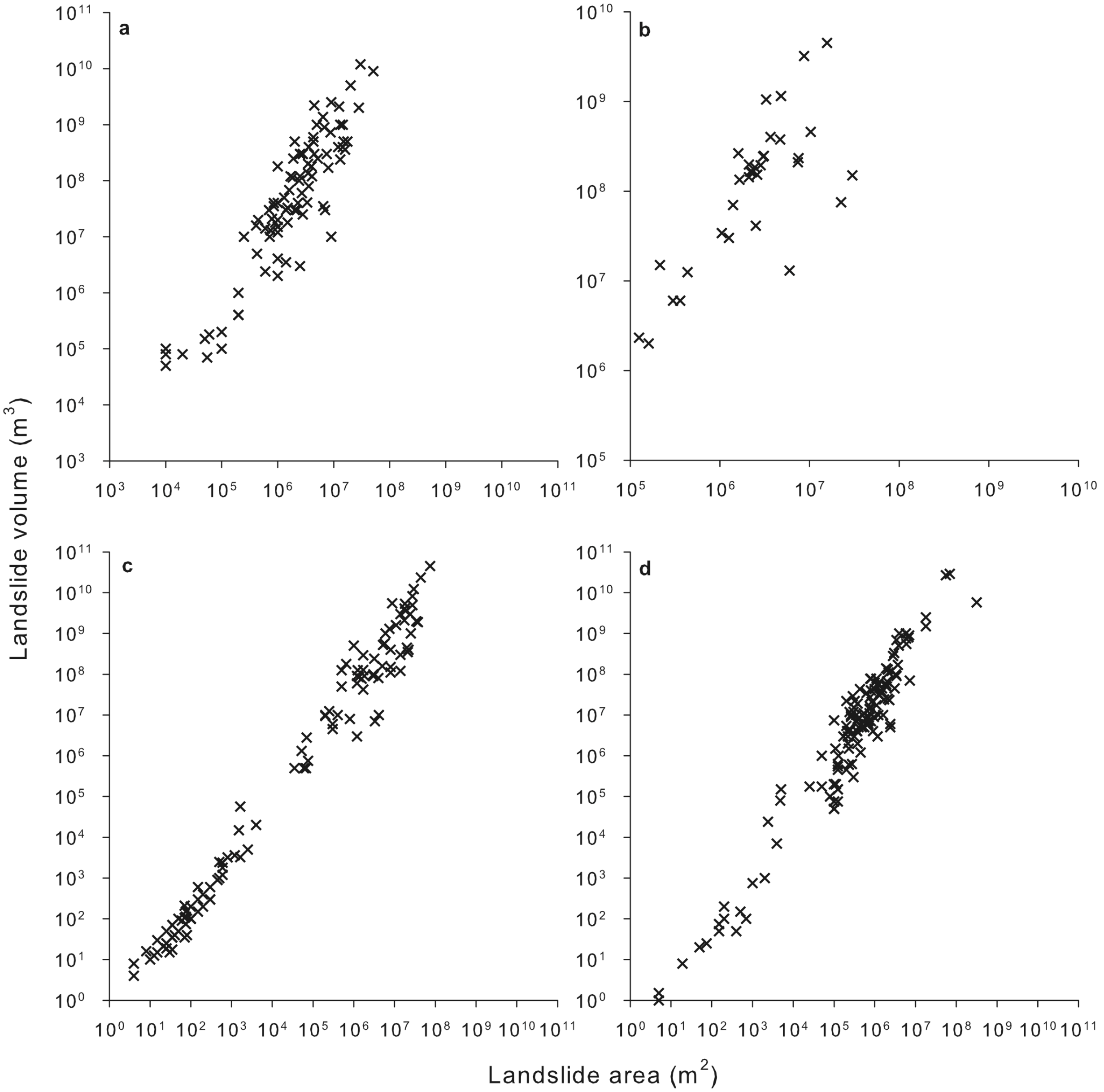

Figure A1.5. Landslide volume versus area for bedrock landslides for a) Alps and Apennines (*n* = 87), b) Andes (*n* = 33), c) Himalaya (*n* = 123), and d) New Zealand (*n* = 140).

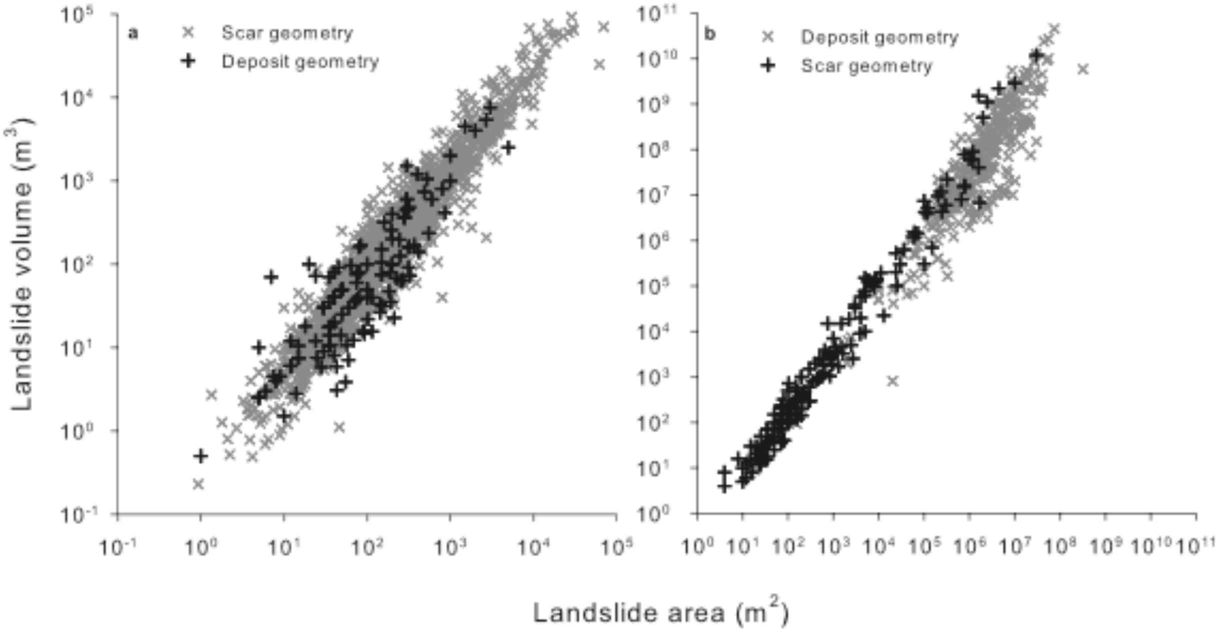

Figure A1.6. Landslide volume versus area for mixed bedrock and soil landslides for a) Himalaya (*n* = 428), b) Japan (*n* = 236), and c) New Zealand (*n* = 389).

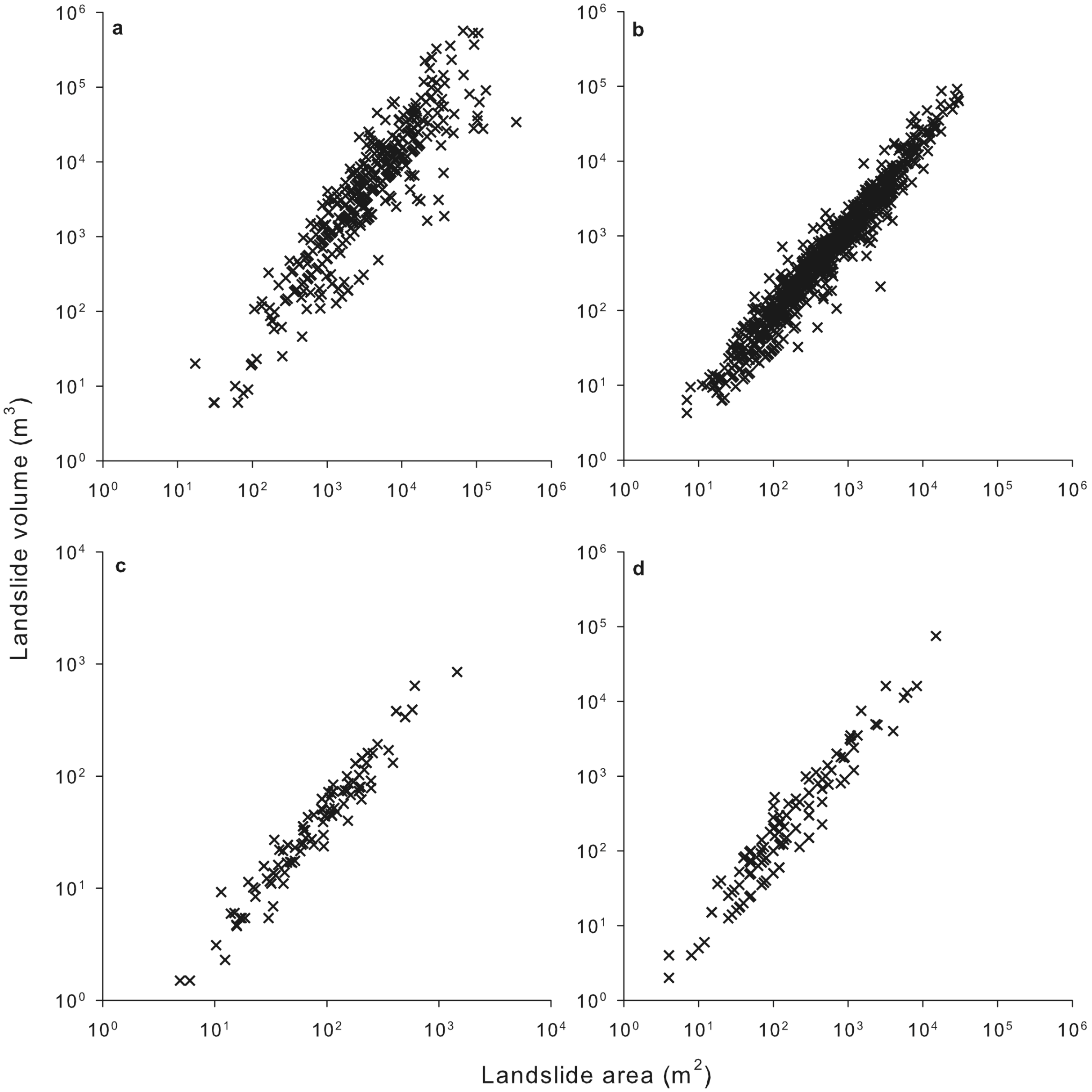

Figure A1.7. Landslide volume versus area for predominantly soil landslide inventories for a) Australia (*n* = 426), b) northern California (*n* = 956), c) southern California (*n* = 117), and d) Himalaya (*n* = 141).

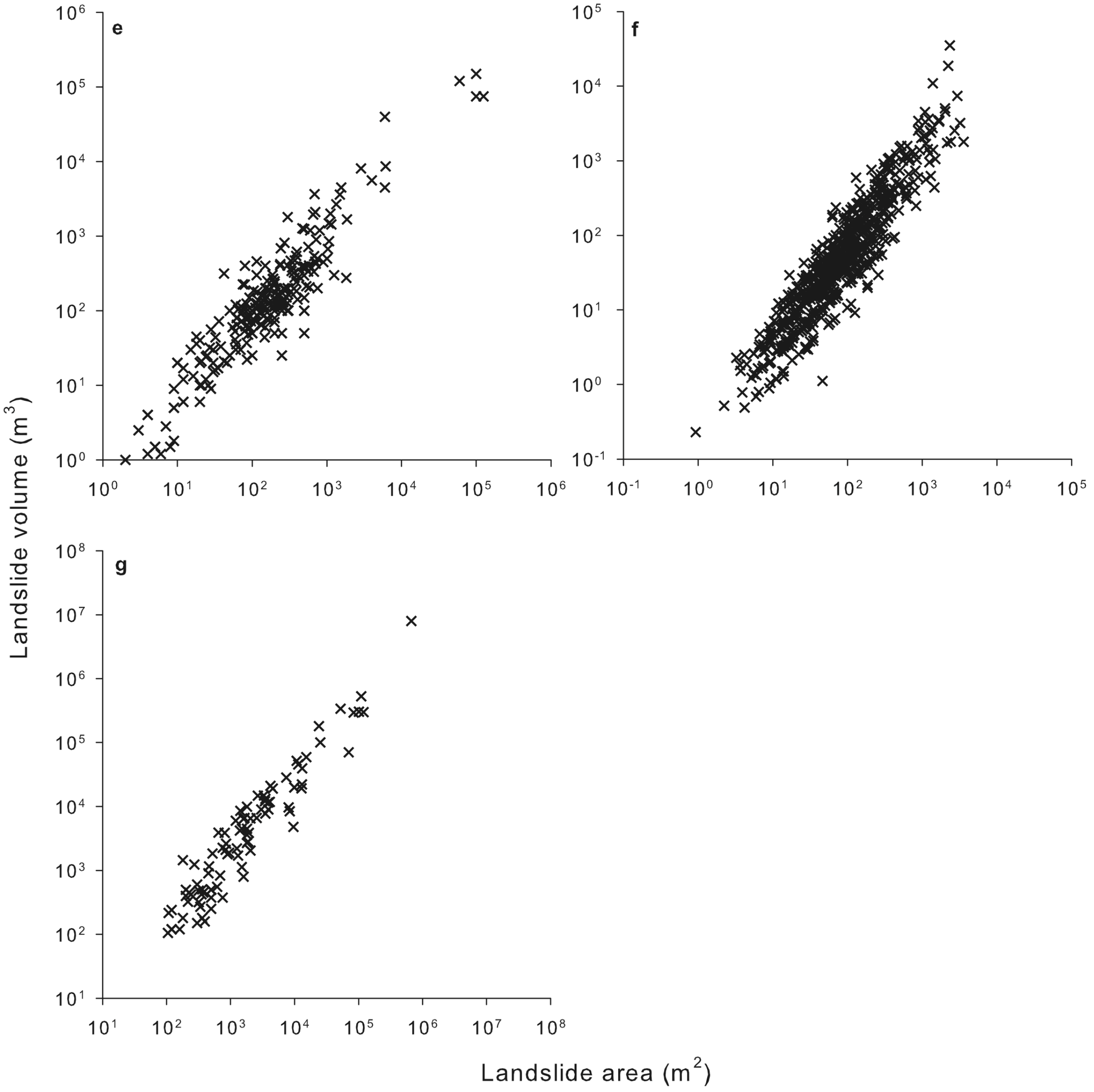

Figure A1.7 (continued). Landslide volume versus area for predominantly soil landslide inventories for e) New Zealand (*n* = 237), f) Oregon and Washington (*n* = 684), and g) Uganda (*n* = 93).

Supplementary References

1. Abdrakhmatov, K. & Strom, A. in *Landslides from massive rock slope failure. Proceedings of the NATO Advanced research workshop on massive rock slope failure: New models for hazard assesment* (eds Evans, S.G., Mugnozza, G.S., Strom, A. & Hermanns, R.L.) 551-572 (Springer, 2006).
2. Abele, G. *Bergstürze in den Alpen—ihre Verbreitung, Morphologie und Folgeerscheinungen*. Vol. 25 (1974).
3. Adushkin, V. in *Landslides from massive rock slope failure. Proceedings of the NATO Advanced research workshop on massive rock slope failure: New models for hazard assesment* (eds Evans, S.G., Mugnozza, G.S., Strom, A. & Hermanns, R.L.) 267-284 (Springer, 2006).
4. Alloway, B., Pillans, B., Carter, L., Naish, T. & Westgate, J. Onshore–offshore correlation of Pleistocene rhyolitic eruptions from New Zealand: implications for TVZ eruptive history and paleoenvironmental construction. *Quat. Sci. Rev.* **24**, 1601-1622 (2005).
5. Antinao, J. L. & Gosse, J. Large rockslides in the Southern Central Andes of Chile (32-34.5°S): Tectonic control and significance for Quaternary landscape evolution. *Geomorphology*, 117-133 (2009).
6. Antognini, M. & Volpers, R. A Late Pleistocene Age for the Chironico rockslide (Central Alps, Ticino, Switzerland). *Bull. Appl. Geol.* **7**, 113-125 (2002).
7. Arsenault, A. & Meigs, A. Contribution of deep-seated bedrock landslides to erosion of a glaciated basin in southern Alaska. *Earth Surf. Processes Landforms* **30,** 1111-1125 (2005).
8. Badger, T. C. *Geomorphology and failure mechanisms of gigantic landslides within Summer Lake Basin: Implications for seismogenic triggers, Lake County, Oregon.* MS thesis, University of Nevada, Reno (2002).
9. Barla, G. & Barla, M. in *Rock mechanics: a challenge for society : proceedings of the ISRM Regional Symposium EUROROCK.* (eds Särkkä, P. & Eloranta, P.) 35-40 (Taylor & Francis, 2001).
10. Barnard, P., Owen, L., Sharma, M. & Finkel, R. Natural and human-induced landsliding in the Garhwal Himalaya of northern India. *Geomorphology* **40**, 21-35 (2001).
11. Bartarya, S. & Valdiya, K. Landslides and erosion in the catchment of the Gaula River, Kumaun Lesser Himalaya, India. *Mt. Res. Dev.* **9**, 405-419 (1989).
12. Beetham, R., McSaveney, M. & Read, S. in *Landslides: Proceedings of the First European Conference on Landslides.* (Taylor & Francis, 2002).
13. Blodgett, T. A. & Isacks, B. L. Landslide Erosion Rate in the Eastern Cordillera of Northern Bolivia. *Earth Int.* **11**, 1-30 (2007).
14. Blong, R. *Landform Morphometry and Landsurface Evolution in the Upper Mangawhara Catchment, North Island, New Zealand*. PhD thesis, University of Sydney (1971).
15. Breien, H., Blasio, F. V., Elverhøi, Høeg, K. Erosion and morphology of a debris flow caused by a glacial lake outburst flood Western Norway. *Landslides*, **5**, 271-280 (2008).
16. Caine, N. & Mool, P. Landslides in the Kolpu Khola drainage, middle mountains, Nepal. *Mt. Res. Dev.* **2**, 157-173 (1982).

17. Chang, K.-J., Taboada, A., & Chan, Y.C. Geological and morphological study of the Jiufengershan landslide triggered by the Chi-Chi Taiwan earthquake. *Geomorphology*. **71**, 293-309 (2005).
18. Corsini, A., Pasuto, A., Soldati, M. & Zannoni, A. Field monitoring of the Corvara landslide (Dolomites, Italy) and its relevance for hazard assessment. *Geomorphology*, **66**, 149-165 (2005).
19. Costa, J. & Schuster, R. Documented Historical Landslide Dams From Around the World. USGS Open-file report 91-239 (1991).
20. Cox, S. C. & Allen, S. K. Vampire rock avalanches of January 2008 and 2003, Southern Alps, New Zealand. *Landslides* **6**, 161-166 (2009).
21. Cruden, D. Major rock slides in the Rockies. *Can. Geotech. J.* **13**, 8-20 (1976).
22. Cruden, D. & Krahn, J. in *Rockslides and Avalanches* Vol. 1 (ed Voight, B.) 97–112 (Elsevier, 1978).
23. Dai, F., Deng, J., Tham, L., Law, K. & Lee, C. A large landslide in Zigui County, Three Gorges area. *Can. Geotech. J.* **41**, 1233-1240 (2004).
24. Dapples, F., Oswald, D., Raetzo, H., Lardelli, T. & Zwahlen, P. New records of Holocene landslide activity in the western and eastern Swiss Alps: Implication of climate and vegetation changes. *Eclogae Geol. Helv.* **96**, 1-9 (2003).
25. Davis, S. & Karzulovic, K. Landslides at Lago Rinihue, Chile. *Bull. Seismol. Soc. Am.* **53**, 1403-1414 (1963).
26. Deng, Q. L., Zhu, Z. Y., Cui, Z. Q., & Wang, X. P. Mass rock creep and landsliding on the Huangtupo slope in the reservoir area of the Three Gorges Project, Yangtze River, China. *Eng. Geol.* **58**, 67-83 (2000).
27. Dewitte *et al*. Tracking landslide displacements by multi-temporal DTMs: A combined aerial stereophotogrammetric and LIDAR approach in western Belgium. *Eng. Geol.* **99**, 11-22 (2008).
28. Dortch, J. *et al.* Nature and timing of large landslides in the Himalaya and Transhimalaya of northern India. *Quat. Sci. Rev.* **28**, 1037-1054 (2009).
29. Douglass, J., Dorn, R. I., Gootee, B. A large landslide on the urban fringe of metropolitan Phoenix, Arizona. *Geomorphology* **65**, 321-336 (2005).
30. Dunning, S. A., Rosser, N. J., Petley, D. N., & Massey, C. R. Formation and failure of the Tsatichhu landslide dam, Bhutan. *Landslides*, **3**, 107-113, (2006).
31. Dunning, S., Mitchell, W., Rosser, N. & Petley, D. The Hattian Bala rock avalanche and associated landslides triggered by the Kashmir Earthquake of 8 October 2005. *Eng. Geol.* **93**, 130-144 (2007).
32. Egger, V. H., *et al.* Erläuterungen zu Blatt 67 Grünau im Almtal. Geologische Bundesanstalt, Wein, 68 p. (2007).
33. Eisbacher, G. & Clague, J. *Destructive Mass Movements in High Mountains: Hazard and Management*. Vol. 84-16 (Geological Survey of Canada, 1984).
34. Ermini, L. & Casagli, N. Prediction of the behaviour of landslide dams using a geomorphological dimensionless index. *Earth Surf. Processes Landforms* **28**, 31-47 (2003).
35. Evans, S. & Savigny, K. Landslides in the Vancouver–Fraser Valley–Whistler region. *Geology and Geological Hazards of the Vancouver Region, Southwestern British Columbia.* (ed Monger, J. W. H.) *Geological Survey of Canada, Bulletin* **481**, 251–286 (1994).

36. Fauqué, L. & Tchilinguirian, P. in *Catastrophic rockslides: Effects, occurrence, and mechanisms* Vol. 15 *Reviews in Engineering Geology* (eds Evans, S.G. & DeGraff, J.V.) 303-324 (Geological Society of America, 2002).
37. Flentje, P. & Chowdhury, R. in *Proceedings of the GeoQuest Symposium on Planning for Natural Hazards - How can we mitigate the impacts?* (ed Morrison, J.) 65-78 (GeoQuest Research Centre, 2005).
38. Gabet, E. & Dunne, T. Landslides on coastal sage-scrub and grassland hillslopes in a severe El Niño winter: The effects of vegetation conversion on sediment delivery. *Geol. Soc. Am. Bull.* **114**, 983-990 (2002).
39. Genevois, R., Armento, C. & Tecca, P. in *Landslides from massive rock slope failure. Proceedings of the NATO Advanced research workshop on massive rock slope failure: New models for hazard assesment* (eds Evans, S.G., Mugnozza, G.S., Strom, A. & Hermanns, R.L.) 407-427 (Springer, 2006).
40. Gianotti, F., Crosta, G., Frattini, P. & Chen, H. Geomorphological mapping and numerical modelling of the Becca France rock avalanche (Aosta Valley, Italy) *Geophys. Res. Abstr.* **8**, 08784 (2006).
41. GNS Science. *GeoNet New Zealand Landslide Catalogue*, http://www.geonet.org.nz/resources/landslide/landslide-catalogue.html (2009).
42. Guthrie, R. *The Characterization and Dating of Landslides in the Tsitika River and Schmidt Creek Watersheds, Northern Vancouver Island, British Columbia* MSc thesis, University of Victoria (1997).
43. Guthrie, R. & Evans, S. Analysis of landslide frequencies and characteristics in a natural system, coastal British Columbia. *Earth Surf. Processes Landforms* **29**, 1321-1339 (2004).
44. Guzzetti, F., Ardizzone, F., Cardinali, M., Rossi, M. & Valigi, D. Landslide volumes and landslide mobilization rates in Umbria, central Italy. *Earth. Planet. Sci. Lett.* 222-229 (2009).
45. Hancox, G., Cox, S., Turnbull, I. & Crozier, M. Reconnaissance Studies of Landslides and Other Ground Damage Caused by the Mw 7.2 Fiordland Earthquake of 22 August 2003 (Institute of Geological & Nuclear Sciences, Lower Hutt, 2003).
46. Hancox, G. & Perrin, N. Green Lake landslide and other giant and very large postglacial landslides in Fiordland, New Zealand. *Quat. Sci. Rev.* **28**, 1020-1036 (2009).
47. Hansen, L., Eilertsen, R., Solberg, I.-L., Rokoengen, K. Stratigraphic evaluation of a Holocene clay-slide in northern Norway. *Landslides*, **4**, 233-244 (2007).
48. Harp, E. & Jibson, R. Landslides triggered by the 1994 Northridge, California, earthquake. *Bull. Seismol. Soc. Am.* **86**, 319-332 (1996).
49. Harrison, J. & Falcon, N. An ancient landslip at Saidmarreh in southwestern Iran. *J. Geol.* **46**, 296-309 (1938).
50. Hauser, A. in *Catastrophic Landslides: Effects, Occurrence, and Mechanisms* Vol. 15 *Reviews in Engineering Geology* (eds Evans, S.G. & DeGraff, J.V.) 135-148 (Geological Society of America, 2002).
51. Havenith, H.-B. *et al.* Seismic triggering of landslides, Part A: Field evidence from the Northern Tien Shan. *Nat. Hazard. Earth Syst. Sci.* **3**, 135-149 (2003).

52. Hermanns, R. & Strecker, M. Structural and lithological controls on large Quaternary rock avalanches (sturzstroms) in arid northwestern Argentina. *Geol. Soc. Am. Bull.* **111**, 934-948 (1999).
53. Hermans, R., Niedermann, S., Villanueva Garcia, A. & Schellenberger, A. in *Landslides from massive rock slope failure. Proceedings of the NATO Advanced research workshop on massive rock slope failure: New models for hazard assesment* (eds Evans, S.G., Mugnozza, G.S., Strom, A. & Hermanns, R.L.) 497-520 (Springer, 2006).
54. Heuberger, H., Masch, L., Preuss, E. & Schrocker, A. Quaternary landslides and rock fusion in Central Nepal and in the Tyrolean Alps. *Mt. Res. Dev.* **4**, 345-362 (1984).
55. Hewitt, K. Catastrophic Landslide Deposits in the Karakoram Himalaya. *Science* **242**, 64-67 (1988).
56. Hewitt, K. Catastrophic landslides and their effects on the Upper Indus streams, Karakoram Himalaya, northern Pakistan. *Geomorphology* **26**, 47-80 (1998).
57. Hewitt, K. in *Catastrophic Landslides: Effects, Occurrence, and Mechanisms* Vol. 15 *Reviews in Engineering Geology* (eds Evans, S.G. & DeGraff, J.V.) 345-377 (Geological Society of America, 2002).
58. Hewitt, K., Clague, J. & Orwin, J. Legacies of catastrophic rock slope failures in mountain landscapes. *Earth Sci. Rev.* **87**, 1-38 (2008).
59. Hovius, N., Stark, C. & Allen, P. Sediment flux from a mountain belt derived by landslide mapping. *Geology* **25**, 231-234 (1997).
60. Hung, J.-J. Chi-Chi earthquake induced landslides in Taiwan. *Earthquake Eng. & Eng. Seismol.* **2**, 25-33, (2000).
61. Imaizumi, F. & Sidle, R. Linkage of sediment supply and transport processes in Miyagawa Dam catchment, Japan. *J. Geophys. Res.* **112**, F03012 (2007).
62. Imaizumi, F., Sidle, R. & Kamei, R. Effects of forest harvesting on the occurrence of landslides and debris flows in steep terrain of central Japan. *Earth Surf. Processes Landforms* **33**, 827 (2008).
63. Innes, J. Lichenometric dating of debris-flow deposits in the Scottish Highlands. *Earth Surf. Processes Landforms* **8**, 579-588 (1983).
64. Jäckli, H. Gegenwartsgeologie des bu¨ndnerischen Rheingebietes. *Beitr. Geol. Schweiz Geotech.* **36** (1957).
65. Jarman, D. Rock slope failure and landscape evolution in the Caledonian Mountains, as exemplified in the Abisko area, northern Sweden. *Geogr. Ann. Ser. A* **84**, 213-224 (2002).
66. Jibson, R. W. The 2005 La Conchita, California, landslide. *Landslides*, **3**, 73-78 (2006).
67. Jibson, R., Harp, E., Schulz, W. & Keefer, D. Large rock avalanches triggered by the M 7.9 Denali Fault, Alaska, earthquake of 3 November 2002. *Eng. Geol.* **83**, 144-160 (2006).
68. Johnson, B. in *Rockslides and Avalanches* Vol. 1 (ed Voight, B.) 481-504 (Elsevier, 1978).
69. Kelsey, H., Coghlan, M., Pitlick, J. & Best, D. Geomorphic Analysis of Streamside Landslides in the Redwood Creek Basin, Northwestern California. USGS Professional Paper 1454-J, J1-J12 (1995).
70. Kilburn, C. & Petley, D. Forecasting giant, catastrophic slope collapse: lessons from Vajont, Northern Italy. *Geomorphology* **54**, 21-32 (2003).
71. Knapen, A. *et al.* Landslides in a densely populated county at the footslopes of Mount Elgon (Uganda): Characteristics and causal factors. *Geomorphology* **73**, 149-165 (2006).

72. Korup, O. *Landslide-induced river disruption—Geomorphic imprints and scaling effects in alpine catchments of South Westland and Fiordland, New Zealand*. PhD thesis, Victoria University (2003).
73. Korup, O. Geomorphic implications of fault zone weakening: slope instability along the Alpine Fault, South Westland to Fiordland. *New Zeal. J. Geol. Geophys.* **47**, 257-267 (2004).
74. Korup, O. Distribution of landslides in southwest New Zealand. *Landslides* **2**, 43-51 (2005).
75. Korup, O. Effects of large deep-seated landslides on hillslope morphology, western Southern Alps, New Zealand. *J. Geophys. Res.* **111**, F01018, doi:doi:10.1029/2004JF000242 (2006).
76. Korup O. & Crozier, M. Landslide types and geomorphic impact on river channels, Southern Alps, New Zealand. in *Proceedings of the first European conference on landslides*, (eds Rybar J., Stemberk J., Wagner, P.) Prague, 233–238 (2002).
77. Korup, O. *et al.* Giant landslides, topography, and erosion. *Earth. Planet. Sci. Lett.* **261**, 578-589 (2007).
78. Lang, A., Moya, J., Corominas, J., Schrott, L. & Dikau, R. Classic and new dating methods for assessing the temporal occurrence of mass movements. *Geomorphology* **30**, 33-52 (1999).
79. Larsen, I. *From the Rim to the River: The Geomorphology of Debris Flows in the Green River Canyons of Dinosaur National Monument, Colorado and Utah* M.S. thesis, Utah State University (2003).
80. Larsen, I. & Montgomery, D. *Landslides measured in the Siang River drainage, Arunachal Pradesh, India* (this study).
81. Lin, M., Wang, K. & Chen, T. in *International Workshop on Annual Commemeration of Chi-Chi Earthquake, Taipei*. 199-209 (National Center for Research on Earthquake Engineering, 2000).
82. Logar, J. et al. History and present state of the Slano Blato landslide. *Nat. Hazard. Earth Syst. Sci.* **5**, 447-457 (2005).
83. Mathews, W. & McTaggart, K. in *Rockslides and Avalanches* Vol. 1 (ed Voight, B.) 259-278 (Elsevier, 1978).
84. May, C. Debris flows through different forest age classes in the central Oregon Coast Range. *J. Am. Water Resour. As.* **38**, 1097-1113 (2002).
85. McSaveney, M. in *Rockslides and Avalanches* Vol. 1 (ed Voight, B.) 197-258 (Elsevier, 1978).
86. McSaveney, M. in *Catastrophic Landslides: Effects, Occurrence, and Mechanisms,* Vol. 15 *Rev. Eng. Geol.* (eds Evans, S.G. & DeGraff, J.V.) 35-70 (Geological Society of America, 2002).
87. Mikoš, M., Fazarinc, R., Pulko, B., Petkovsek, A. & Majes, B. Stepwise mitigation of the Macesnik landslide, N Slovenia. *Nat. Hazard. Earth Syst. Sci.* **5**, 947-958 (2005).
88. Montgomery, D. *Landslides measured at Coos Bay, Oregon, USA* (this study).
89. Moon, V. & Simpson, C. Large-scale mass wasting in ancient volcanic materials. *Eng. Geol.* **64**, 41-64 (2002).
90. Mudge, M. Rockfall-avalanche and rockslide-avalanche deposits at Sawtooth Ridge, Montana. *Bull. Geol. Soc. Am.* **76**, 1003-1014 (1965).

91. Nicoletti, P. & Sorriso-Valvo, M. Geomorphic controls of the shape and mobility of rock avalanches. *Geol. Soc. Am. Bull.* **103**, 1365-1373 (1991).
92. Okada, Y., Ochiai, H., Kurokawa, U., Ogawa, Y., & Asano, S. A channelised long run-out debris slide triggered by the Noto Hanto Earthquake in 2007, Japan. *Landlides* **5**, 235-239 (2008).
93. Orwin, J. F., Clague, J. J. & Gerath, R. F. The Cheam rock avalanche, Fraser Valley, British Columbia, Canada. *Landslides* **1**, 289-298 (2004).
94. Pain, C. *Mass movement and vegetation in the Orere River catchment, Hunua Ranges*. MA thesis, University of Auckland, (1968).
95. Pánek, T., Hradecký, J., Smolková, V. & Šilhán, K. Gigantic low-gradient landslides in the northern periphery of the Crimean Mountains (Ukraine). *Geomorphology* **95**, 449-473 (2008).
96. Peart, M. The Kaiapit Landslide: events and mechanisms. *Quarterly Journal of Eng. Geol. & Hydrogeol.* **24**, 399-411 (1991).
97. Pedersen, S. A. S. *et al.* Tsunami-generating rock fall and landslide on the south coast of Nuussuaq, central West Greenland. *Geology of Greenland Survey Bulletin* **191**, 73-83 (2002).
98. Pellegrini, G. & Surian, N. Geomorphological study of the Fadalto landslide, Venetian Prealps, Italy. *Geomorphology* **15**, 337-350 (1996).
99. Perrin, N. & Hancox, G. in *Landslides. Glissements de Terrain. Proceedings of the Sixth International Symposium* (ed Bell, D.H.) 1457–1466 (Balkema, Christchurch, 1992).
100. Piteau, D., Mylrea, F. & Blown, I. in *Rockslides and Avalanches* Vol. 1 (ed Voight, B.) 365-392 (Elsevier, 1978).
101. Pitlick, J. Sediment routing in tributaries of the Redwood Creek Basin, northwestern California. USGS Professional Paper 1454-K, K1-K10 (1995).
102. Plafker, G. & Ericksen, G. in *Rockslides and Avalanches* Vol. 1 (ed Voight, B.) 277–314 (Elsevier, 1978).
103. Porter, S. & Ormbelli, G. Catastrophic rockfall of setember 1717 on the Italian flank of the Mont Blanc massif. *Z. Geomorphol.* **24**, 200-218 (1980).
104. Prager, C. & Zangerl, C. Kinematics of a long run-out rockslide: a case study from the Fernpass-region (Northern Calcareous Alps, Tyrol, Austria) *Geophys. Res. Abstr.* **7**. 02737 (2005).
105. Prager, C., Zangerl, C., Patzelt, G. & Brandner, R. Age distribution of fossil landslides in the Tyrol (Austria) and its surrounding areas. *Nat. Hazard. Earth Syst. Sci.* **8**, 377-407 (2008).
106. Raetzo, H., Lateltin, O., Bollinger, D. & Tripet, J. Hazard assessment in Switzerland-Codes of Practice for mass movements. *Bull. Eng. Geol. Environ.* **61**, 263-268 (2002).
107. Reid, L. *Sediment production from gravel-surfaced forest roads, Clearwater Basin, Washington*. MS thesis, University of Washington (1981).
108. Reid, L. M. *Landslides measured at Caspar Creek, California, USA* (pers. comm.).
109. Rice, R., Crobett, E. & Bailey, R. Soil slips related to regetation, topography, and soil in Southern California. *Water Resour. Res.* **5**, 647-659 (1969).
110. Rice, R. & Foggin, G. Effect of high intensity storms on soil slippage on mountainous watersheds in southern California. *Water Resour. Res.* **7**, 1485-1496 (1971).

111. Robison, E., Mills, K., Paul, J., Dent, L. & Skaugset, A. Storm Impacts and Landslides of 1996: Final Report. (Oregon Department of Forestry Forest Practices Monitoring Program, 1999).

112. Runqiu, H. Some catastrophic landslides since the twentieth centuryin the southwest of China. *Landslides* **6**, 69-81 (2009).

113. Scarascia-Mugnozza, G., Bianchi-Fasani, G., Esposito, C., Di Luzio, E. & Evans, S. in *Landslides from massive rock slope failure. Proceedings of the NATO Advanced research workshop on massive rock slope failure: New models for hazard assesment* (eds Evans, S.G., Mugnozza, G.S., Strom, A. & Hermanns, R.L.) 357-376 (Springer, 2006).

114. Seno, S. & Thüring, M. Large landslides in Ticino, Southern Switzerland: Geometry and kinematics. *Eng. Geol.* **83**, 109-119 (2006).

115. Shroder, J. Slope failure and denudation in the western Himalaya. *Geomorphology* **26**, 81-105 (1998).

116. Simonett, D. in *Landform studies from Australia and New Guinea* (eds Jennings, J.N. & Mabbutt, J.A.) 64-84 (Australian National University Press, 1967).

117. Smith, G. M., Davies, T. R., McSaveney, M. J., & Bell, D. H. The Acheron rock avalanche, Canterbury, New Zealand—morphology and dynamics. *Landslides* **3**, 62-72 (2006).

118. Springer, G., Dowdy, H. & Eaton, L. Sediment budgets for two mountainous basins affected by a catastrophic storm: Blue Ridge Mountains, Virginia. *Geomorphology* **37**, 135-148 (2001).

119. Strom, A. Rock avalanches of the Ardon River Valley at the southern foot of the Rocky Range, Northern Caucasus, North Osetia. *Landsides* **1**, 237-241 (2004).

120. Strom, A. in *Landslides and Avalanches: ICFL 2005 Norway: Proceedings of the 11th International Conference and Field Trip on Landslides* (eds Senneset, K., Flaate, K. & Larsen, J.A.) 343-348 (Taylor & Francis, 2005).

121. Strom, A. & Korup, O. Extremely large rockslides and rock avalanches in the Tien Shan Mountains, Kyrgyzstan. *Landslides* **3**, 125-136 (2006).

122. Sugai, T., Ohmori, H. & Hirano, M. Rock control on the magnitude-frequency distribution of landslides. *Trans. Jpn. Geomorph. Union* **15**, 233-251 (1994).

123. Thomson, R. The 1984 Iris Burn Slip: a geological appraisal (Institute of Geological and Nuclear Sciences, Science Report 94/38, Lower Hutt, 1994).

124. Tibaldi, A., Graziotto, E., Forcella, F. & Gapich, V. Morphotectonic indicators of Holocene faulting in central Tien Shan, Kazakstan, and geodynamic implications. *J. Geodyn.* **23**, 23-45 (1997).

125. Tinner, W. & Ammann, B. in *Global Change and Mountain Regions. An overview of current knowledge* (eds Huber, U.M., Bugmann, H.K.M. & Reasoner, M.A.) 133–143 (Springer, 2005).

126. Tsutsui, K. *et al*. Detection and volume estimation of large-scale landslides based on elevation-change analysis using DEMs extracted from high resolution satellite stereo imagery. *IEEE Trans. Geosci. Remote Sens*. **45**, 1681-1696 (2007).

127. Uhlir, C. & Schramm, J. Zur Kinematik des Bergsturzes von Vingaun (Salzburg). *Bull. Angewandte Geologie* **93**, 161-173 (2003).

128. Van Dissen, R., Sutherland, D., Bowers, R. & Redwine, J. Forest burial by large rock avalanche in Miller Stream, Seaward Kaikoura Range, New Zealand, c. 1700 years ago. *New Zeal. J. Geol. Geophys.* **49**, 151-157 (2006).

129. von Poschinger, A. Some aspects of the "impact" of a landslide on a valley floor. *Landslide News* **8**, 26-28 (1994).

130. von Poschinger, A. The Flims rockslide dam. in Security of natural and artificial rockslide dams: extended abstracts volume,NATO Advanced Research Workshop, (eds Abdrakhmatov, K., Evans, S. G., Hermanns, R., Scarascia-Mugnozza, G. and Strom, A. L.) Bishkek, Kyrgyzstan, 8-13 June, 141-144 (2004).

131. von Poschinger, A. Der Flimser Bergsturz als Staudamm. *Bull. Angewandte Geologie* **10**, 33-47 (2005).

132. Wang, F.-W., Zhang, Y.-M., Huo, Z.-T., Matsumoto, T., and Huang, B.-L. The July 14, 2003 Qianjiangping landslide, Three Gorges Reservoir, China. *Landslides* **1**, 157-162 (2004).

133. Wang, G., Suemine, A., Furuya, G., Kaibori, M., & Sassa, K. Rainstorm-induced landslides at Kisawa village, Tokushima Prefecture, Japan, August 2004. *Landslides* **2**, 235-242 (2005).

134. Wei, M., Fujun, N., Satoshi, A., Dewu, J. Slope instability phenomena in permafrost regions of Qinghai-Tibet Plateau, China. *Landslides* **3**, 260-264 (2006).

135. Weidinger, J. Predesign, failure and displacement mechanisms of large rockslides in the Annapurna Himalayas, Nepal. *Eng. Geol.* **83**, 201-216 (2006).

136. Whitehouse, I. Distribution of large rock avalanche deposits in the central Southern Alps, New Zealand. *New Zeal. J. Geol. Geophys.* **26**, 271-279 (1983).

137. Wieczorek, G., Larsen, M., Eaton, L., Morgan, B. & Blair, J. Debris-flow and flooding hazards associated with the December 1999 storm in coastal Venezuela and strategies for mitigation. Open File Report 01-144 (U.S. Geological Survey, 2001).

138. Wieczorek, G., Eaton, L., Yanosky, T. & Turner, E. Hurricane-induced landslide activity on an alluvial fan along Meadow Run, Shenandoah Valley, Virginia (eastern USA). *Landslides* **3**, 95-106 (2006).

139 Wieczorek, G., Geist, E. L., Motyka, R. J., & Jakob, M. Hazard assessment of the Tidal Inlet landslide and potential subsequent tsunami, Glacier Bay National Park, Alaska. *Landslides* **4**, 205-215 (2007).

140. Wright, C. The AD 930 long-runout Round Top debris avalanche, Westland, New Zealand. *New Zeal. J. Geol. Geophys.* **41**, 493-497 (1999).

141. Yamagishi H. et al. Estimation of the sequence and size of the Tozawagawa landslide, Niigata, Japan, using aerial photographs. *Landslides* **1**, 229-303 (2004).

142. Yamagishi, H. & Iwahashi, J. Comparison between the two triggered landslides in Mid-Niigata, Japan by July 13 heavy rainfall and October 23 intensive earthquakes in 2004. *Landslides* **4**, 389-397 (2007).

143. Zêzere, J. L., Oliveira, S. C., Garcia, R. A. C., & Reis, E. Landslide risk analysis in the area north of Lisbon (Portugal): evaluation of direct and indirect costs resulting from a motorway disruption by slope movements. *Landslides* **4**, 123-136 (2007).

144. Zhang, Z., Chen, S. & Tao, L. in *Catastrophic Landslides: Effects, Occurrence, and Mechanisms*. Vol. 15 *Reviews in Engineering Geology* (eds Evans S.G. & DeGraff, J.V.) 149-163 (Geological Society of America, 2002).

145. Harp, E. & Jibson, R. Inventory of landslides triggered by the 1994 Northridge California, earthquake. Open-File Report 95-213 (US Geological Survey*,* 1995).

146. Iwahashi, J., Kamiya, I. & Yamagishi, H. Estimation of the most suitable window size of the slope gradient and convexo-concave index for the assessment of shallow landslides using high-resolution LiDAR DEM. *Trans. Jpn. Geomorph. Union* **30,** 15-27 (2009).
147. Batjes, N. H. A Homogenized Soil Profile Dataset for Global and Regional Environmental Research (WISE, Version 1.1) Report 2002/01 (International Soil Reference and Information Center, Wageningen, 2002).
148. Seney, J., Frazier, A. & Popenoe, J. Soil Survey of Redwood National and State Parks, California (USDA Natural Resources Conservation Service, 2008).
149. Badger, T. & Watters, R. J. Gigantic seismogenic landslides of Summer Lake basin, south-central Oregon. *Geol. Soc. Am. Bull*. **116**, 687-697 (2004).
150. Cambiaghi, A., & Schuster, R. L. Landslide damming and environmental protection – a case study from northern Italy. in *Proc. 2nd International. Symp. on Environmental Geotechnology*, Shanghai, **1**, 381-385 (1989).
151. Chang, K.-J., Toboada, A., Chan, Y.-C., & Dominguez, S. Post-seismic surface processes in the Jiufengershan landslide area, 1999 Chi-Chi earthquake epicentral zone, Taiwan. *Eng. Geol.* **86**, 102-117 (2006).
152. Chigira, M., Wang, W. N., Furuya, T., & Kamai, T. Geological causes and geomorphological precursors of the Tsaoling landslide triggered by the 1999 Chi-Chi earthquake, Taiwan. *Eng. Geol*. **68**, 259–273 (2003).
153. Cruden, D. M. & Lu, Z. Y. The rockslide and debris flow from Mount Cayley B. C., in June 1984. *Can. Geotech. J.* **29**, 614–626 (1992).
154. Geertsema, M., Hungr, O., Schwab, J. W., & Evans, S. G., A large rockslide-debris avalanche in cohesive soil at Pink Mountain, northeastern British Columbia, Canada. *Eng. Geol*. **83**, 64-75 (2006).
155. Hung, J. J., Lee, C. T., & Lin, M. L. Tsao-ling rockslides, Taiwan. in *Catastrophic Landslides: Effects, Occurrence, and Mechanisms* (ed Evans, S. G. and DeGraff, J. V.) *Rev. Eng. Geo.* **15**, 91-115 (Geological Society of America Boulder, Colorado, 2002).
156. Hungr, O. & Evans, S. Entrainment of debris in rock avalanches: An analysis of a long run-out mechanism. *Geol. Soc. Am. Bull*. **116**, 1240-1252 (2004).
157. Lu, Z. Y. & Cruden, D. M. Two debris flow modes on Mount Cayley, British Columbia. *Can. Geotech. J.* **33**, 123–139 (1996).
158. Melekestsev, I. V., Dirksen, O. V., & Girina, O. A. A giant landslide-explosion cirque and a debris avalanche at Bakening volcano, Kamchatka. *Volcanol. Seismol.* **20**, 265-280 (1999).
159. Noetzli, J., Huggel, C., Hoelzle, M., & Haeberli, W. GIS-based modelling of rock-ice avalanches from Alpine permafrost areas. *Comput. Geosci*. **10**, 161-178 (2006).
160. Ohmori, H. Morphological characteristics of the scar created by large-scale rapid mass movement, *Trans. Jpn. Geomorph. Union*, **13**, 185-202 (1992).
161. Read, S. A. L., Beetham, R. D., & Riley, P. B., Lake Waikaremoana—A large landslide dam in New Zealand. in *Landslides: Proceedings of 6th international Symposium on landslides, Christchurch, New Zealand*, (ed Bell, D. H.) 1481-1487 (Balkema, Rotterdam, 1992).
162. Shang, Y. *et al*. A super-large landslide in Tibet in 2000: background, occurrence, disaster, and origin. *Geomorphology* **54**, 225-243 (2003).
163. Siebert, L., Glicken, H., & Ui, T. Volcanic hazards from Bezymianny- and Bandai-type eruptions. *Bull. Volcanol*. **49**, 435-459 (1987).

164. Takarada, S., Ui, T. & Yamamoto, Y. Depositional features and transportation mechanism of valley-filling Iwasegawa and Kaida debris avalanches, *Japan. Bull. Volcanol.* **60**, 508-522 (1999).

165. Wen, B., Wang, S., Wang, E., & Zhang, J. Characteristics of rapid giant landslides in China. *Landslides* **1**, 247-261 (2004).

APPENDIX 2

Supplementary Figures

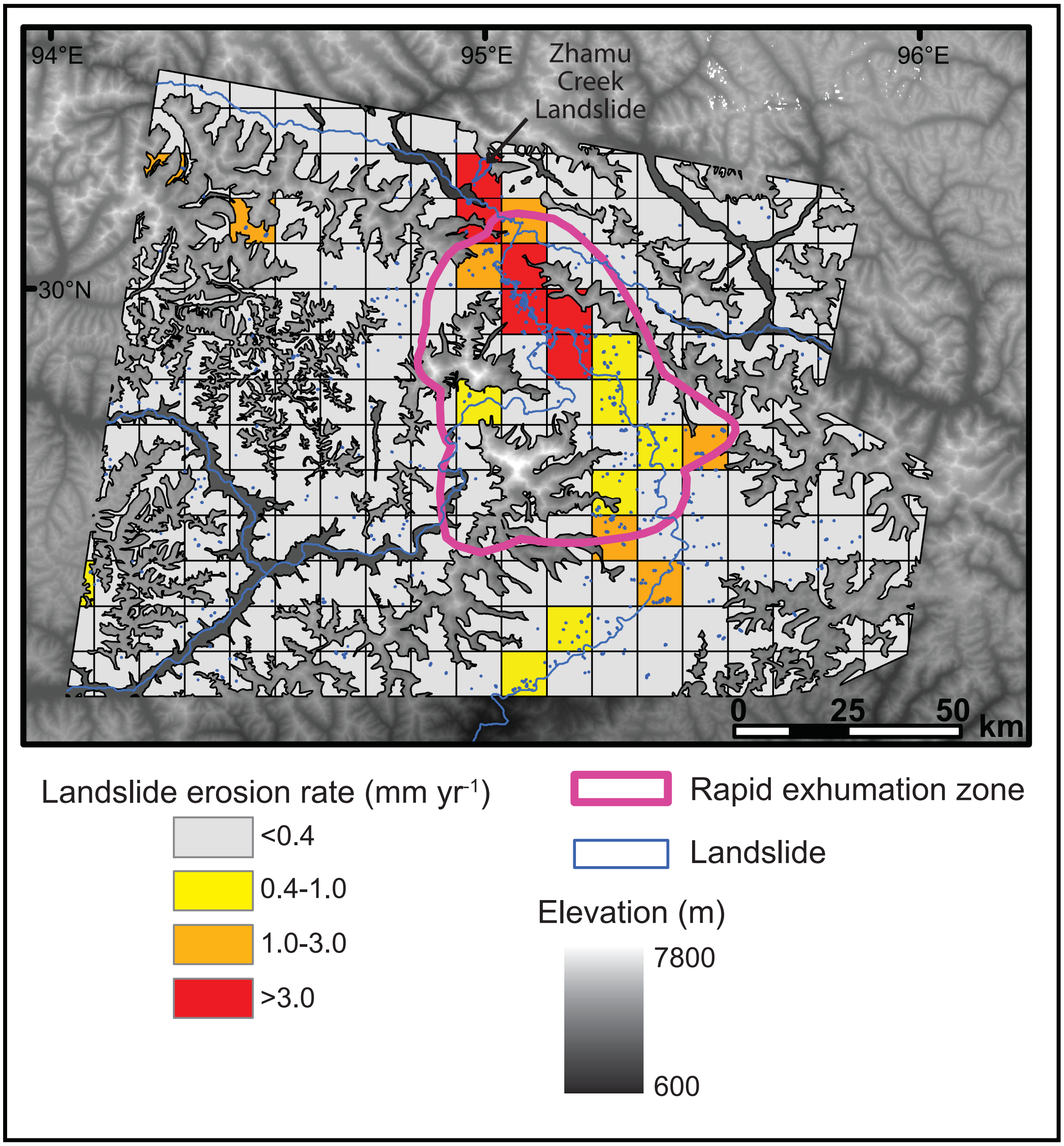

Figure A2.1. Landslide erosion rates for the 1974–2007 landslide inventory.

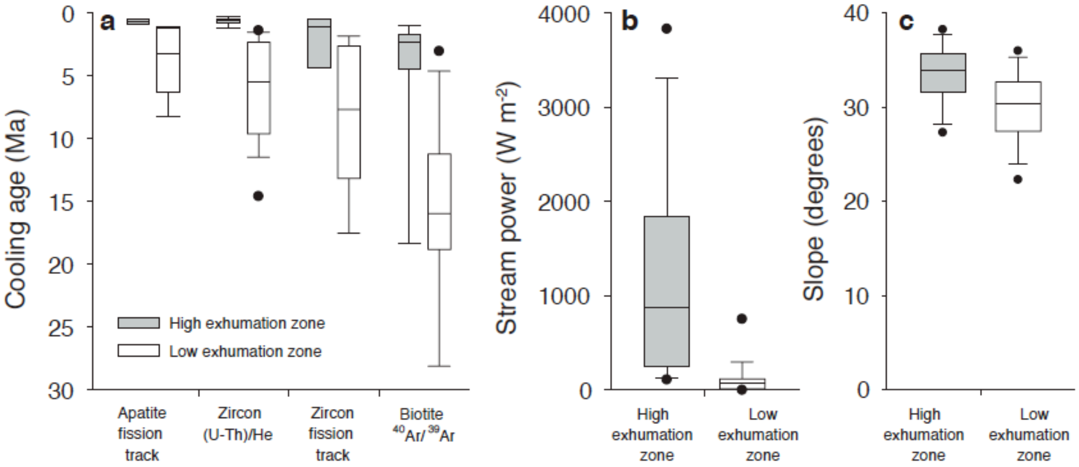

Figure A2.2. Mineral cooling age, stream power, and hillslope angle distributions for the high versus low exhumation zones. a, Mineral cooling ages[1–5]; b, stream power[3]; c, hillslope angle distributions of mean values for individual grid cells. The boxes span the inter-quartile range, the line denotes the median, whiskers denote 10th and 90th percentiles, and circles denote 5th and 95th percentiles. Each pair has significantly different medians or means ($p<0.02$; see Methods).

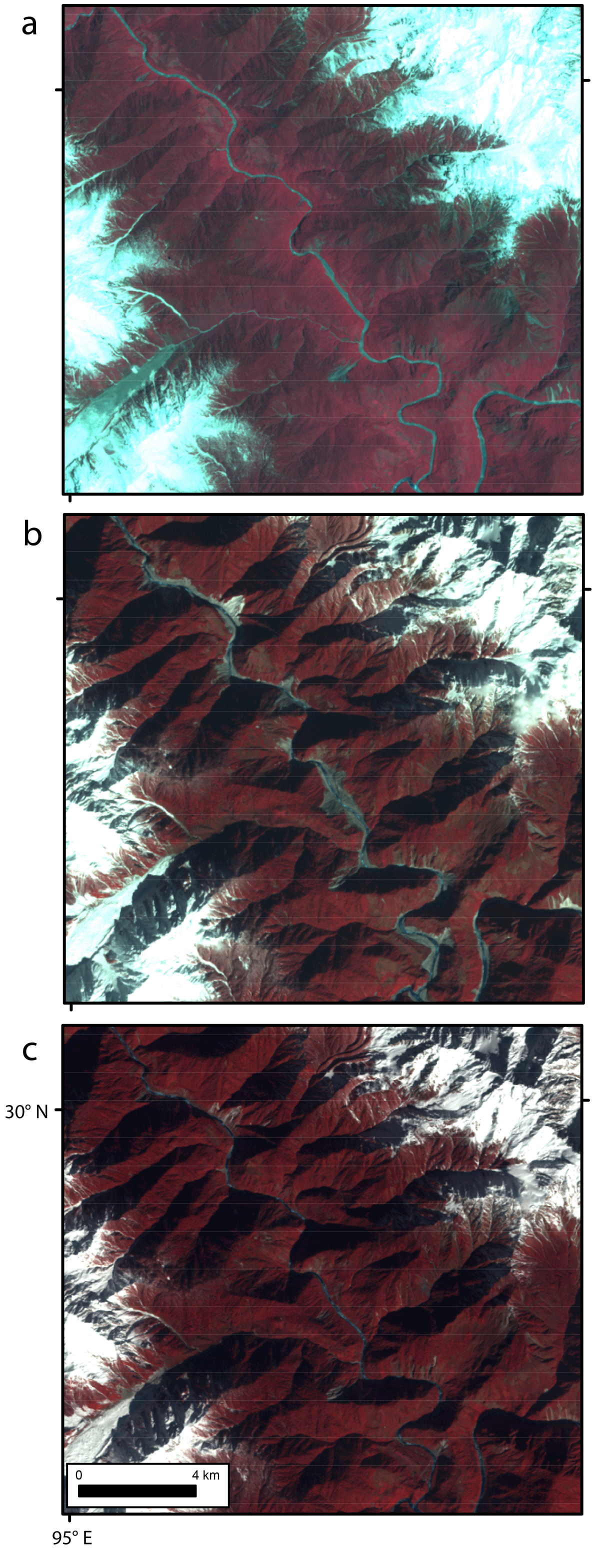

Figure A2.3. Vegetation recovery on landslide scars. LANDSAT images (30-m resolution) for a portion of the Tsangpo Gorge from (a) 4 May 2000 prior to the Zhamu Creek outburst flood, (b) 15 January 2001 approximately 6 months after the outburst flood, and (c) 16 January 2010. Note the number of landslides triggered by the 10 June 2000 outburst flood and the high degree of re-vegetation of the landslide scars during the subsequent decade. The confluence of the Po Tsangpo and Yarlung Tsangpo Rivers is at the bottom of the image.

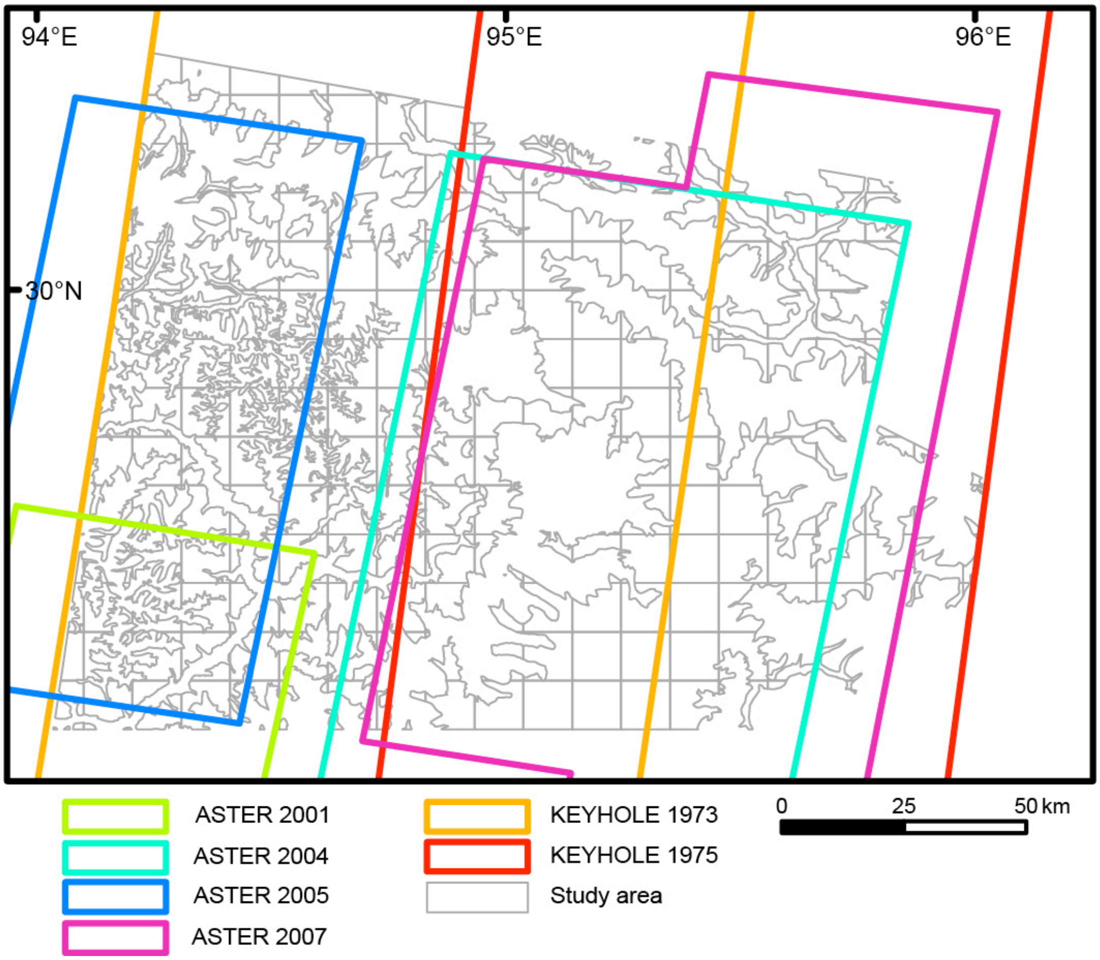

Figure A2.4. Satellite image index map. LANDSAT images from 2000 and 1990 covered the entire study area.

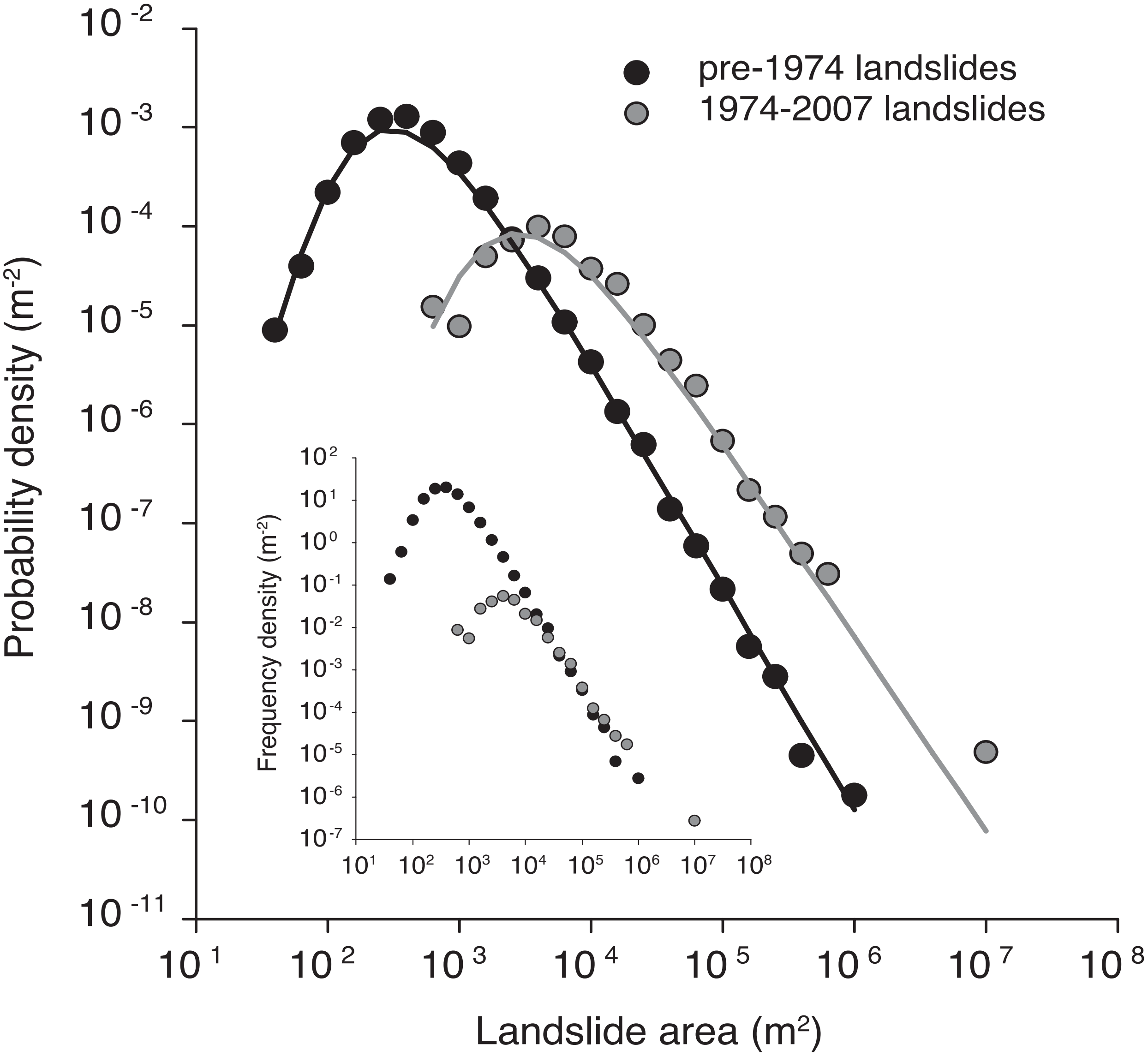

Figure A2.5. Landslide probability and frequency density as a function of landslide area. Probability density and frequency density (inset) data are for the pre-1974 and 1974–2007 landslide inventories and were calculated following ref. 7. The best-fit lines are three-parameter inverse-gamma distributions (eq. A2.2) with parameter values: $a = 768$ m^2, $\rho = 1.27$, and $s = –32.6$ m^2 for pre-1974 landslides and $\alpha = 6100$ m^2, $\rho = 0.96$, and $s = –311$ m^2 for 1974–2007 landslides. We attribute the difference in the landslide area at which the peak probability density occurs between the two inventories to the differences in image resolution.

Supplementary Tables

Table A2.1. Total landslide volume and erosion rate estimates based on summing volumes of individual landslides

Landslide inventory	Number of landslides	Volume-area-scaling relationship					
		α=0.26; γ=1.36		α=0.146; γ=1.332		$A_L<10^5 m^2$: α=0.224; γ=1.262 $A_L>10^5 m^2$: α=0.23; γ=1.41	
		Total landslide volume (m^3)	Landslide erosion rate (mm yr^{-1})	Total landslide volume (m^3)	Landslide erosion rate (mm yr^{-1})	Total landslide volume (m^3)	Landslide erosion rate (mm yr^{-1})
pre-1974*							
All landslides	15257	$1.86 \bullet 10^8$	0.56	$7.84 \bullet 10^7$	0.24	$1.46 \bullet 10^8$	0.44
High exhumation zone	4902	$9.00 \bullet 10^7$	1.55	$3.81 \bullet 10^7$	0.66	$6.09 \bullet 10^7$	1.05
Low exhumation zone	10355	$9.59 \bullet 10^7$	0.35	$4.03 \bullet 10^7$	0.15	$8.51 \bullet 10^7$	0.31
1974-2007							
All landslides	558	$8.07 \bullet 10^8$	1.72	$2.99 \bullet 10^8$	0.64	$1.42 \bullet 10^9$	3.03
High exhumation zone	253	$1.43 \bullet 10^8$	1.68	$5.77 \bullet 10^7$	0.68	$1.79 \bullet 10^8$	2.10
Low exhumation zone	305	$6.64 \bullet 10^8$	1.73	$2.42 \bullet 10^8$	0.63	$1.24 \bullet 10^9$	3.24
All without flood-induced landslides	517	$7.07 \bullet 10^8$	1.51	$2.60 \bullet 10^8$	0.56	$1.27 \bullet 10^9$	2.71
High exhumation zone without flood induced landslides	212	$4.34 \bullet 10^7$	0.51	$1.80 \bullet 10^7$	0.21	$2.83 \bullet 10^7$	0.33
All landslides without Zhamu Creek landslide	557	$1.97 \bullet 10^8$	0.42	$7.97 \bullet 10^7$	0.17	$2.27 \bullet 10^8$	0.49
Low exhumation zone without Zhamu Creek landslide	304	$5.36 \bullet 10^7$	0.14	$2.20 \bullet 10^7$	0.057	$4.75 \bullet 10^7$	0.12

The respective areas for the pre-1974 high and low exhumation zones are $1.93 \bullet 10^9$ m^2 and $9.18 \bullet 10^9$ m^2. The respective areas for the 1974-2007 high and low exhumation zones are $2.58 \bullet 10^9$ m^2 and $1.16 \bullet 10^{10}$ m^2. The total area is the sum of the high and low exhumation zone areas. The differences in area are due to variation in snow and ice cover on images. *Pre-1974 landslide erosion rates are averaged over a 30-yr period.

Table A2.2. Inverse gamma fitting parameters

Landslide Inventory	Inverse-gamma distribution parameters		
	a (m^2)	ρ	*s* (m^2)
<u>pre-1974</u>			
All landslides	768	1.27	-32.6
High exhumation zone	986	1.23	-58.4
Low exhumation zone	707	1.32	-26.7
<u>1974-2007</u>			
All landslides	6100	0.96	-311
High exhumation zone	8723	0.82	-1055
Low exhumation zone	5047	0.83	-151

Table A2.3. Erosion rate estimates based on integration of landslide volume-frequency distributions

Landslide inventory	Erosion rates (mm yr^{-1}) for different volume-area scaling parameters		
	$\alpha=0.26$; $\gamma=1.36$	$\alpha=0.146$; $\gamma=1.332$	$A_L<10^5 m^2$: $\alpha=0.224$; $\gamma=1.262$ $A_L>10^5 m^2$: $\alpha=0.23$; $\gamma=1.41$
<u>pre-1974</u>			
All landslides	1.56	0.60	1.95
High exhumation zone	4.82	1.82	6.29
Low exhumation zone	0.86	0.33	0.98
<u>1974-2007</u>			
All landslides	1.86	0.68	3.14
High exhumation zone	12.1	4.34	21.4
Low exhumation zone	2.06	0.74	3.62

Mean landslide volumes were calculated by eq. S3 and multiplied by the total number of landslides (Table S1) to calculate the total landslide volume. The total landslide volume was divided by the drainage area to determine the mean depth of erosion. The pre-1973 erosion depth was averaged over 30 yrs and the 1974-2007 erosion depth was averaged over 33 yrs.

Supplementary Methods

The spatial patterns of landslide erosion rates we determine for the eastern Himalaya (Figure 2.1d, Figure A2.1) are based on the spatial distribution of mapped landslide areas. The spatial patterns are hence robust, but the absolute magnitude of the erosion rates depend on the method used to calculate the volume of individual landslides. The images we used to map landslides cover only a short time period. Hence it is probable that infrequent, but large and volumetrically important landslides are missing from our landslide inventory, leading to underestimation of erosion rates. Additionally, in the case of the pre-1974 landslide inventory, the erosion rates also depend on time period over which the landslides occurred.

To assess the sensitivity of landslide erosion rates to volume-area scaling parameters, we estimated the volume of individual landslides using three different landslide volume-area scaling relationships and compared the landslide erosion rates estimated by each scaling relationship. We also determined landslide erosion rates by integrating synthetic volume-frequency distributions in order to develop more robust erosion estimates that accounts for the large, infrequent landslides that may not have been captured by our empirical inventories.

Determining erosion rates by integration of volume-frequency distributions requires that the shape of the landslide probability density distribution be known. Hence, this technique was applied to large areas (entire study area; high and low exhumation zones) where there were a sufficient number of mapped landslides to define the probability density distribution. The erosion rates calculated by determining the volumes of individual landslides and the erosion rates determined by integration of volume-frequency distributions provide different, but complimentary information. Calculating the volumes of individual landslides allows the spatial pattern of landslide erosion to be determined, whereas integration of volume-frequency distributions provides more robust estimates of landslide erosion magnitude, but without detailed spatial resolution.

We estimated landslide volume using a volume-area scaling relationship with the form:

$$V = \alpha A^{\gamma} \qquad \text{(eq. A2.1)}$$

where V is landslide volume (m^3), A is landslide area (m^2), and α (m$^{(3-2\gamma)}$) and γ are power-law scaling parameters. Three sets of α and γ values were used to calculate landslide volumes (Table A2.1). The volume-area scaling parameters α=0.26 and γ=1.36 are based on data from 428 measurements of soil and bedrock landslides from the Himalaya[6]; the erosion rates shown in Figures 2.1-2.5 and Figure A2.1 are based on these parameters. The second set of volume-area scaling parameters with α=0.146 and γ=1.332 are based on a global data set of 4231 landslide measurements[6]. The third landslide volume estimates are based on volume-area scaling parameters α=0.224 and γ=1.262 for landslides with areas <10^5 m^2 and α=0.23 and γ=1.41 for landslides with areas >10^5 m^2, based on the assumption that landslides with areas <10^5 m^2 are predominantly soil landslides and landslides with areas >10^5 m^2 are predominantly bedrock landslides[6].

Landslide frequency-area distributions (Figure A2.5) were fit with a three-parameter inverse-gamma distribution[7] with the form:

$$p(A) = \frac{1}{a\Gamma(\rho)}\left[\frac{a}{A-s}\right]^{\rho+1} \exp\left[-\frac{a}{A-s}\right] \qquad \text{(eq. A2.2)}$$

where $p(A)$ is the probability density of landslide areas (A), a, ρ, and s are empirical parameters (Table A2.2) and Γ(ρ) is the gamma function of ρ. Following ref. 7, we numerically solved for the mean landslide volume ($\overline{V}$) for synthetic landslide inventories using the appropriate a, ρ, and s-values for each inventory and varying α and γ values via:

$$\overline{V} = \alpha \int_{A\,\min}^{A\,\max} A^{\gamma} p(A) dA \qquad \text{(eq. A2.3)}$$

by substituting eq. A2.2 for $p(A)$. The smallest landslide area ($A_{\min}$) was set to 100 m^2. The largest mapped landslide was the Zhamu Creek landslide, which had an area of nearly $8 \cdot 10^6$ m^2. Hence we assumed the largest landslide area ($A_{\max}$) that could occur in our study area was 10^7 m^2. The total landslide volume was determined by multiplying the mean landslide volume by the total number of landslides in each inventory.

To convert the total landslide volumes for the pre-1974 landslide inventory to erosion rates, we assume that the landslides occurred over a 30-year period but acknowledge the time period may be longer or shorter (i.e., Figure 3.1d). The similarities in the power-law tail of the frequency density relationships for the pre-1974 and 1974–2007 landslide inventories (Figure A2.5, inset) suggests the inventories have a similar number of landslides[7]. The 1974–2007 landslides occurred over a 33-yr period, and if landslide frequency is roughly constant, then our 30-year estimate for the pre-1974 inventory is consistent with the frequency density data. The rapid revegetation of landslide scars (Figure A2.3) also indicates that landslides are detectable for only a few decades after they occur. Landslides in the Southern Alps of New Zealand are visible of air photos for about 20 yr after they occur[8], which is consistent with our estimate for the eastern Himalaya.

Supplementary Results

Total landslide volumes calculated by summing the volumes of individual landslides vary based on the volume-area scaling parameters used to estimate landslide volumes (Table A2.1). For the pre-1974 landslide inventory, the highest erosion rates are about 2.3 times greater than the lowest rates. The highest erosion rate estimates for the 1974-2007 landslide inventory are about 2.5 to 5 times greater than the lowest values. The variability in erosion rates determined via volume-frequency integration was similar, as the highest erosion estimates were of 2 to 5 times greater than the lowest estimates (Table A2.2).

The total landslide volumes calculated via integration of the landslide volume-frequency distributions are generally higher than those calculated by summing the volume of individual landslides. For the pre-1974 landslide inventory the erosion rate estimates for the high exhumation zone range from 1.82–6.29 mm yr^{-1}, depending on the volume-area scaling parameters. Erosion rates in the low exhumation zone were lower, ranging from 0.33–0.98 mm yr^{-1}. Landslide erosion rates for the 1974–2007 inventory were 4.34–21.4 mm yr^{-1} for the high exhumation zone and 0.74–3.62 mm yr^{-1} for the low exhumation zone. The higher landslide erosion rates for the 1974–2007 inventory, relative to the pre-1974 inventory, is expected, given that the flood-triggered landslides and the Zhamu Creek landslide cause the frequency-area distribution of the 1974–2007 inventory to have a heavier power-law tail (p) than the pre-1974 distribution.

Supplementary Discussion

Uncertainty in landslide volume-area scaling parameters leads to variability in the magnitude of landslide erosion estimates, but the variability in erosion rates is generally less than a factor of five for the volume-area scaling parameters we deem most appropriate for the eastern Himalaya. Additionally, the variability introduced by uncertainty in volume-area scaling parameters has little influence on the spatial pattern of landslide erosion. Since we tested the threshold hillslope model by quantifying the spatial pattern of landslide erosion with respect to exhumation rates, stream power, and hillslope angles, the degree of uncertainty in landslide volumes and erosion rates does not alter our conclusions regarding spatial coupling of landslide erosion with river incision and exhumation rates. Accounting for potential 'missing' landslides via integration of volume-frequency distributions yields erosion rates that are in agreement with long-term exhumation rates calculated using thermochronolgy, supporting our conclusion that landslide erosion on threshold hillslopes drive the rapid exhumation rates observed in the eastern Himalaya.

Supplementary References

1. Burg, J. *et al.* Exhumation during crustal folding in the Namche-Barwa syntaxis. *Terra Nova* **9**, 53-56 (1997).
2. Burg, J. *et al.* The Namche Barwa syntaxis: evidence for exhumation related to compressional crustal folding. *Journal of Asian Earth Sciences* **16**, 239-252 (1998).
3. Finnegan, N. *et al.* Coupling of rock uplift and river incision in the Namche Barwa-Gyala Peri massif, Tibet. *Geological Society of America Bulletin* **120**, 142-155 (2008).
4. Seward, D. & Burg, J. Growth of the Namche Barwa Syntaxis and associated evolution of the Tsangpo Gorge: Constraints from structural and thermochronological data. *Tectonophysics* **451**, 282-289 (2008).
5. Stewart, R. *et al.* Brahmaputra sediment flux dominated by highly localized rapid erosion from the easternmost Himalaya. *Geology* **36**, 711-714 (2008).
6. Larsen, I., Montgomery, D. & Korup, O. Landslide erosion controlled by hillslope material. *Nature Geoscience* **3**, 247-251 (2010).
7. Malamud, B., Turcotte, D., Guzzetti, F. & Reichenbach, P. Landslide inventories and their statistical properties. *Earth Surface Processes and Landforms* **29**, 687-711 (2004).
8. Hovius, N., Stark, C. & Allen, P. Sediment flux from a mountain belt derived by landslide mapping. *Geology* **25**, 231-234 (1997).

APPENDIX 3

Supplementary Methods

Soil, bedrock, and sediment sampling

We sampled soil from five ridges in the western Southern Alps (Fig. A3.3, A3.4). In order to avoid sampling material that had been extensively transported, *in-situ* soils were collected from the main ridge or from local-scale convexities on smaller divides emanating from the main ridge, rather than downslope locations. The morphology and horizon development of each soil was described prior to sampling. We discarded organic-rich O-horizon materials and collected material generally from the entire soil column; from the top of the A-horizon to parent material. The depth to bedrock (mineral soil thickness) was measured at each site. Soil bulk density was estimated using the compliant cavity method[1]. Local slope at each site was measured with a clinometer. Bedrock was sampled from the lowermost depth of each soil pit, which reached into fractured rock, as well as from the nearest outcrop to each pit. At one soil pit (Alex Knob Pit 4) we collected soil in 10 cm thick increments, which correspond closely to the soil horizons at the site (Fig. A3.5). We collected one sample from a bedrock outcrop in the Karangarua catchment. We also collected sand-sized river sediment from sandbars and channel margin deposits.

Sample processing and analysis

All samples were wet sieved to isolate the 250–850 µm grain-size fraction. The 250850 µm grain-size fraction of each sample was treated with warm HCl for 24 h, followed by treatment with a combination of warm NaOH and H_2O_2 for 24 h; both treatments were then repeated. Selective dissolution in 2% HF was used to isolate quartz. Refractory heavy minerals were removed using lithium heteropolytungstate (LST) heavy liquid. A surfactant was used to aid removal of muscovite and feldspar. Samples were boiled in NaOH prior to the final HF etch. ^{9}Be carrier was added to quartz aliquots prior to dissolution and Be separation at the University of Washington Cosmogenic Isotope Laboratory[2,3]. BeO was packed into cathodes with Nb powder and ^{10}Be/^{9}Be ratios were measured via accelerator mass spectrometry (AMS) at Lawrence Livermore National Laboratory.

Splits of each bulk soil sample (generally ~1 kg) were crushed and pulverized. Zirconium (Zr) concentrations were measured on sub-splits of the pulverized material. Loss-on-ignition (LOI) was also measured for sub-splits and soil Zr concentrations were corrected for LOI. Surfaces of bedrock samples were cut or ground off to remove potentially weathered joint or foliation surfaces prior to Zr measurement. Bedrock density was measured following the removal of joint surfaces by weighing samples in air and in water. All Zr measurements were made via x-ray fluorescence on pressed powder samples at ALS Minerals, Vancouver, Canada. We generally calculated the chemical depletion fraction (CDF)[4,5] using the bedrock collected from the base of each pit, rather than bedrock collected from outcrops, because preliminary measurements of the outcrop samples suggested Zr concentrations were spatially variable, which has been observed in other studies[6]. However, the Gunn Pit 4 and Gunn Pit 6 rock samples from the base of the soil pits had higher Zr concentrations than the soil, so we used Zr concentrations in bedrock from outcrops to calculate the CDF for those sites. Bedrock weathering beneath the soil would lead to the interpretation that the CDF are minimum values, but high bedrock density values suggest very little mass loss due to incipient saprolite formation (Table A3.1).

Interpretation of ^{10}Be concentrations

Vertical mixing

The ^{10}Be concentration in quartz grains within a soil provides an estimate of the total denudation rate (soil production rate) at that site, provided the soil is vertically well-mixed[7,8]. We tested the assumption of well-mixed soil with the Alex Knob Pit 4 samples. The soil ^{10}Be concentrations for different depth intervals indicate the soil is well-mixed (Fig. A3.5). Few studies have evaluated whether soils are vertically-well mixed, but the results are consistent with those expected from bioturbation, as observed in other landscapes[9–11].

Isotopic steady-state

Interpretation of ^{10}Be concentrations in soil and sediment as denudation rates requires the assumption of isotopic steady-state, such that the in-going and out-going ^{10}Be flux from a soil profile or watershed is constant over time[7,9,12,13]. Landslides, which are common in the western Southern Alps[14], have the potential to upset the ^{10}Be balance at both the soil profile and watershed scales. For example, sampling a surface immediately after a landslide removed 1 m of rock would cause erosion rates to be over-estimated by about a factor of three[15]. Given the rapid denudation rates in the western Southern Alps, it is not feasible to use a second nuclide, such as ^{26}Al, to test the isotopic steady-state assumption[13], so we carefully selected sampling sites in order to minimize the likelihood of violating the steady-state assumption.

At the soil profile scale, landslides can expose bedrock shielded from cosmic rays, resulting in low ^{10}Be concentrations that are out of equilibrium with long term soil production rates[13,15]. Measuring ^{10}Be concentrations in soils formed on recent landslide scars would result in over-estimation of soil production rates. The time (t) required to return to isotopic equilibrium declines with increasing denudation rate following:

$$t = \frac{\Lambda}{\rho \cdot D} \qquad \text{(eq. A3.1)}$$

where Λ is the attenuation length for ^{10}Be production below the surface (160 g cm^{-2}), ρ is rock density, (2.65 g cm^{-3}) and D is the denudation rate (cm yr^{-1}) (ref. 13). For example, for a soil production rate of 2 mm yr^{-1}, isotopic equilibrium will be re-established 300 yr following a landslide.

We carefully selected sampling sites to avoid areas with evidence of landsliding. We limited our sampling to convex ridgetops (Fig. A3.3, A3.4) where chronic, biogenic disturbance-driven geomorphic processes dominate[16] and avoided planar, threshold hillslopes where episodic landslides are the dominant erosion mechanism[17]. Previous work on spatial patterns of vegetation and soils in the western Southern Alps indicates ridges are the most stable portions of the landscape with respect to disturbance by landsliding[18,19]. While in the field we did not observe scars of any recent landslides that breached topographic divides and lowered ridgetop elevations, although we did observe recent landslide scars downslope from ridges. The landslides we did observe resulted in distinct topographic depressions, as even “shallow” landslides erode into bedrock, given the dm-scale soil depths in the western Southern Alps. We observed no similar topographic depressions on the ridgetops we sampled, indicating that the landslide return interval for ridgetops is likely to be much longer than those reported for the landscape as a whole. The mean time between landslides (return interval) for a given point on the landscape in the western Southern Alps has been estimated to be both 2,100–15,000 yr (ref. 20) and ~300 years (ref. 21). Note that the different landslide return intervals are based on the same landslide mapping data[14], but the authors make different assumptions about the continuity (or dis-continuity) of landslide area-frequency distributions; the 2,100–15,000 yr estimate is based directly on the mapped landslide distribution. It is worth noting that both landslide return interval estimates (which likely overestimate landslide frequency on ridgetops) are sufficiently long that ^{10}Be equilibrium can be re-established between landslides for the high soil production rates we measure. In the case where earthquakes on the Alpine Fault caused co-seismic shaking and ridgetop landsliding, as observed following the Chi-Chi earthquake in Taiwan[22], a soil production rate of 2 mm yr^{-1} would be sufficiently rapid to establish a new ^{10}Be equilibrium in the time interval since the most recent (M_W>7.6; 1717 A.D.) earthquake[23]. Moreover, none of our ^{10}Be concentrations are consistent with coseismic landsliding during the most recent Alpine Fault rupture—the apparent exposure ages are too old (Table A3.2). If the soil ^{10}Be data were alternatively interpreted as soil exposure ages that yield information on the time since the last landslide, a soil production rate can be determined by dividing the soil depth by the soil age. For this method to yield true soil production rates, it must be assumed that no erosion of soils formed *in-situ* on the landslide scar has occurred. Such an approach would yield lower soil production rates than those calculated by interpreting the ^{10}Be data as steady-state soil production rates. However, given the steep slope gradients at most of our sampling sites (Table A3.3), the assumption of no erosion is implausible, hence interpreting soil ^{10}Be concentrations as exposure ages would underestimate soil production rates.

Tree throw is an episodic driver of soil production[24,25] that could also cause ^{10}Be concentrations to be out of steady-state. We explored the potential influence of tree throw on soil production rates with a model similar to those developed to assess potential errors in denudation rates caused by sampling bedrock surfaces following spallation of a slab of rock[15,26]. Here we assume that tree throw removes rock from the soil-bedrock interface in a manner analogous to episodic erosion of an outcrop and track the ^{10}Be concentration at the soil-bedrock interface. The model does not simulate mixing of detached material with overlying soil and we assume our results reflect maximum estimates of potential errors, as incorporation of rock transported by tree-throw into a well-mixed regolith would provide additional buffering that minimizes temporal variation of ^{10}Be concentrations in soil. The model also assumes that all denudation is due to physical erosion, which also requires interpreting the error estimates as maximum values. The model uses a finite-difference approach with an annual time-step; the initial condition is a steady state erosion rate, after which erosion becomes unsteady, with periods of no erosion punctuated by periodic removal of a rock slab with a specified thickness. We modeled soil production rate scenarios of 1 mm yr^{-1} and a 2.5 mm yr^{-1}, as we were most concerned with potential over-estimation of higher soil production rates. There are two 1 mm yr^{-1} cases, one in which 100 mm of rock is removed once per century and one in which 300 mm is removed once every 300 yr. There are also two 2.5 mm yr^{-1} cases, one in which 250 mm is eroded once per century and one in which 750 mm is removed once every three centuries.

The modeling results show that, after reaching steady-state, the range of erosion rates interpreted from ^{10}Be in the 1 mm yr^{-1} scenario is 0.93–1.09 mm yr^{-1} for the case in which all the erosion occurs once per century and 0.79–1.29 mm yr^{-1} for the case in which all the erosion occurs once every three centuries (Figure A3.6). One of our measured soil production rates is 1.00±0.077 mm yr^{-1} and the true uncertainty is likely greater due to uncertainty in ^{10}Be production rate scaling[27,28]. Hence uncertainty in soil production rates predicted by our 1 mm yr^{-1} un-steady erosion rate models is of comparable magnitude to analytical and production rate uncertainty.

The range of erosion rates interpreted from ^{10}Be in the 2.5 mm yr^{-1} scenarios are 2.05–3.11 mm yr^{-1} for the case in which all the erosion occurs once per century, which is nearly identical to the uncertainty in one of our measured values of the same magnitude (2.48±0.51 mm yr^{-1}). The range of inferred erosion rates for the 2.5 mm yr^{-1} scenario in which all erosion occurs every 300 years is 1.43 to 4.94 mm yr^{-1} (Figure A3.6). The magnitude of the erosion (750 mm) is unrealistically high for a single tree fall event, especially given that shrubs are the dominant vegetation at the ridgetops we sampled. Hence, the potential error modeled by this scenario is more representative of error caused by shallow landsliding, which we minimized with our sampling scheme, as described above.

Additionally, whereas the soil production rates we measure in the western Southern Alps are substantially higher than those determined elsewhere using *in situ*-produced ^{10}Be, they are consistent with values estimated using other methods. For example, meteoric ^{10}Be has been used to infer a soil production function in with a y-intercept of 2.1 mm yr^{-1} for very weak shale bedrock[29]. Similarly, soil on man-made bedrock exposures has been shown to form at rates of 5–10 mm yr^{-1} (given the volume change associated with rock-soil conversion, the equivalent bedrock lowering rates would be about half these values) on sandstone and shale bedrock[30]. These two examples highlight the role weak lithology plays in driving rapid soil production rates, and we expect climate and biotic activity to play similar roles in driving high soil production rates in the western Southern Alps.

At the catchment scale, landslides stochastically deliver sediment to channels. The ^{10}Be concentration in landslide-derived sediment varies with landslide depth. Unless sediment is sufficiently well-mixed such that ^{10}Be concentration in sediment transported past the sediment sampling point is steady, the ^{10}Be concentrations will not accurately represent the true denudation rate[31,32]. The catchment scale at which ^{10}Be in sediment can be used reliably to infer the denudation rates of the upstream watershed has been modeled to be on the order of 70–100 km^2 (ref. 31, 32). The large catchments we sampled that drain from the Main Divide to the Alpine Fault have areas of 340-450 km^2, which are sufficiently large to expect steady ^{10}Be flux. ^{10}Be disequilibrium is expected to be more likely at small catchment areas, typically resulting in overestimation of denudation rates[31]. Denudation rates for the two small (1.6 km^2; 12.6 km^2) catchments nested within larger catchments are within 1σ error or lower than denudation rates for the larger catchments, and hence do not exhibit evidence of isotopic disequilibrium. The lack of disequilibrium is likely due to the high rates of landsliding in the western Southern Alps, as rivers are always transporting sediment derived from a range of landslide depths. Though it is not evidence of erosional steady state, we do note that the catchment-scale denudation rates are generally consistent with erosion and exhumation rates averaged over a range of timescales[14].

CRONUS calculator inputs and denudation rate calculations

We used the CRONUS calculator[33] to calculate denudation rates (Table A3.1, A3.2) from our ^{10}Be concentrations. To maintain consistency with other studies, we use the ^{10}Be production rate calibration data encoded in the CRONUS calculator[33], which are from a wide-range of global sites, in determining denudation rates. More recent calibration efforts from the eastern Southern Alps of New Zealand[28] has resulted in a ^{10}Be production rate estimate that is ~14% lower than those in the version of the CRONUS calculator we used (Wrapper script v.2.2; Main calculator v.2.1; Objective function v.2; Constants v.2.2.1; Muons v.1.1). Adopting the more proximal calibration data would result in roughly a 14% reduction in the denudation rates we report. Because ^{10}Be production rate calibration schemes will continue to be improved upon, we report our results and the data required to reproduce our denudation rates in Tables A3.1–A3.6. The 1-standard error uncertainties in the denudation rates calculated using the CRONUS calculator include errors in the number of ^{9}Be atoms added to each sample, errors in the ^{10}Be concentration of procedural and carrier blanks, and errors in the AMS isotope ratio measurements, added in quadrature.

We calculated catchment-averaged ^{10}Be production rate scaling factors by determining production rates for each grid cell in a DEM, using the elevation and latitude of each grid cell, as described by Greg Balco (http://depts.washington.edu/cosmolab/P_by_GIS.html). We used production rate scaling factors to calculate the elevation input for the CRONUS calculator, using the mean catchment latitude and Lal's polynomial ^{10}Be production rate scaling scheme[13]. The catchment-averaged production rates we use assume zero ^{10}Be production for the portions of each catchment with ice and permanent snow cover (11%, 13%, and 4% of the Karangarua, Whataroa, and Hokitika catchments, respectively), using 1:50,000 scale data from Land Information New Zealand (http://data.linz.govt.nz/layer/352-nz-mainland-snow-polygons-topo-150k/). The thickness of all soil and sediment samples was set to an arbitrarily low value of 0.1 cm, as the ^{10}Be concentration at the surface is the relevant value for determining denudation rates in both vertically-mixed soils and sediment[7]. The density values are mean values from multiple bedrock samples from each soil pit; catchment bedrock density values are the mean value of all soil pit samples within the watershed.

Topographic shielding of soil pits was calculated based on the hillslope angle of the sample site. The thick vegetation in the western Southern Alps generally blocked our view of the horizon, so we did not collect data for determining a shielding correction due to distant topography. Given our samples were from ridgetops, distant topography is expected to cause little shielding. We were able to climb on top of the single bedrock outcrop we sampled, which did afford a view of the horizon. The shielding factor determined for distant topography at this site is extremely small (0.999), indicating that by neglecting to account for shielding from distant topography, we are introducing very small errors that are orders of magnitude lower than the AMS measurement uncertainty. We calculated catchment-scale topographic shielding factors by first assuming that cosmic rays are conserved, such that all cosmic rays that enter a catchment produce ^{10}Be within the catchment. We then assumed that all cosmic rays entering a catchment pass through a plane that projects from the catchment outlet to the maximum catchment elevation. The angle of the catchment surface plane was then used to determine catchment scale shielding factors in a manner analogous to determining the shielding factor for a sample on a sloping surface[34]. The denudation rates we report in Tables A3.2 and A3.4 are based on time-dependent ^{10}Be production and the Lal[13]-Stone[35] latitude and altitude scaling scheme.

Quartz is resistant to dissolution; hence the mean residence time for quartz in soils is longer than the mean residence time of all minerals[36]. The enrichment of quartz biases denudation rate estimates[37]. We corrected our soil denudation rate measurements for quartz enrichment by assuming Zr is similarly enriched in our samples[37,38]. The correction factors are generally small, with an average of 1.06 (Table A3.5). For all corrections we assume a soil density of 1.0 g cm^{-1} (approximately the mean of the measured values) and an attenuation length of 160 g cm^{-2} (Table A3.3).

Soil and bedrock Zr concentrations were also used to determine chemical depletion fractions (CDF), where:

$$CDF = \left(1 - \frac{[Zr]_{rock}}{[Zr]_{soil}}\right) \qquad \text{(eq. A3.2)}$$

which is equivalent to the ratio of chemical denudation to total denudation[4,5]. Hence chemical denudation (W) can be determined:

$$W = D \cdot \left(1 - \frac{[Zr]_{rock}}{[Zr]_{soil}}\right) \qquad \text{(eq. A3.3)}$$

where D is the soil production or total denudation rate. Since:

$$D = W + E \qquad \text{(eq. A3.4)}$$

and *E* is the physical denudation rate, *E* can be determined from *D* and *W*. Errors in *D* are propagated in calculating *W* and *E*. Bedrock Zr was measured in a composite sample consisting of one or more pieces of bedrock from the base of each pit. Similarly, soil Zr was measured in a split of a large, homogenized sample that included rock fragments; hence we assume these data represent mean Zr concentrations. Because measurement errors in the Zr data are small (±2 ppm) relative to the concentrations we measure (Table A3.3), and are not expected to vary among samples, we did not propagate Zr measurement error in our calculations of *W*.

Global soil production functions, physical denudation, and chemical denudation data

The soil production functions in Fig. 4.3b are compiled from references 39–47. The soil production functions are as originally published; for example, no corrections have been made for updates of ^{10}Be production rate scaling.

The soil physical and chemical denudation rate data in Fig. 4.4 are compiled from references 5, 6, 48-52. The physical and chemical denudation data are as originally published, except some of those from ref. 5, which have been re-calculated using chemical erosion factors reported in ref. 38. The catchment-based physical and chemical denudation rate data are for 299 ocean-draining rivers from ref. 53. Pre-dam denudation data were used when these data were reported and data from five rivers (Colorado, Haihe, Rhine, Patuxent, and Severn) in the database were excluded from the statistical analyses due to high anthropogenic influence on either chemical or physical denudation. Removal of these data resulted in an increase in the chemical-physical denudation R^2 value, but had very little influence on the power-law scaling exponent. The chemical denudation data from the western Southern Alps are from refs. 54 and 55, whereas the physical denudation data are updated values from ref. 56. Data are shown only for rivers with measurements; no extrapolated values are shown.

Modeling global erosion and weathering

Slope gradient was calculated for Earth's terrestrial surface (excluding Greenland and Antarctica) using a 3 arc-second DEM from viewfinderpanorama.org, which is based primarily on the Shuttle Radar Topography Mission DEM, but with high latitudes and data gaps filled with elevation data from topographic maps. To properly represent slope at high latitude, slopes were calculated by accounting for variation in grid cell width as a function of latitude; grid cell widths were set to a single value for latitudinal bands that spanned 1° and grid cell width was varied for each 1° band. The 3 arc-second slope values were averaged to a grid of 15 arc-second cells prior to calculating the mean local (focal mean) slope using a square 5 km by 5 km moving window. Aggregating the slope data to 15 arc-seconds was done for computational efficiency in determining the focal mean, but it does not alter the value of the focal mean relative to the 3 arc-second data (i.e., for a 5 km by 5 km area, the mean of the 3-arc second slopes is the same as the mean of the 15 arc-second slopes because the values of the 15 arc-second slopes are the means of the 3 arc-second slope data).

Denudation rates (D, mm per 1000 yr) were calculated using an empirical relationship based on 990 catchment scale ^{10}Be denudation rate measurements:

$$D = 11.9e^{0.0065S} \qquad \text{(eq. A3.5)}$$

where slope (S, m km^{-1}) is the mean catchment slope determined from the 3 arc-second SRTM DEM (ref. 57). Following ref. 57, global slope gradients were determined using a 5 km by 5 km moving window so that slope values used to model global denudation were averaged over a spatial domain comparable to catchment averaged slopes. Denudation rates modeled with eq. A3.5 are unreasonably high for very steep slopes, so we set the maximum denudation rate to 10 mm yr^{-1}. The World Wildlife Fund global lakes and wetlands dataset (http://worldwildlife.org/pages/global-lakes-and-wetlands-database) was used to exclude lakes with surface areas >50 km^2 and reservoirs with >0.5 km^3 storage capacity from the analysis (GLWD-1 data), as these areas are not denuding. Denudation rates were also modeled after excluding endorheic catchments (in addition to lakes), using watershed data from the United Nations Food and Agriculture Organization (http://www.fao.org/geonetwork/srv/en/metadata.show?id=38047). The 3 arc-second DEM was re-sampled to 30 arc-seconds and D was calculated following the same methods for the 3 arc-second data, but without aggregating slopes.

Chemical denudation rates were calculated from the total denudation rates for both 3 and 30 arc-second data using empirical *W-D* relationships for global soil and river data (Fig. A3.7). Global soil and river data exhibit the following *W-D* relationships:

$$W_{soil} = 0.35 \bullet D_{soil} \qquad \text{(eq. A3.6)}$$

$$W_{river} = 0.71 \bullet D_{river}^{0.81} \qquad \text{(eq. A3.7)}$$

hence we generated two estimates of global chemical denudation rates—one using eq. A3.6 and one with eq. 7. Equation A3.6 is based only on the global soil chemical denudation rate values that exceed 10 Mg km^{-2} yr^{-1}, as the data for all global soils, which include the <10 Mg km^{-2} yr^{-1}

chemical denudation rate data, has an exponent significantly greater than 1.0 (Fig. A3.7). The <10 Mg km^{-2} yr^{-1} chemical denudation rate data exhibit considerable scatter and drive the high scaling exponent in the dataset containing all soils, so to conservatively estimate chemical denudation rates, we used the relationship with the lower scaling exponent. Because the scaling exponent of 0.97 is within one standard error of 1.0 (Fig. A3.7), we simply assume that chemical denudation rates scale linearly with denudation rates for the purpose of modeling global chemical denudation.

The total area of Earth's surface with given denudation and chemical denudation rates were determined by summing the areas of all pixels with the same value and plotting the cumulative distribution of denudation and chemical denudation as a function of slope gradient. Our calculation of the cumulative area denuding at a given rate accounts for the latitudinal influence on grid cell area in a manner similar to our slope gradient calculations.

Supplementary Figures

Figure A3.1. Photos of roots penetrating bedrock exposed by a recent tree fall. a, Coarse (cm-scale) roots growing in a foliation plane have opened an 810 cm fracture and have broken off a ~10 cm thick slab of schist. b, Fine (mm-scale) roots growing within planes of weakness within the schist contribute to chemical weathering and can physically spall mm-thick pieces of bedrock.

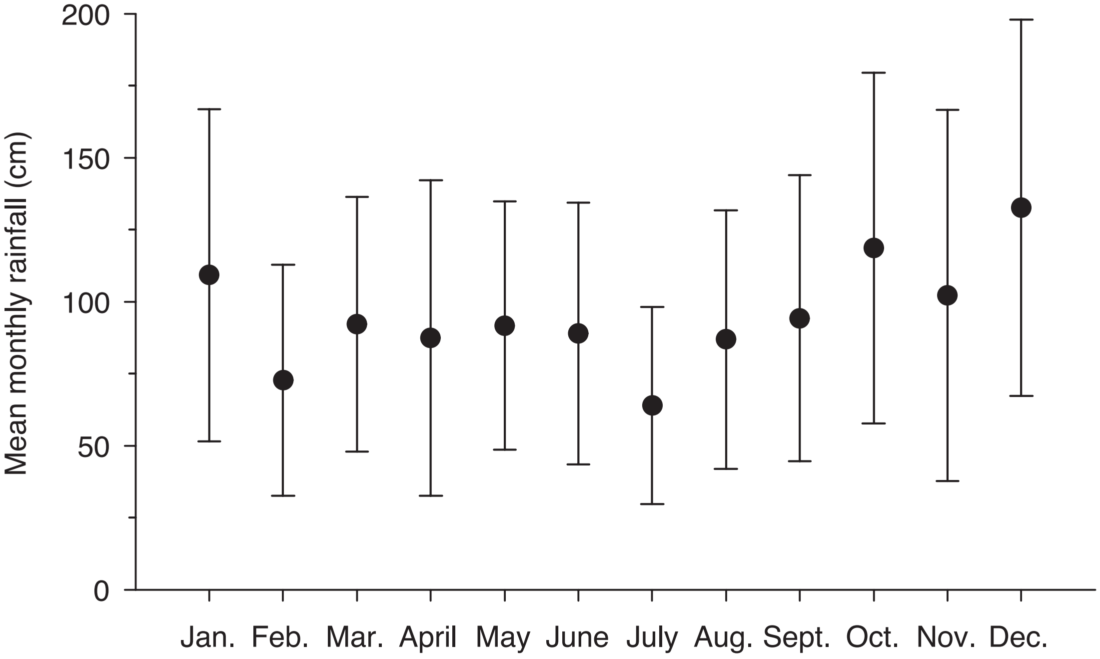

Figure A3.2. Mean monthly rainfall at the Cropp at Waterfall rain gage. Note that high rates of monthly rainfall are distributed throughout the year, with little seasonality. The rain gage is in the Cropp River catchment, which is adjacent to the Rapid Creek catchment we sampled, at an elevation of 975 m. The mean annual precipitation at this site is 11.52 m. Data are from July 1982 to October 2012, courtesy of the New Zealand National Institute of Water and Atmospheric Research. The mean annual temperature is about 5.5 °C (ref. 58).

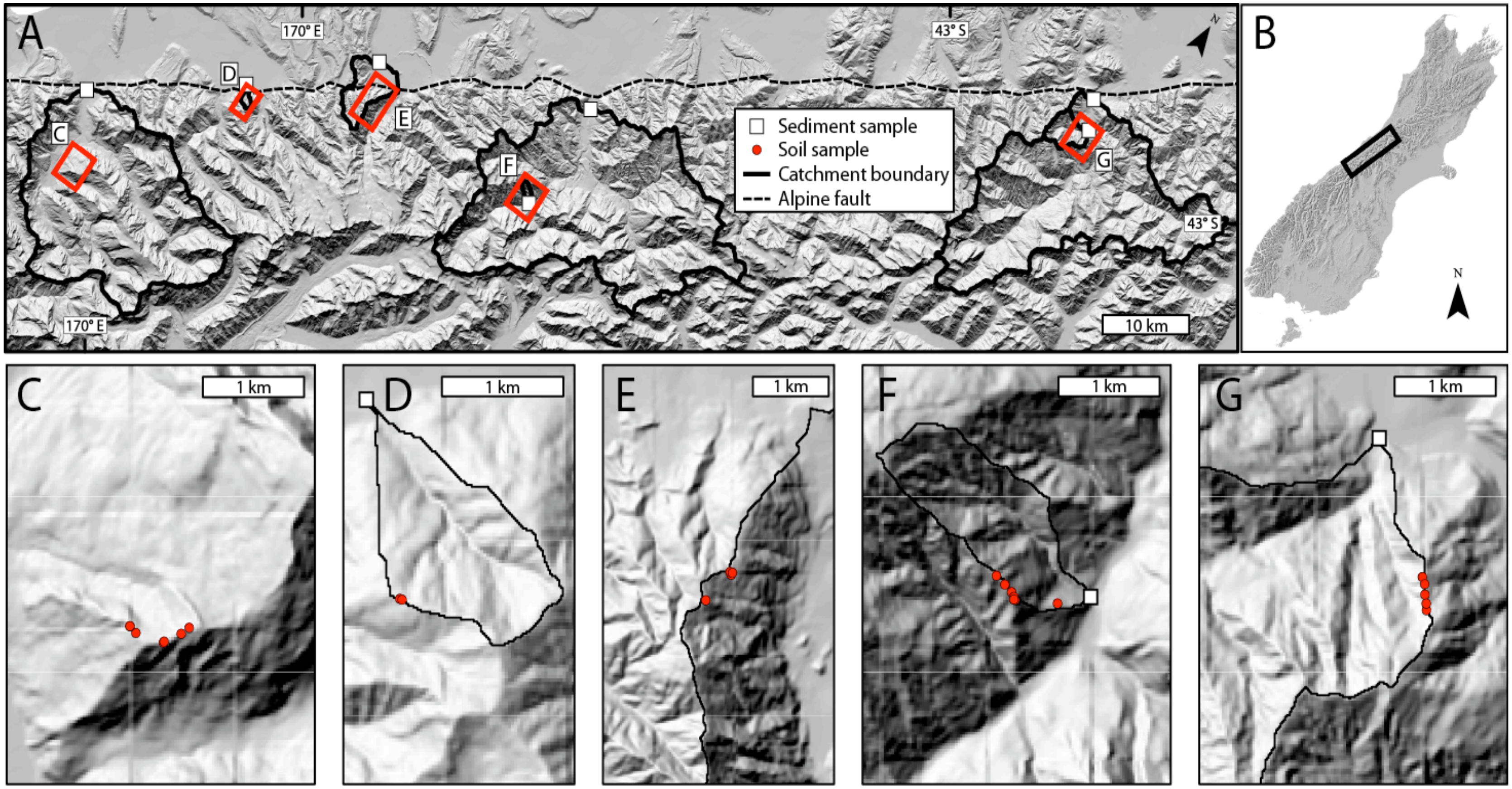

Figure A3.3. Sample locations. a, Hillshade map of the study area. The red boxes outline the bounds of panels c–g. b, Location of the study area on New Zealand’s South Island. c-g, Locations of soil samples on ridgetops.

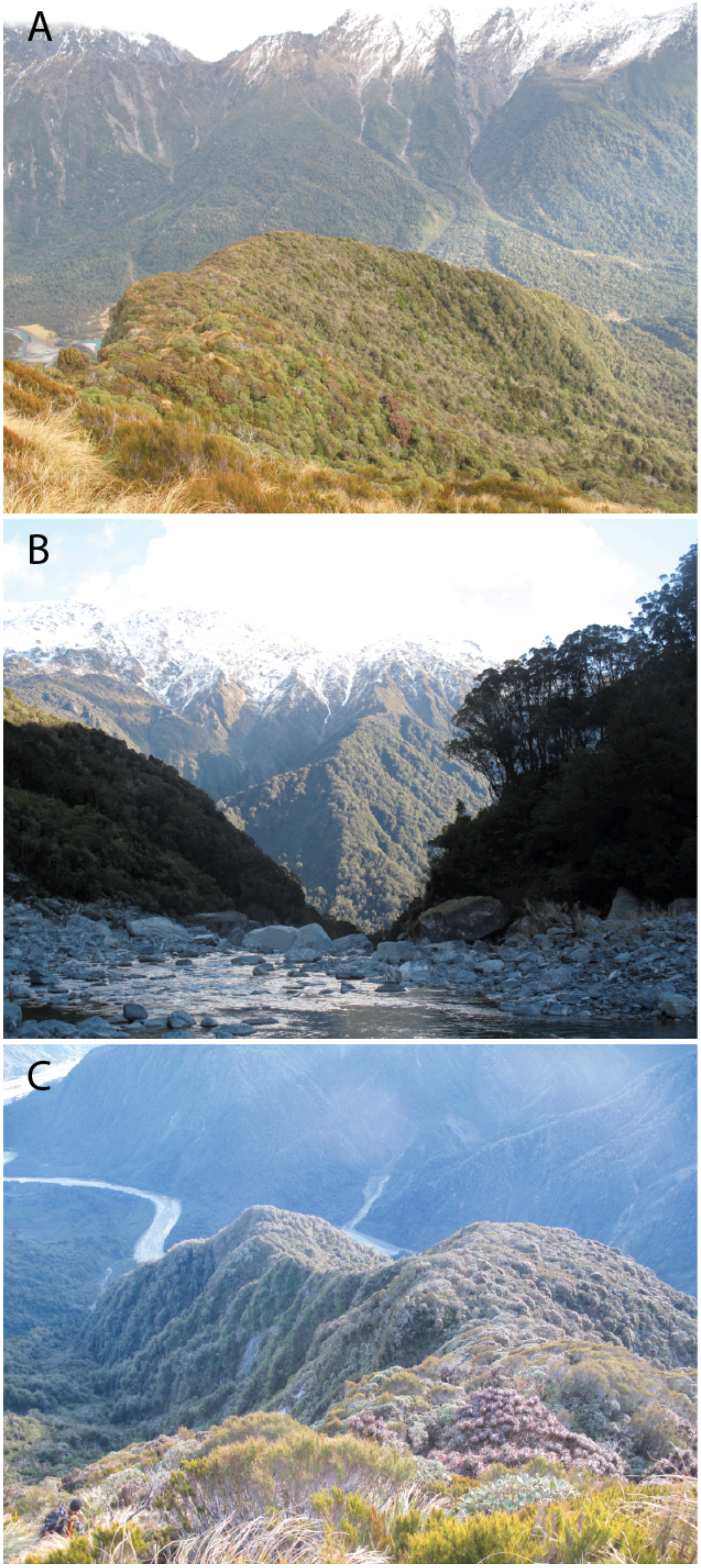

Figure A3.4. Photos of the ridges we sampled in the (a) Karangarua, (b) Whataroa, and (c) Hokitika catchments. Note that the dense vegetation is rooted in a near-continuous soil mantle.

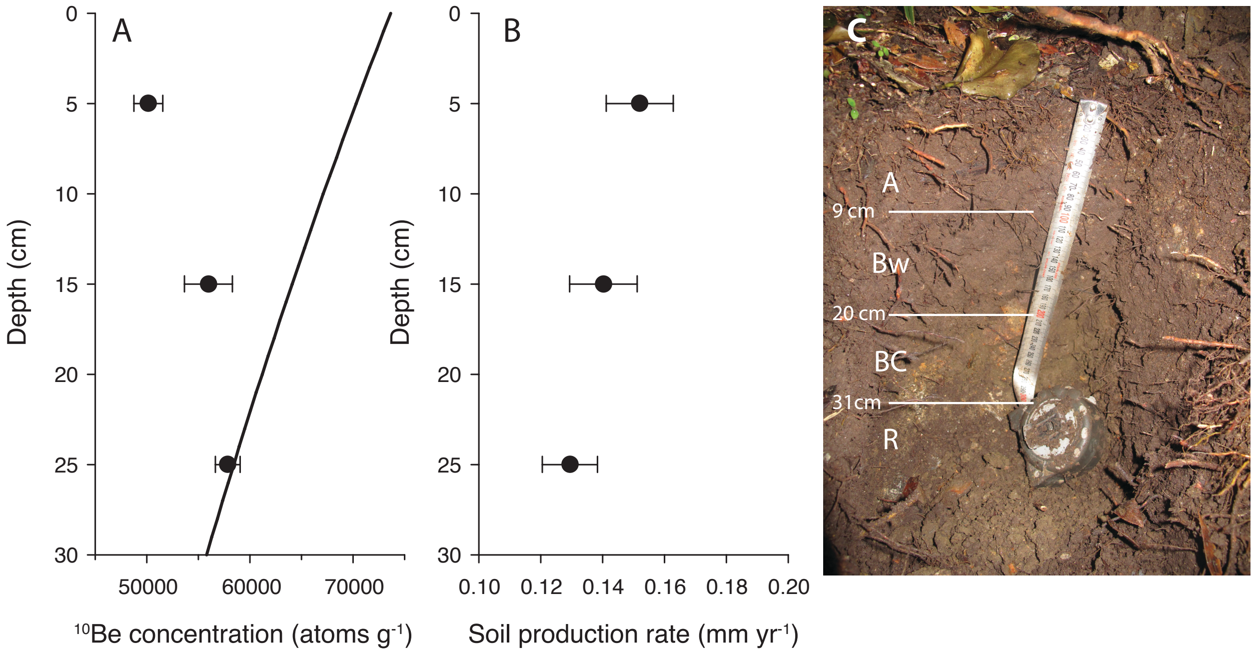

Figure A3.5. Alex Knob Pit 4 soil depth profile. a, ^{10}Be concentrations for samples from three depths. The upper, middle, and lower samples each span the 0–10 cm, 10–20 cm, and 20–30 cm depths, respectively. The black curve is the predicted ^{10}Be concentration for an unmixed soil, using a bulk density of 1.48 g cm^{-3}, the mean for the mineral Bw and BC horizons. The data do not follow the trend predicted by no mixing, indicating the soil has been mixed vertically by bioturbation. b, Soil production rates inferred from the ^{10}Be concentrations. c, Photo of the soil with designated soil horizons. The soil horizons correspond closely (within 1 cm) to the sample depth increments.

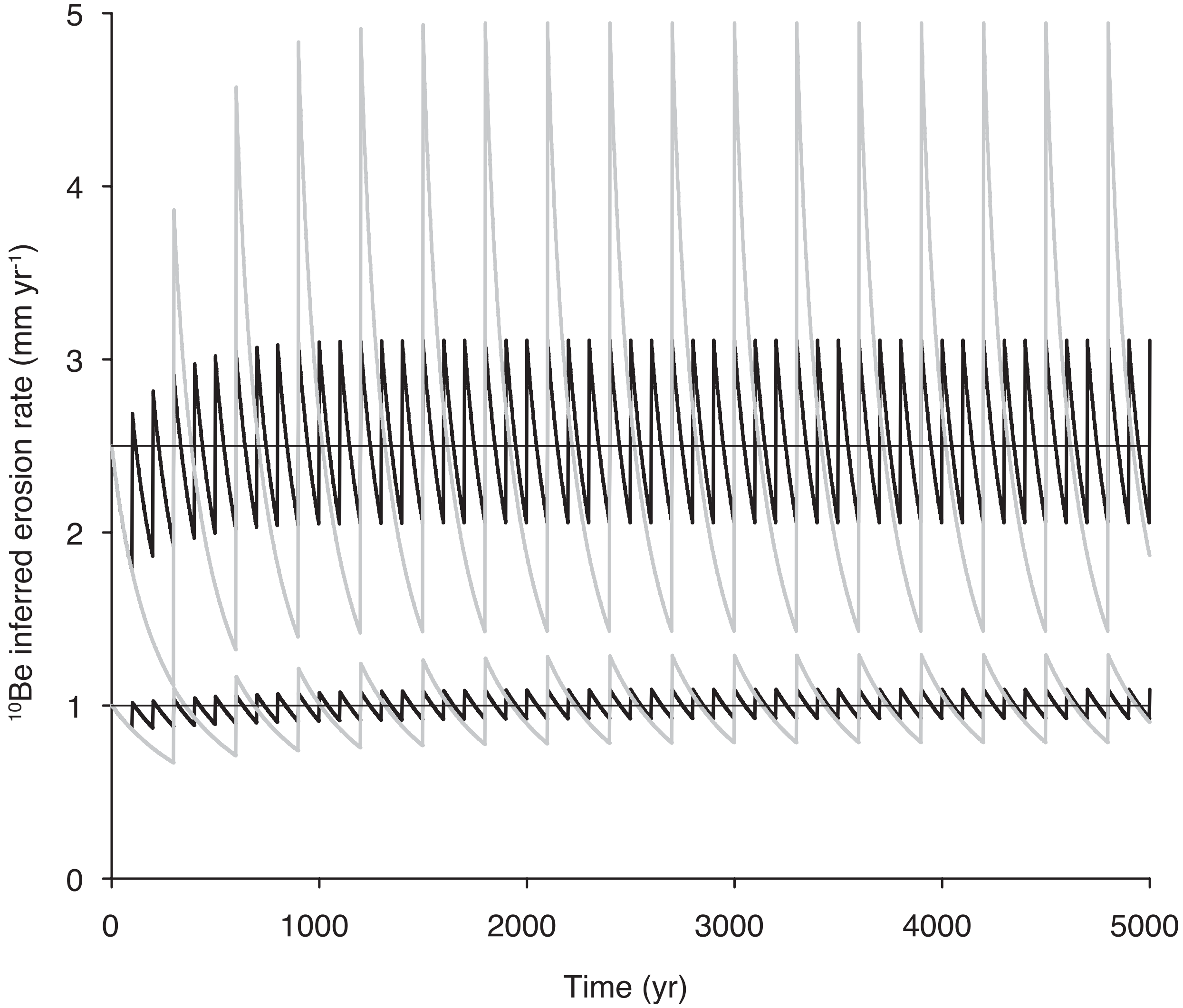

Figure A3.6. Variability in inferred soil production rates due to unsteady erosion. The upper and lower sets of curves are for 2.5 mm yr^{-1} and 1 mm yr^{-1} soil production rate scenarios, respectively. For both scenarios, the thin black line shows steady soil production, the thick black line shows soil production rates inferred from ^{10}Be when all erosion occurs once per century, and the gray line shows soil production rates inferred from ^{10}Be when all erosion occurs once every three centuries. The variability in inferred soil production rates caused by unsteady erosion is of the same (or lower) magnitude than analytical and ^{10}Be production rate scaling uncertainty, except for the 2.5 mm yr^{-1} scenario where all erosion occurs once ever 300 yr. In this case, the 750 mm of erosion is unrealistically high for a single tree fall event, but comparable to what might be expected due to shallow landsliding. As explained in the text, we designed our sampling strategy to avoid sampling areas subject to recent landsliding.

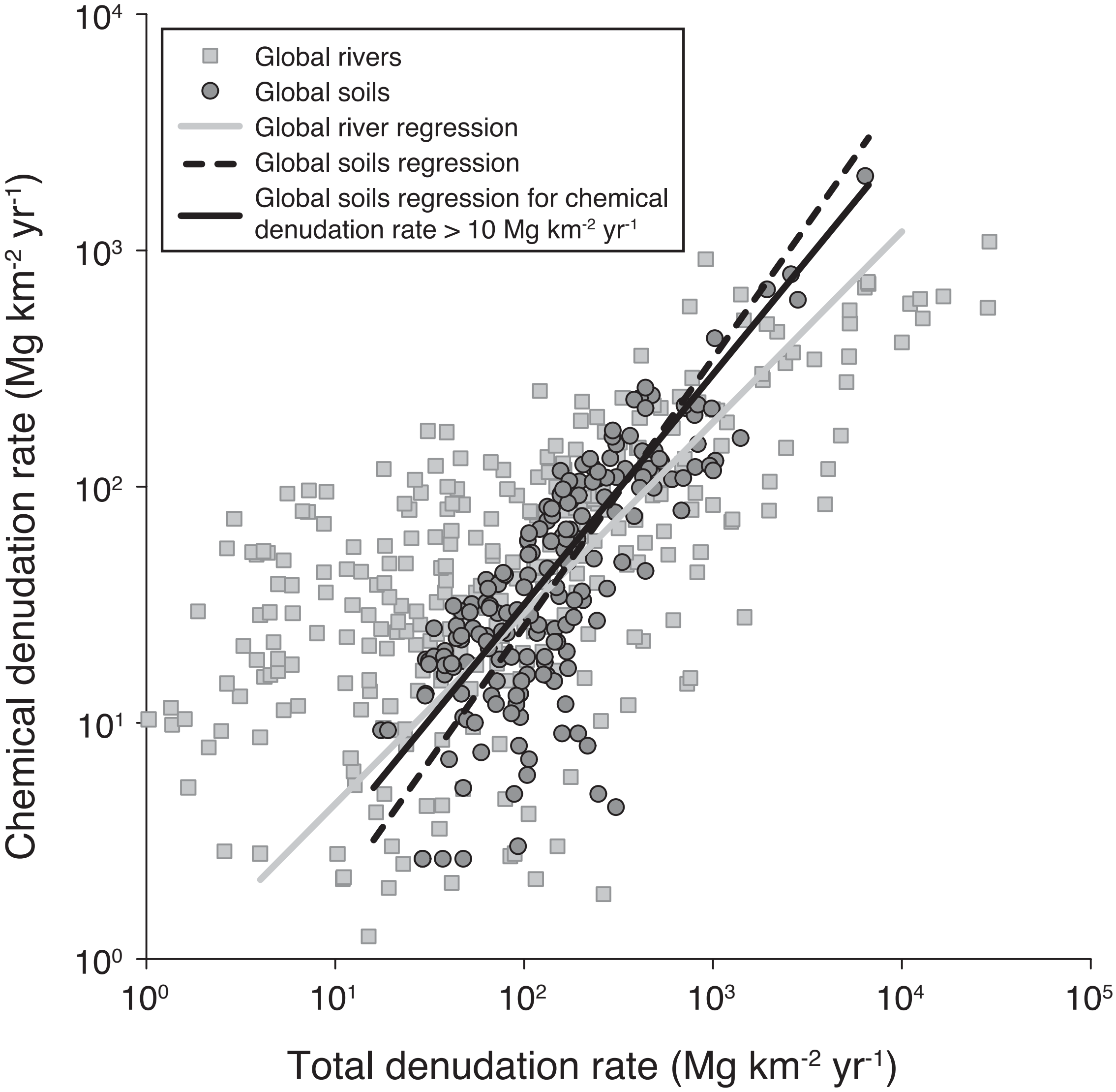

Figure A3.7 Chemical versus total denudation rate for global soil and river data. The RMA regression relationship for global soils is: $y = (10\text{^}{-0.86}(\pm 0.11))x^{1.14(\pm 0.052)}$, $R^2 = 0.62$, $p<0.001$. For global soils with chemical denudation rates greater than 10 Mg km^{-2} yr^{-1}, the relationship is: $y = (10\text{^}{-0.45}(\pm 0.089))x^{0.97(\pm 0.040)}$, $R^2 = 0.72$, $p<0.001$. The regression relationship for the global river data is: $y = (10\text{^}{-0.15}(\pm 0.066))x^{0.81(\pm 0.028)}$, $R^2 = 0.64$, $p<0.001$.

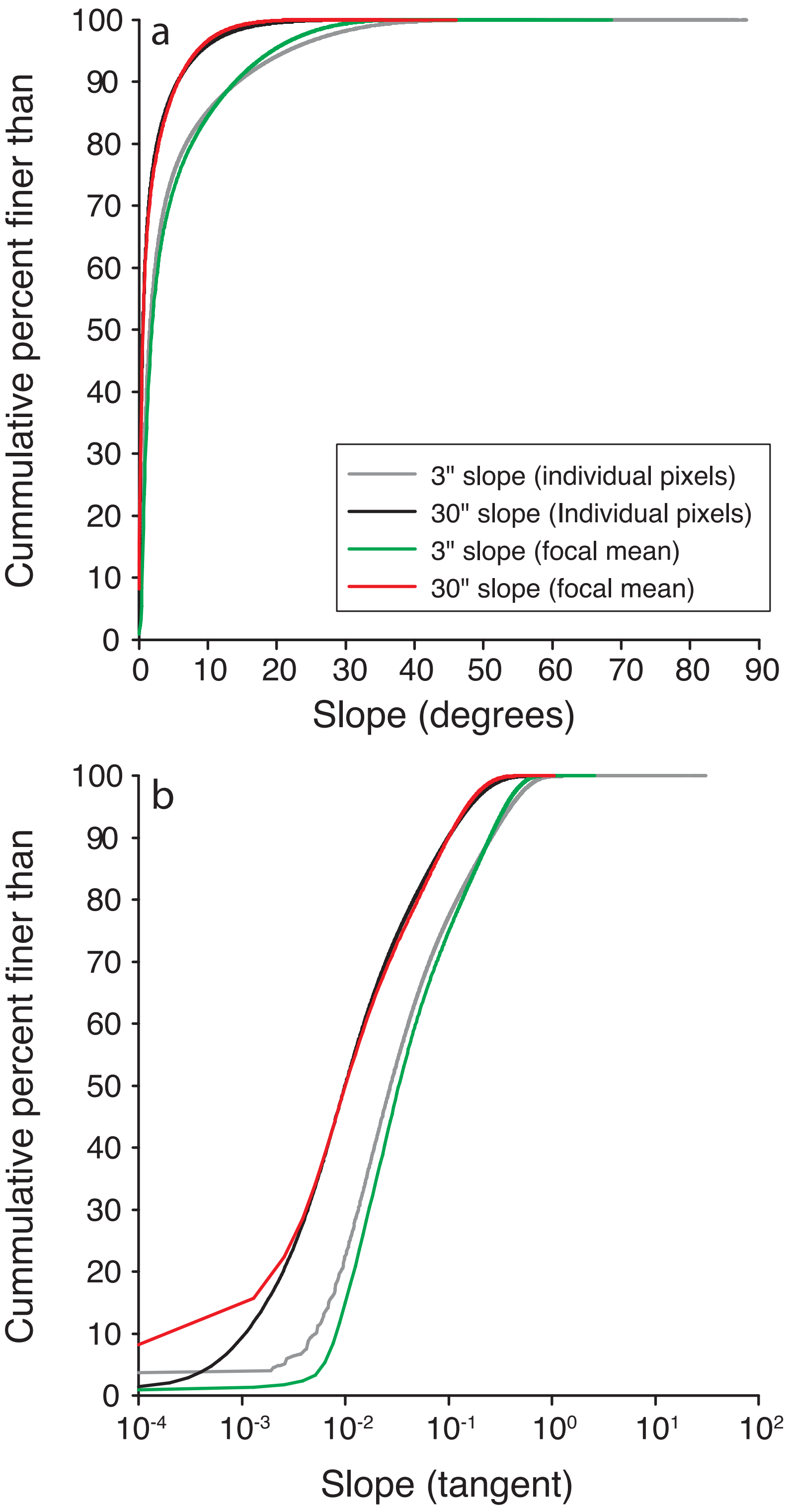

Figure A3.8. Global slope angle distributions for individual pixels and mean values calculated using a 5 km x 5 km moving window with slope expressed in degrees (a) and as the tangent (b). The percentages indicate the area of Earth's surface with slopes less than a given value. Areas with zero slope are expressed as tangent = 10^{-4}.

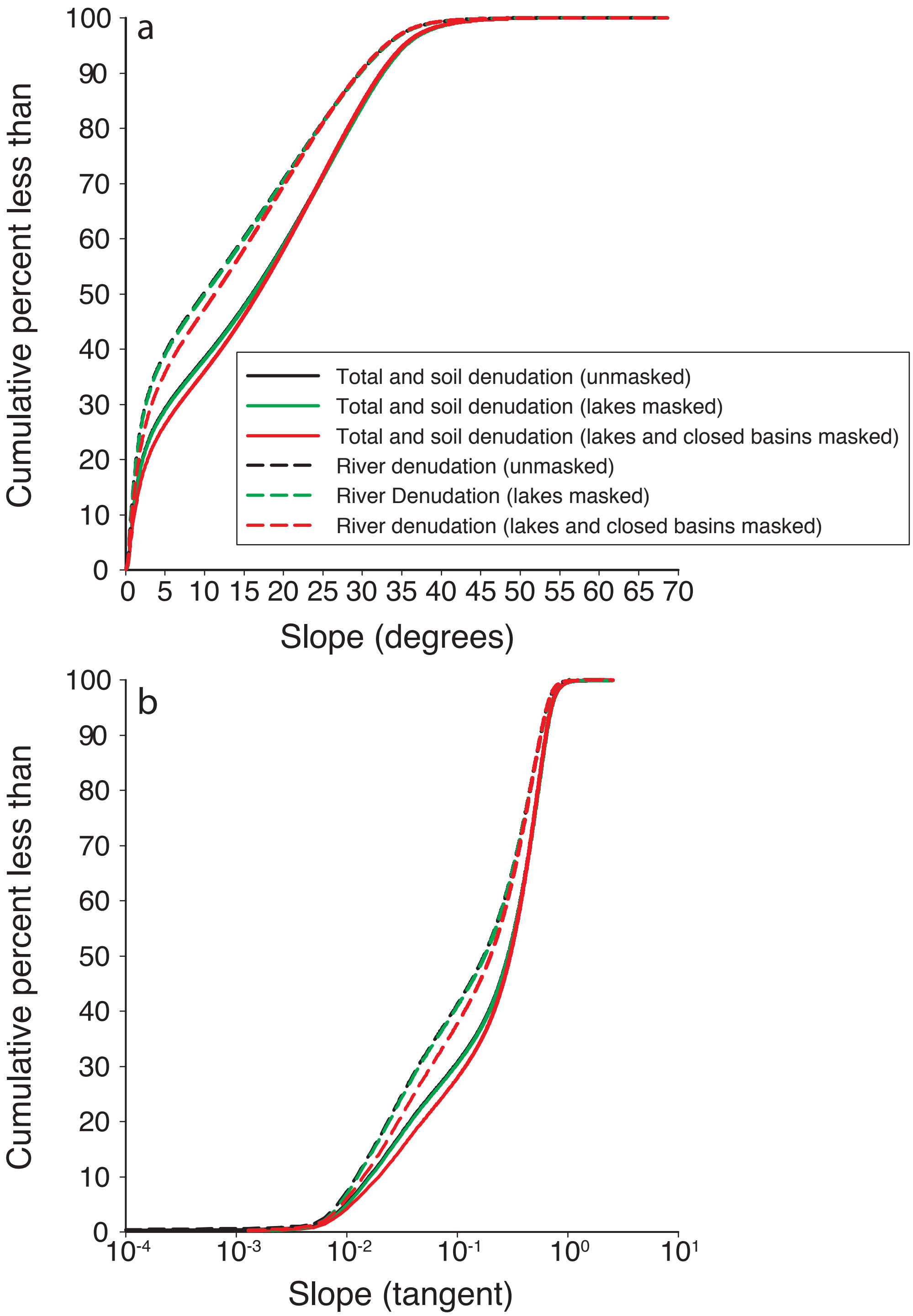

Figure A3.9. Global denudation rate distributions showing the percentage of Earth's total denudation generated from areas with different slope angles, with slope expressed in degrees (a) and as the tangent (b). The different curves show how removing (masking) lakes and closed basins influences the distributions. The distributions with lakes removed are nearly identical to the distributions for the entire global surface. All data are 3 arc-second resolution; areas with zero slope are expressed as tangent = 10^{-4}.

Supplementary Tables

Table A3.1. CRONUS calculator inputs. All samples assume a standard atmosphere and are normalized to the 07KNSTD ^{10}Be standard. The input sample thickness is 0.1 cm for all samples, with the exception of the Karangarua bedrock sample, which had a thickness of 1.6 cm.

Sample name	Lat.	Lon.	Elev. (m)	Density (g cm^{-3})	Shielding factor	^{10}Be conc. (atom g^{-1})	^{10}Be conc. uncertainty (atom g^{-1})
Karangarua-Pit-1	-43.65	169.85	1030	2.73	0.9889	28063.0	1280.3
Karangarua-Pit-2	-43.65	169.85	1082	2.6	0.9819	57364.6	2338.3
Karangarua-Pit-3	-43.65	169.85	1112	2.74	0.9564	73769.9	1724.7
Karangarua-Pit-4	-43.65	169.85	959	2.73	0.9797	20838.9	687.1
Karangarua-Pit-5	-43.65	169.85	961	2.72	0.9260	24799.4	1017.5
Karangarua-bedrock	-43.65	169.85	1085	2.74	0.9988	66381.1	2569.0
Karangarua-sed	-43.65	169.93	1004	2.7	0.9998	2219.2	187.6
Fox-Pit-1	-43.49	170.00	932	2.66	0.9874	35443.9	920.2
Fox-Pit-2	-43.49	170.00	942	2.65	0.9839	70921.8	1458.9
Fox_sed	-43.49	170.00	731	2.66	0.9874	5035.4	429.8
Alex-Knob-Pit-2	-43.42	170.16	846	2.68	0.9600	48980.2	1156.0
Alex-Knob-Pit-3	-43.42	170.15	947	2.69	0.9633	43287.9	1575.9
Alex_Knob_Pit_4_0-10_cm	-43.42	170.16	836	2.7	0.9874	50142.0	1393.5
Alex_Knob_Pit_4_10-20_cm	-43.42	170.16	836	2.7	0.9874	55983.1	2334.4
Alex_Knob_Pit_4_20-30_cm	-43.42	170.16	836	2.7	0.9874	57835.3	1203.4
Docherty_Creek_sed	-43.41	170.14	562	2.69	0.9985	3073.7	183.3
Gunn-Pit-1	-43.40	170.40	866	2.73	0.9874	14435.4	793.1
Gunn_Pit_2	-43.40	170.41	832	2.66	0.9723	20392.7	840.6
Gunn-Pit-3	-43.40	170.40	856	2.57	0.9446	19529.2	877.0
Gunn_Pit_4	-43.40	170.40	953	2.7	0.9857	43576.8	1940.2
Gunn-Pit-5	-43.40	170.40	910	2.65	0.9874	30577.9	1497.7
Gunn-Pit-6	-43.40	170.40	838	2.65	0.9750	20624.6	772.7
Gunn-Pit-7	-43.40	170.41	555	2.67	0.9750	24180.6	933.2
Gunn-Ridge-sed	-43.40	170.40	944	2.68	0.9819	1008.7	195.3
Whataroa-sed	-43.37	170.49	1017	2.68	0.9998	1257.6	336.6
Rapid-Creek-Pit-1	-43.03	171.02	966	2.97	0.9633	24875.5	1140.3
Rapid-Creek-Pit-2	-43.03	171.02	897	2.61	0.9260	11101.1	663.6
Rapid-Creek-Pit-3	-43.03	171.02	856	2.59	1.0000	8023.7	343.8
Rapid-Creek-Pit-4	-43.03	171.02	946	2.59	0.8916	3160.3	593.4
Rapid-Creek-Pit-5	-43.03	171.02	832	2.65	0.9819	7071.5	342.3
Rapid-Creek-sed	-43.03	170.99	1070	2.68	0.9948	1640.9	163.0
Hokitika_sed	-43.08	171.04	1124	2.68	0.9997	988.5	121.0

Table A3.2. Denudation rate and apparent exposure ages determined using the CRONUS calculator. Note that we do not use the soil denudation rate data presented here in our analyses, but the CEF-corrected values reported in Table A3.4.

Sample name	Denudation rate (mm yr^{-1})	Denudation rate uncertainty (mm yr^{-1})	Denudation rate (Mg km^{-2} yr^{-1})	Denudation rate uncertainty (Mg km^{-2} yr^{-1})	Apparent exposure age (yr)	Apparent exposure age uncertainty (yr)
Karangarua-Pit-1	0.29	0.02	789.6	63.5	2646	254
Karangarua-Pit-2	0.15	0.01	395.6	31.1	5177	485
Karangarua-Pit-3	0.11	0.01	306.4	21.9	6596	578
Karangarua-Pit-4	0.37	0.03	1010.3	73.8	2102	190
Karangarua-Pit-5	0.30	0.02	815.0	62.5	2634	247
Karangarua-bedrock	0.13	0.01	343.0	26.7	5917	550
Karangarua-sed	3.70	0.40	9986.5	1070.7	211	25
Fox-Pit-1	0.22	0.02	584.9	41.2	3618	319
Fox-Pit-2	0.11	0.01	291.1	20.3	7069	614
Fox_sed	1.38	0.15	3658.4	390.0	606	73
Alex-Knob-Pit-2	0.15	0.01	390.6	27.0	5470	479
Alex-Knob-Pit-3	0.18	0.01	473.5	35.6	4451	409
Alex_Knob_Pit_4_0-10_cm	0.14	0.01	387.0	27.5	5493	488
Alex_Knob_Pit_4_10-20_cm	0.13	0.01	346.1	26.9	6097	574
Alex_Knob_Pit_4_20-30_cm	0.12	0.01	334.8	23.0	6290	547
Docherty_Creek_sed	2.03	0.17	5448.2	468.2	421	43
Gunn-Pit-1	0.51	0.04	1380.7	117.0	1565	158
Gunn_Pit_2	0.36	0.03	945.2	72.1	2301	216
Gunn-Pit-3	0.38	0.03	981.4	76.8	2224	213
Gunn_Pit_4	0.18	0.01	480.3	38.3	4363	416
Gunn-Pit-5	0.25	0.02	668.5	54.6	3188	311
Gunn-Pit-6	0.35	0.03	939.9	69.9	2310	213
Gunn-Pit-7	0.25	0.02	670.6	49.2	3411	316
Gunn-Ridge-sed	7.78	1.64	20842.3	4402.7	103	22
Whataroa-sed	6.61	1.95	17716.7	5237.2	119	33
Rapid-Creek-Pit-1	0.28	0.02	832.6	66.4	2559	246
Rapid-Creek-Pit-2	0.67	0.06	1740.9	152.3	1258	130
Rapid-Creek-Pit-3	0.96	0.07	2485.2	191.6	871	82
Rapid-Creek-Pit-4	2.38	0.49	6167.8	1263.0	355	73
Rapid-Creek-Pit-5	1.04	0.08	2743.3	219.5	796	77
Rapid-Creek-sed	5.19	0.62	13912.9	1666.7	150	20
Hokitika_sed	8.96	1.26	23999.6	3375.8	86	13

Table A3.3. Soil loss-on-ignition (LOI), soil and bedrock Zr data, chemical depletion fractions (CDF), and chemical erosion fraction (CEF) correction, soil depth, and soil sampling site slope data.

Sample name	Soil LOI (%)	Zr_{soil} (ppm)	LOIcorrected Zr_{soil} (ppm)	Zr_{rock} (ppm)	CDF	CEF	Soil thickness (cm)	Local slope (degrees)
Karangarua-Pit-1	3.9	237	246	199	0.19	1.05	40	24
Karangarua-Pit-2	15.0	288	331	213	0.36	1.07	21	28
Karangarua-Pit-3	2.6	259	266	262	0.01	1.00	15	37
Karangarua-Pit-4	5.8	209	221	193	0.13	1.02	21	29
Karangarua-Pit-5	10.9	330	366	266	0.27	1.02	10	44
Fox-Pit-1	13.4	255	289	236	0.18	1.04	32	25
Fox-Pit-2	12.2	275	309	226	0.27	1.04	20	27
Alex-Knob-Pit-2	8.8	257	280	201	0.28	1.09	41	36
Alex-Knob-Pit-3	5.7	289	305	214	0.30	1.04	15	35
Alex_Knob_Pit_4_0-10_cm	8.5	224	243	181	0.26	1.06	31	29
Alex_Knob_Pit_4_10-20_cm	6.9	260	278	181	0.35	1.09	31	29
Alex_Knob_Pit_4_20-30_cm	5.5	215	227	181	0.20	1.04	31	29
Gunn-Pit-1	12.7	220	248	219	0.12	1.02	24	25
Gunn_Pit_2	7.6	238	256	223	0.13	1.02	25	32
Gunn-Pit-3	6.0	256	271	239	0.12	1.02	29	40
Gunn_Pit_4	8.2	262	284	206	0.27	1.08	39	26
Gunn-Pit-5	9.9	226	248	219	0.12	1.02	30	25
Gunn-Pit-6	6.0	243	258	199	0.23	1.05	27	31
Gunn-Pit-7	10.8	208	230	193	0.16	1.04	34	31
Rapid-Creek-Pit-1	5.1	208	219	107	0.51	1.23	40	35
Rapid-Creek-Pit-2	10.1	253	279	169	0.39	1.11	30	44
Rapid-Creek-Pit-3	7.1	233	249	170	0.32	1.04	16	0
Rapid-Creek-Pit-4	6.8	221	236	157	0.33	1.04	12	50
Rapid-Creek-Pit-5	25.4	213	267	207	0.23	1.03	15	28

Table A3.4. CEF-corrected soil denudation rate data. T = total denudation (soil production) rate, W = chemical denudation rate, and E = physical denudation rate.

Sample name	T (mm yr^{-1})	±T (mm yr^{-1})	T (Mg km^{-2} yr^{-1})	± T (Mg km^{-2} yr^{-1})	W (mm yr^{-1})	± W (mm yr^{-1})	W (Mg km^{-2} yr^{-1})	± W (Mg km^{-2} yr^{-1})	E (mm yr^{-1})	± E (mm yr^{-1})	E (Mg km^{-2} yr^{-1})	± E (Mg km^{-2} yr^{-1})
Karangarua-Pit-1	0.30	0.02	831.1	66.81	0.056	0.005	151.6	12.8	0.25	0.02	679.5	68.0
Karangarua-Pit-2	0.16	0.01	422.6	33.25	0.054	0.005	141.2	11.9	0.11	0.01	281.4	35.3
Karangarua-Pit-3	0.11	0.01	306.8	21.92	0.002	0.000	4.4	0.3	0.11	0.01	302.4	21.9
Karangarua-Pit-4	0.38	0.03	1028.4	75.15	0.047	0.004	128.7	9.6	0.33	0.03	899.8	75.8
Karangarua-Pit-5	0.31	0.02	833.6	63.93	0.082	0.006	222.6	17.5	0.22	0.02	610.9	66.3
Fox-Pit-1	0.23	0.02	608.7	42.91	0.040	0.003	107.3	7.9	0.19	0.02	501.4	43.6
Fox-Pit-2	0.11	0.01	303.6	21.17	0.029	0.002	77.9	5.7	0.09	0.01	225.7	21.9
Alex-Knob-Pit-2	0.16	0.01	425.1	29.43	0.041	0.003	109.8	8.3	0.12	0.01	315.3	30.6
Alex-Knob-Pit-3	0.18	0.01	491.6	36.95	0.053	0.004	141.7	11.1	0.13	0.01	349.9	38.6
Alex_Knob_Pit_4_0-10_cm	0.15	0.01	410.3	29.14	0.037	0.003	98.7	7.4	0.12	0.01	311.6	30.1
Alex_Knob_Pit_4_10-20_cm	0.14	0.01	378.7	29.49	0.045	0.004	120.6	10.3	0.10	0.01	258.1	31.2
Alex_Knob_Pit_4_20-30_cm	0.13	0.01	349.7	24.05	0.025	0.002	67.6	4.9	0.10	0.01	282.1	24.5
Gunn-Pit-1	0.52	0.04	1406.0	119.15	0.059	0.005	160.6	13.9	0.46	0.04	1245.4	120.0
Gunn_Pit_2	0.36	0.03	965.5	73.66	0.046	0.004	122.3	9.5	0.32	0.03	843.2	74.3
Gunn-Pit-3	0.39	0.03	1003.4	78.51	0.046	0.004	117.1	9.4	0.34	0.03	886.3	79.1
Gunn_Pit_4	0.19	0.02	519.4	41.40	0.049	0.004	131.3	11.3	0.14	0.02	388.1	42.9
Gunn-Pit-5	0.26	0.02	683.8	55.90	0.030	0.002	79.0	6.6	0.23	0.02	604.9	56.3
Gunn-Pit-6	0.37	0.03	982.8	73.10	0.081	0.006	213.6	16.6	0.29	0.03	769.2	75.0
Gunn-Pit-7	0.26	0.02	695.5	51.06	0.041	0.003	108.8	8.3	0.22	0.02	586.7	51.7
Rapid-Creek-Pit-1	0.34	0.03	1024.5	81.68	0.143	0.014	424.9	41.7	0.20	0.03	599.6	91.7
Rapid-Creek-Pit-2	0.74	0.06	1933.8	169.17	0.262	0.025	684.7	66.5	0.48	0.07	1249.2	181.8
Rapid-Creek-Pit-3	1.00	0.08	2595.8	200.14	0.306	0.025	791.9	63.8	0.70	0.08	1803.9	210.0
Rapid-Creek-Pit-4	2.47	0.51	6391.9	1308.85	0.797	0.169	2064.0	438.0	1.67	0.53	4328.0	1380.2
Rapid-Creek-Pit-5	1.06	0.08	2812.3	225.02	0.233	0.019	617.3	50.6	0.83	0.09	2195.0	230.6

Table A3.5. Blank information, sample size, Be carrier weights, isotope ratio, and quartz yield data. ^{9}Be carrier concentration error=0.8%. na=not applicable

Sample name	Blank name	Sample mass (g quartz)	Be carrier (µg)	^{10}Be/^{9}Be ratio (corrected for boron)	^{10}Be/^{9}Be ratio uncertainty (corrected for boron)	^{10}Be/^{9}Be ratio (corrected for boron and blank)	^{10}Be/^{9}Be ratio uncertainty (corrected for boron and blank)	Quartz yield from bulk soil (%)	Quartz yield from 250-850 µm fraction (%)
Karangarua-Pit-1	Blank_ijl_15feb2012	31.5248	244.4	5.465E-14	2.427E-15	5.417E-14	2.430E-15	2.3	35.2
Karangarua-Pit-2	Blank-ijl31aug2012	20.3623	244.9	7.138E-14	2.837E-15	7.138E-14	2.837E-15	2.0	32.9
Karangarua-Pit-3	Blank_ijl_15feb2012	31.5192	244.9	1.426E-13	3.117E-15	1.421E-13	3.119E-15	2.5	56.1
Karangarua-Pit-4	Blank_ijl_15june2012	33.2208	244.8	4.335E-14	1.029E-15	4.232E-14	1.203E-15	3.2	38.2
Karangarua-Pit-5	Blank_ijl_15feb2012	32.3650	244.5	4.961E-14	1.970E-15	4.913E-14	1.973E-15	2.4	28.9
Karangarua-bedrock	Blank_ijl_3aug2012	24.2542	245.8	9.802E-14	3.700E-15	9.802E-14	3.700E-15	na	37.1
Karangarua-sed	Blank_ijl_15feb2012	37.4834	244.0	5.580E-15	3.953E-16	5.102E-15	4.126E-16	na	30.1
Fox-Pit-1	Blank-ijl31aug2012	25.9308	245.8	5.596E-14	1.350E-15	5.596E-14	1.350E-15	3.4	17.6
Fox-Pit-2	Blank-ijl31aug2012	26.8048	246.0	1.156E-13	2.172E-15	1.156E-13	2.172E-15	5.0	52.1
Fox_sed	Blank_ijl_3aug2012	38.6035	246.2	1.182E-14	9.972E-16	1.182E-14	9.972E-16	na	20.7
Alex-Knob-Pit-2	Blank-ijl31aug2012	24.9813	245.2	7.468E-14	1.631E-15	7.468E-14	1.631E-15	2.4	39.7
Alex-Knob-Pit-3	Blank-ijl31aug2012	24.7428	246.0	6.516E-14	2.295E-15	6.516E-14	2.295E-15	2.6	32.3
Alex_Knob_Pit_4_0-10_cm	Blank_ijl_3aug2012	27.2564	246.2	8.307E-14	2.208E-15	8.307E-14	2.208E-15	1.4	23.4
Alex_Knob_Pit_4_10-20_cm	Blank_ijl_3aug2012	27.3397	246.1	9.307E-14	3.807E-15	9.307E-14	3.807E-15	1.6	22.8
Alex_Knob_Pit_4_20-30_cm	Blank_ijl_3aug2012	27.8965	245.9	9.819E-14	1.882E-15	9.819E-14	1.882E-15	1.3	33.0
Docherty_Creek_sed	Blank_ijl_3aug2012	37.6864	245.9	7.050E-15	3.999E-16	7.050E-15	3.999E-16	na	20.5
Gunn-Pit-1	Blank_ijl_15june2012	25.5671	244.4	2.363E-14	8.573E-16	2.260E-14	1.059E-15	1.4	25.4
Gunn_Pit_2	Blank_ijl_3aug2012	28.2016	245.5	3.506E-14	1.413E-15	3.506E-14	1.413E-15	1.2	32.7
Gunn-Pit-3	Blank_ijl_15june2012	25.8279	244.6	3.189E-14	1.042E-15	3.086E-14	1.214E-15	1.7	45.2
Gunn_Pit_4	Blank_ijl_15june2012	25.0069	243.8	6.792E-14	2.794E-15	6.689E-14	2.862E-15	1.6	34.5
Gunn-Pit-5	Blank-205-IL-JS	24.8587	243.6	4.670E-14	2.246E-15	4.670E-14	2.246E-15	1.8	26.5
Gunn-Pit-6	Blank-ijl31aug2012	24.7996	246.2	3.109E-14	1.099E-15	3.109E-14	1.099E-15	1.7	46.4

Gunn-Pit-7	Blank-ijl31aug2012	25.7644	245.2	3.802E-14	1.404E-15	3.802E-14	1.404E-15	1.2	23.5
Gunn-Ridge-sed	Blank-205-IL-JS	33.5699	242.6	2.089E-15	3.383E-16	2.089E-15	3.383E-16	na	21.7
Whataroa-sed	Blank_ijl_15feb2012	38.2650	242.8	3.444E-15	7.755E-16	2.966E-15	7.845E-16	na	25.4
Rapid-Creek-Pit-1	Blank_ijl_15june2012	32.3075	244.6	5.020E-14	2.038E-15	4.917E-14	2.130E-15	1.9	35.0
Rapid-Creek-Pit-2	Blank_ijl_15june2012	29.0639	244.8	2.075E-14	7.698E-16	1.972E-14	9.894E-16	2.7	14.0
Rapid-Creek-Pit-3	Blank_ijl_15feb2012	30.5438	245.1	1.544E-14	6.073E-16	1.496E-14	6.187E-16	2.2	23.5
Rapid-Creek-Pit-4	Blank_ijl_15june2012	31.0972	244.8	7.038E-15	7.054E-16	6.008E-15	9.402E-16	1.6	18.2
Rapid-Creek-Pit-5	Blank-ijl31aug2012	30.1100	245.4	1.298E-14	5.444E-16	1.298E-14	5.444E-16	2.1	18.4
Rapid-Creek-sed	Blank_ijl_15feb2012	37.2632	244.7	4.218E-15	3.303E-16	3.739E-15	3.509E-16	na	20.4
Hokitika_sed	Blank_ijl_3aug2012	37.8328	245.8	2.277E-15	2.522E-16	2.277E-15	2.522E-16	na	20.0
Blank_ijl_15feb2012	Blank_ijl_15feb2012	na	244.5	4.782E-16	1.183E-16	na	na	na	na
Blank_ijl_15june2012	Blank_ijl_15june2012	na	244.8	1.030E-15	6.216E-16	na	na	na	na
Blank_ijl_3aug2012	Blank_ijl_3aug2012	na	246.1	5.361E-16	1.169E-16	na	na	na	na
Blank-205-IL-JS	Blank-205-IL-JS	na	242.1	2.947E-16	2.214E-16	na	na	na	na
Blank-ijl31aug2012	Blank-ijl31aug2012	na	245.4	4.489E-16	2.964E-16	na	na	na	na

Table A3.6. Sediment sample locations, UTM zone 59S, WGS84 datum.

Sample	Northing	Easting
Karangarua-sed	5174514	403755
Fox-sed	5185320	418733
Docherty-Creek-sed	5196260	429580
Gunn-Ridge-sed	5194083	452560
Whataroa-sed	5206454	452429
Rapid-Creek-sed	5237499	500973
Hokitika-sed	5240528	499687

Table A3.7 Soil bulk density data. The third column indicates the depth of the top of the excavated cavity with respect to the mineral soil surface. Due to the presence of roots and rocks, it was difficult to measure cavity volumes accurately. The upper 5-10 cm of each soil profile was generally A-horizon material. Dry weights reflect drying w at high temperature >120° for 18 h (for sterilization). nd indicates no data.

Soil pit	Volume (cm^3)	Depth (cm)	Wet weight (g)	Dry weight (g)	Wet density (g cm^{-3})	Dry density (g cm^{-3})
Alex Pit 1	85	12	137.5	72.7	1.7	0.9
Fox Pit 1	110	0	29	23.5	0.3	0.21
Fox Pit 1	50	10	72.6	57.6	1.5	1.15
Fox Pit 2	120	5	153.4	54.5	1.3	0.45
Fox Pit 2	80	12	124.3	66	1.6	0.83
Alex Pit 2	60	6	75.9	33.6	1.3	0.56
Alex Pit 2	40	21	108.5	74.6	2.7	1.87
Alex Pit 3	125	11	214.6	101.9	1.7	0.82
Karangarua Pit 1	nd	18	236.3	134.4	nd	nd
Karangarua Pit 2	190	17	309.8	165.2	1.6	0.87
Karangarua Pit 3	165	12	208.5	87.7	1.3	0.53
Karangarua Pit 4	190	3	310.8	187.8	1.6	0.99
Karangarua Pit 5	130	1	192.5	125.3	1.5	0.96
Rapid Creek Pit 1	140	11	235.6	119	1.7	0.85
Rapid Creek Pit 2	140	4	221.4	120	1.6	0.86
Rapid Creek Pit 3	150	4	212.9	115.7	1.4	0.77
Rapid Creek Pit 4	95	1	115	43.9	1.2	0.46
Rapid Creek Pit 5	210	3	215.9	84.9	1.0	0.40
Gunn Pit 1	140	19	148.1	78.7	1.1	0.56
Gunn Pit 2	80	10	172.8	107.3	2.2	1.34
Gunn Pit 3	70	12	117	66.9	1.7	0.96
Gunn Pit 4	60	11	115.1	71.3	1.9	1.19
Gunn Pit 5	140	6	152.6	88	1.1	0.63
Gunn Pit 6	110	6	182.3	119	1.7	1.08
Gunn Pit 7	140	11	104.5	67.7	0.7	0.48
AlexPit 4 0-10 cm	130	2	128.9	98.1	1.0	0.75
AlexPit 4 10-20 cm	60	13	128.6	91.1	2.1	1.52
AlexPit 4 20-30 cm	95	20	149.1	136.5	1.6	1.44

Supplementary References

1. Burt, R. (ed.). Soil Survey Investigations Report No. 51, Version 1.0, Natural Resources Conservation Service, U.S. Department of Agriculture, 407 p. (2009).
2. Stone, J. O. *Extraction of Al and Be from quartz for isotopic analysis*, <http://depts.washington.edu/cosmolab/chem/Al-26_Be-10.pdf> (2001).
3. Ditchburn, R. & Whitehead, N. in *3rd workshop of the South Pacific Environmental Radioactivity Association,* p. 4-7 (1994).
4. Riebe, C., Kirchner, J., Granger, D. & Finkel, R. Strong tectonic and weak climatic control of long-term chemical weathering rates. *Geology* **29**, 511-514 (2001).
5. Riebe, C. S., Kirchner, J. W. & Finkel, R. C. Erosional and climatic effects on long-term chemical weathering rates in granitic landscapes spanning diverse climate regimes. *Earth. Planet. Sci. Lett.* **224**, 547-562 (2004).
6. Ferrier, K., Kirchner, J. W. & Finkel, R. Weak influences of climate and mineral supply rates on chemical erosion rates: Measurements along two altitudinal transects in the Idaho Batholith. *Journal of Geophysical Research* **117**, F02026 (2012).
7. Granger, D., Kirchner, J. & Finkel, R. Spatially averaged long-term erosion rates measured from in situ-produced cosmogenic nuclides in alluvial sediment. *Journal of Geology* **104**, 249-257 (1996).
8. Granger, D. & Riebe, C. in *Treatise on Geochemistry* Vol. 5 (ed JI Drever) Ch. 5.19, (Elsivier, 2007).
9. Brown, E., Stallard, R., Larsen, M., Raisbeck, G. & Yiou, F. Denudation rates determined from the accumulation of in situ-produced ^{10}Be in the Luquillo Experimental Forest, Puerto Rico. *Earth. Planet. Sci. Lett.* **129**, 193-202 (1995).
10. Jungers, M. C. *et al.* Tracing hillslope sediment production and transport with in situ and meteoric ^{10}Be. *Journal of Geophysical Research* **114**, F04020 (2009).
11. Brown, E., Colin, F. & Bourlès, D. Quantitative evaluation of soil processes using in situ-produced cosmogenic nuclides. *Comptes Rendus Geoscience* **335**, 1161-1171 (2003).
12. Bierman, P. & Steig, E. Estimating rates of denudation using cosmogenic isotope abundances in sediment. *Earth Surface Processes and Landforms* **21**, 125-139 (1996).
13. Lal, D. Cosmic ray labeling of erosion surfaces: *in situ* nuclide production rates and erosion models. *Earth. Planet. Sci. Lett.* **104**, 424-439 (1991).
14. Hovius, N., Stark, C. & Allen, P. Sediment flux from a mountain belt derived by landslide mapping. *Geology* **25**, 231-234 (1997).
15. Small, E., Anderson, R. S., Repka, J. L. & Finkel, R. Erosion rates of alpine bedrock summit surfaces deduced from in situ ^{10}Be and ^{26}Al. *Earth. Planet. Sci. Lett.* **150**, 413-425 (1997).
16. Roering, J. Hillslope evolution by nonlinear, slope-dependent transport: Steady state morphology and equilibrium adjustment timescales. *Journal of Geophysical Research* **106**, 16499-16513 (2001).
17. Burbank, D. *et al.* Bedrock incision, rock uplift and threshold hillslopes in the northwestern Himalayas. *Nature* **379**, 505-510 (1996).
18. Reif, A. & Allen, R. Plant communities of the steepland conifer-broadleaved hardwood forests of central Westland, South Island, New Zealand. *Phytocoenologia* **16**, 145-224 (1988).

19. Harrison, J. Soil distribution and landscape dynamics, Camp Creek, Westland, in *Proceedings of the soil dynamics and land use seminar.* (ed IB Campbell) (New Zealand Society of Soil Science, Lower Hutt, and New Zealand Soil Conservators Association, 1985).
20. Hilton, R., Meunier, P., Hovius, N., Bellingham, P. & Galy, A. Landslide impact on organic carbon cycling in a temperate montane forest. *Earth Surface Processes and Landforms* **36**, 1670-1679 (2011).
21. Clarke, B. A. & Burbank, D. W. Quantifying bedrock-fracture patterns within the shallow subsurface: Implications for rock mass strength, bedrock landslides, and erodibility. *Journal of Geophysical Research* **116**, F04009, (2011).
22. Meunier, P., Hovius, N. & Haines, J. A. Topographic site effects and the location of earthquake induced landslides. *Earth. Planet. Sci. Lett.* **275**, 221-232 (2008).
23. Sutherland, R. *et al.* Do great earthquakes occur on the Alpine Fault in central South Island, New Zealand? *Geophysical Monograph Series* **175**, 235-251 (2007).
24. Roering, J., Marshall, J., Booth, A., Mort, M. & Jin, Q. Evidence for biotic controls on topography and soil production. *Earth. Planet. Sci. Lett.* **298**, 183-190 (2010).
25. Gabet, E. J. & Mudd, S. M. Bedrock erosion by root fracture and tree throw: A coupled biogeomorphic model to explore the humped soil production function and the persistence of hillslope soils. *Journal of Geophysical Research* **115**, F04005 (2010).
26. Reinhardt, L. J. *et al.* Interpreting erosion rates from cosmogenic radionuclide concentrations measured in rapidly eroding terrain. *Earth Surface Processes and Landforms* **32**, 390-406 (2007).
27. Balco, G. *et al.* Regional beryllium-10 production rate calibration for late-glacial northeastern North America. *Quaternary Geochronology* **4**, 93-107 (2009).
28. Putnam, A. *et al.* In situ cosmogenic ^{10}Be production-rate calibration from the Southern Alps, New Zealand. *Quaternary Geochronology* **5**, 392-409 (2010).
29. McKean, J., Dietrich, W., Finkel, R., Southon, J. & Caffee, M. Quantification of soil production and downslope creep rates from cosmogenic ^{10}Be accumulations on a hillslope profile. *Geology* **21**, 343 (1993).
30. Phillips, J., Turkington, A. & Marion, D. Weathering and vegetation effects in early stages of soil formation. *Catena* **72**, 21-28 (2008).
31. Niemi, N., Oskin, M., Burbank, D., Heimsath, A. & Gabet, E. Effects of bedrock landslides on cosmogenically determined erosion rates. *Earth. Planet. Sci. Lett.* **237**, 480-498 (2005).
32. Yanites, B., Tucker, G. & Anderson, R. Numerical and analytical models of cosmogenic radionuclide dynamics in landslide-dominated drainage basins. *Journal of Geophysical Research* **114**, F01007 (2009).
33. Balco, G., Stone, J., Lifton, N. & Dunai, T. A complete and easily accessible means of calculating surface exposure ages or erosion rates from ^{10}Be and ^{26}Al measurements. *Quaternary Geochronology* **3**, 174-195 (2008).
34. Binnie, S., Phillips, W., Summerfield, M. & Fifield, L. Sediment mixing and basin-wide cosmogenic nuclide analysis in rapidly eroding mountainous environments. *Quaternary Geochronology* **1**, 4-14 (2006).
35. Stone, J. Air pressure and cosmogenic isotope production. *Journal of Geophysical Research* **105**, 23753-23759 (2000).

36. Small, E., Anderson, R. & Hancock, G. Estimates of the rate of regolith production using ^{10}Be and ^{26}Al from an alpine hillslope. *Geomorphology* **27**, 131-150 (1999).
37. Riebe, C., Kirchner, J. & Granger, D. Quantifying quartz enrichment and its consequences for cosmogenic measurements of erosion rates from alluvial sediment and regolith. *Geomorphology* **40**, 15-19 (2001).
38. Riebe, C. S. & Granger, D. E. Quantifying effects of deep and near-surface chemical erosion on cosmogenic nuclides in soils, saprolite, and sediment. *Earth Surface Processes and Landforms*, doi:DOI: 10.1002/esp.3339 (2013).
39. Heimsath, A., Dietrich, W., Nishiizumi, K. & Finkel, R. The soil production function and landscape equilibrium. *Nature* **388**, 358-361 (1997).
40. Dixon, J., Heimsath, A., Kaste, J. & Amundson, R. Climate-driven processes of hillslope weathering. *Geology* **37**, 975-978 (2009).
41. Heimsath, A., Chappell, J., Dietrich, W., Nishiizumi, K. & Finkel, R. Late Quaternary erosion in southeastern Australia: a field example using cosmogenic nuclides. *Quaternary International* **83**, 169-185 (2001).
42. Heimsath, A., Chappell, J., Dietrich, W., Nishiizumi, K. & Finkel, R. Soil production on a retreating escarpment in southeastern Australia. *Geology* **28**, 787-790 (2000).
43. Heimsath, A., DiBiase, R. & Whipple, K. X. Soil production limits and the transition to bedrock-dominated landscapes. *Nature Geoscience* **5**, 210-214, (2012).
44. Heimsath, A., Dietrich, W., Nishiizumi, K. & Finkel, R. Stochastic processes of soil production and transport: Erosion rates, topographic variation and cosmogenic nuclides in the Oregon Coast Range. *Earth Surface Processes and Landforms* **26**, 531-552 (2001).
45. Heimsath, A., Furbish, D. & Dietrich, W. The illusion of diffusion: Field evidence for depth-dependent sediment transport. *Geology* **33**, 949-952 (2005).
46. Heimsath, A., Fink, D. & Hancock, G. The 'humped' soil production function: eroding Arnhem Land, Australia. *Earth Surface Processes and Landforms* **34**, 1674-1684 (2009).
47. Owen, J. J. *et al.* The sensitivity of hillslope bedrock erosion to precipitation. *Earth Surface Processes and Landforms* **36**, 117-135 (2011).
48. Dixon, J., Hartshorn, A., Heimsath, A., DiBiase, R. & Whipple, K. Chemical weathering response to tectonic forcing: A soils perspective from the San Gabriel Mountains, California. *Earth. Planet. Sci. Lett.* **323-324**, 40-49 (2012).
49. Burke, B., Heimsath, A. & White, A. Coupling chemical weathering with soil production across soil-mantled landscapes. *Earth Surface Processes and Landforms* **32**, 853 (2007).
50. Burke, B., Heimsath, A., Dixon, J., Chappell, J. & Yoo, K. Weathering the escarpment: chemical and physical rates and processes, south-eastern Australia. *Earth Surface Processes and Landforms* **34**, 768-785 (2009).
51. Norton, K. & von Blanckenburg, F. Silicate weathering of soil-mantled slopes in an active Alpine landscape. *Geochim. Cosmochim. Acta* **74**, 5243-5258 (2010).
52. Dixon, J., Heimsath, A. & Amundson, R. The critical role of climate and saprolite weathering in landscape evolution. *Earth Surface Processes and Landforms* **34**, 1507-1521 (2009).
53. Milliman, J. & Farnsworth, K. *River Discharge to the Coastal Ocean: A Global Synthesis*. (Cambridge University Press, 2011).
54. Jacobson, A. D. & Blum, J. D. Relationship between mechanical erosion and atmospheric CO_2 consumption in the New Zealand Southern Alps. *Geology* **31**, 865-868 (2003).

55. Lyons, B., Carey, A., Hicks, D. & Nezat, C. Chemical weathering in high-sediment-yielding watersheds, New Zealand. *Journal of Geophysical Research* **110**, F11008 (2005).
56. Hicks, D. M. *et al.* Suspended sediment yields from New Zealand rivers. *Journal of Hydrology (New Zealand)* **50**, 81 (2011).
57. Willenbring, J., Codilean, A. & McElroy, B. Earth is (mostly) flat: Apportionment of the flux of continental sediment over millennial time scales. *Geology* **41**, 343-346 (2013).
58. Basher, L., Tonkin, P. & McSaveney, M. Geomorphic history of a rapidly uplifting area on a compressional plate boundary: Cropp River, New Zealand. *Zeitschrift für Geomorphologie* **69**, 117-131 (1988).